Rational Design of Antimony Nanostructures toward High-Performance Anode Materials for Sodium-Ion Batteries

Dissertation

zur Erlangung des Doktorgrades

Dr. rer. nat.

vorgelegt der

Fakultät für Mathematik und Naturwissenschaften der

Technischen Universität Ilmenau

von

M. Sc. Liying Liang

Ilmenau

TECHNISCHE UNIVERSITÄT
ILMENAU

Abstract

Rechargeable Na-ion batteries have received growing attention as the most promising alternative to Li-ion batteries for large-scale energy storage applications, due to the abundant nantural Na resources and its low cost. However, one of the challenges to commercializing Na-ion batteries is to exploit suitable anode materials to host Na ions, because Na ions have a larger radius than that of Li ions. Among various anode material candidates, metallic Sb is quite attractive because of its high theoretical capacity (660 mAh g^{-1}) and a relatively safe operating potential of around 0.4 V (*vs.* Na^+/Na). In spite of these advantages, the main bottleneck for the implementation of Sb anode in practice is its large volume variation (~390%) during cycling, since it is easy to induce pulverization of Sb materials and thus electrical isolation from the current collector, consequently exhibiting rapid capacity degradation and poor rate capability.

In order to address this challenge of large volume change of Sb, new pathways are developed within this dissertation, moreover, they are successfully implemented into a full cell. It is well known that to achieve high electrochemical performance, three important elements are indispensable, which are high ion diffusion, fast electron transport, and stable electrode structure. These three aspects can be realized by the rational design of electrode structure. In this regard, three different performance-oriented electrodes are fabricated, which are hierarchical fern leaf-like Sb, large-scale highly ordered Sb nanorod arrays, and hierarchical Sb-Ni nanoarrays, respectively. Additionally, the three structures all can be used as additive-free anodes for Na-ion batteries, which not only is beneficial to improve rate performance, but also can reduce the cost of the battery system and omit the complicated electrode fabrication processes. In return to these advanced electrode designs, three different Sb anodes all demonstrate the large capacity, long cycle life, and high rate capability. Furthermore, the feasibility of these three electrodes in practice are fully proved in the successful implementation of Na-ion full cells. These design strategies could provide valuable guidance for addressing the large volume changes of other electrode materials for realizing fast and stable Na-ion storage.

Zusammenfassung

Durch die hohe Verfügbarkeit von Natrium und die geringen Kosten haben wiederaufladbare Na-Ionen-Batterien viel Aufmerksamkeit als Alternative für Li-Ionen-Batterien für den Großeinsatz als Energiespeicher erhalten. Eine Herausforderung zur Kommerzialisierung von Na-Ionen-Batterien ist es, nutzbare Anodenmaterialien zu finden um Na-Ionen aufzunehmen, da Na-Ionen einen größeren Radius als Li-Ionen besitzen. Unter verschiedenen Kandidaten als Anodenmaterial ist metallisches Sb (Antimon) sehr attraktiv durch seine hohe theoretische Kapazität (660 mAh g^{-1}) und ein relativ sicheres Betriebspotential von ca. 0.4V (*vs.* Na^+/Na). Trotz dieser Vorteile ist der größte Engpass für die Verwendung von Sb-Anoden in der Praxis ihre hohe Volumenänderung (~390%) während des Lade- bzw. Entladezyklus, was eine Pulverisierung der Sb-Materialien und somit zur elektrischen Isolation vom Stromkollektorinduziert und somit zu einer schnellen Degradation der Kapazität und damit schlechten Zyklenfestigkeit führt.

Um dieses Problem der großen Volumenänderung von Sb anzugehen wurden im Zuge dieser Dissertation neue Wege entwickelt und darüber hinaus erfolgreich in einer Vollzelle implementiert. Es ist bekannt, dass um eine gute elektrische Performance zu erhalten drei wichtige Dinge unerlässlich sind, diese sind eine hohe Ionen-Diffusion, schneller Elektronentransport und stabile, haltbare Elektrodenstrukturen. Diese drei Aspekte können durch ein rationales Design der Elektrodenstruktur realisiert werden. In dieser Hinsicht wurden drei verschiedene effizienz-orientierte Elektroden hergestellt, diese sind eine hierarchische farnblatt-ähnlicheSb-Elektroden, groß-skalige sehr gleichmäßig angeordnete Sb-Nanorod-Arrays sowie hierarchische Sb-Ni-Nanoarrays. Zusätzlich können alle drei Strukturen als additiv-freie Anoden für Na-Ionen-Batterien verwendet werden, was nicht nur vorteilhaft ist um die Zyklenperformance zu verbessern, sondern auch die Kosten des Batterie-Systems reduzieren kann sowie komplizierte Prozesse der Elektrodenherstellung unnötig macht. Im Gegensatz zu diesen fortgeschrittenen Elektrodendesigns zeigen alle drei verschiedenen SB-Anoden eine hohe Kapazität, ein hohe Zyklenzahl sowie hohe Zyklenfestigkeit. Des Weiteren wurde die Umsetzbarkeit der drei Elektroden in der Praxis vollständig bewiesen indem diese erfolgreich in Na-Ionen-Batterien-Vollzellen implementiert wurden. Diese Designstrategien können eine wertvolle Orientierung für die Problematik der Volumenänderung auch anderer Elektrodenmaterialien für die Realisierung von schnellen und stabilen Na-Ionen-Energiespeichern darstellen.

Acknowledgement

I would like to appreciate all people who supported me in different ways during my Ph.D. period and the elaboration of my thesis.

First and foremost, I would like to express my deepest and the most sincere gratitude to my advisor Prof. Dr. Yong Lei. I thank him for providing me with the opportunity to conduct my Ph.D. thesis in his research group at TU Ilmenau. It is truly an honor to be his student. I appreciate all his contributions of time, immense knowledge, encouragement, support, and guidance to make my Ph.D. experience enjoyable and productive. He has taught me the attitude, logic, and methodology to conduct real science. He encouraged me to not only grow as an experimentalist but also as an independent thinker and an instructor. I am also grateful for the excellent example he has shown me as a dedicated, successful, and well-respected scientist. Besides the academic matters, he has also encouraged me into academic activities including teaching activities and conference management. I greatly appreciate the enjoyable and valuable experiences and memories that we shared in the past four years.

Second, I would like to thank the current and past members of Prof. Dr. Yong Lei's group. They have immensely contributed to my professional and personal development, and without their efforts, my work would have undoubtedly been more difficult. My particular thanks to Dr. Yang Xu for his fruitful discussions and countless help. He is always patient and supportive, showing me the wonderful side of science research, helping me in all the time of research, and teaching me how to organize a logic research paper. My sincere thanks also go to Dr. Min Zhou, Dr. Huaping Zhao, Dr. Chengliang Wang, Dr. Liaoyong Wen, and Mrs. Moumou Li for their meaningful advice and consistent help both in working and living. Many thanks to Dr. Dawei Cao, Dr. Zhijie Wang, Dr. Yaoguo Fang, Mr. Rui Xu, Mr. Nasori, Dr. Yan Mi, Dr. Fabian Grote, Dr. Samar Tarish, Dr. Ahmed Shukur Hameed Al-Haddad, Mrs. Benrong Hai, Mr. Lin Cheng, Dr. Ranjith Vellacheri, Mr. Max Sommerfeld, Mr. Stefan Bösemann, Mrs. Yan Zheng, Mr. Wenxin Wang, Mr. Long Liu, Mrs. Yi Wang, and Mr. Huanming Zhang for their many kinds of technique support whenever needed as well as useful feedback and insightful comments on my work. I certainly enjoy such an inspiring and cooperative working atmosphere. The warm support and love from all my friends help me grow up and have a very good time along the way. I will never forget those delightful moments in the group.

Regarding measurements, I want to thank Dr. Henry Romanus for his effort and precious time during the measurements of SEM and TEM. I also thank Dr. Yueliang Li and Dr. Haoyuan Qi from Prof. Dr. Ute Kaiser's group at the University of Ulm for the help of TEM measurements as well as valuable discussions and suggestions.

Moreover, I am also indebted Prof. Dr. Changming Li from the Southwest University for inviting me to visit his group for two months. The welcoming atmosphere has inspired me and the collaborating work has resulted in excellent scientific results. The stay gives me great and unforgettable memories both from a scientific and non-scientific point of view.

Finally, my deep appreciation goes to Dr. Li Zhao for his support, encouragement, quiet patience and unwavering love that were undeniably the bedrock. He is accompanying me through all those good and challenging time, and helping me grow into a mature, independent, and optimistic person. I am forever grateful to my dear family: my parents and my brother, for their constant support, love and allowing me to be as ambitious as I wanted.

Table of Content

List of Figures

List of Tables

List of Abbreviations

1D	One-dimensional
2D	Two-dimensional
3D	Three-dimensional
AAO	Anodic aluminum oxide
ALD	Atomic layer deposition
Al_2O_3	Aluminum oxide
C	Carbon
CE	Coulombic efficiency
CNT	Carbon nanotube
CPE	Constant phase element
CV	Cyclic voltammetry
CVD	Chemical vapor deposition
DEC	Diethyl carbonate
EC	Ethylene carbonate
ED	Electrochemical deposition
EDX	Energy-dispersive X-rays
EIS	Electrochemical impedance spectroscopy
ESS	Energy storage system
FEC	Fluoroethylene carbonate
FE-SEM	Field emission scanning electron microscopy
FFT	Fast Fourier transform
HONA	Highly ordered nanostructured array
HRTEM	High resolution transmission electron microscopy
i_p	Peak current
LIBs	Lithium-ion batteries
$LiCoO_2$	Lithium cobalt oxide
$LiClO_4$	Lithium perchlorate
$LiFePO_4$	Lithium iron phosphate
MWCNT	Multiwall carbon nanotubes
$Na_2C_8H_4O_4$	Disodium terephthalate
$NaClO_4$	Sodium perchlorate

NaCoO$_2$	Sodium cobalt oxide
NASICON	Na$^+$ superionic conductor
PC	Propylene carbonate
PHMSs	Porous hollow microspheres
PVD	Physical vapor deposition
Q	Total capacity
Q_s	Surface capacity
Q_d	Diffusion-controlled capacity
R$_{ct}$	Charge transfer resistance
RGO	Reduced graphite oxide
R$_s$	Electrolyte resistance
SAED	Selected area electron diffraction
SEI	Solid electrolyte interphase
SEM	Scanning electron microscopy
SHE	Standard hydrogen electrode
SIBs	Sodium-ion batteries
TEM	Transmission electron microscopy
TiO$_2$	Titanium dioxide
XRD	X-ray diffraction spectroscopy
v	Potential scan rate
W$_o$	Warburg element

1 Introduction

The depletion of non-renewable resources has pushed the existing fossil fuel dependent energy economy to be at a serious risk. Adopting renewable energy together with efficient energy storage systems would be a promising solution. Lithium-ion batteries (LIBs) have been widely employed as power sources for portable electronic devices. However, there are still great concerns about the safety, and lithium's cost and continued availability.[1-4] Therefore, as a potential alternative to LIBs, sodium-ion batteries (SIBs) have recently attracted extensive attentions, since sodium is much cheaper, safer, and more environmentally benign than lithium.[5] Due to the larger radius of Na^+ than that of Li^+, it is difficult to find a suitable electrode material to afford reversible and rapid Na ions insertion and extraction.[6, 7] In this regard, improvements have been achieved for SIBs cathode materials,[8-17] however, less have been devoted on the side of anode materials. Several carbonaceous materials have been presented, however, due to poor intercalation property for large Na ions, limited capacities at a high rate are shown.[18-25] Another emerging anode of titanate also has been widely investigated.[26-30] Although they generally show stable Na-ion storage reversibility, their capacities especially at high rates are not satisfactory.

As the most promising SIB anode candidate, antimony (Sb) has been widely investigated due to its large Na storage capacity of 660 mAh g^{-1}, excellent electronic conductivity, and moderate operating voltage.[31] However, the practical application of Sb is mainly hindered by two problems which are the massive volume expansions (about 390%) during repeated sodiation/desodiation processes and the utilization of electrode additives in the process of Sb electrode fabrication.

Regarding the large volume variation, it is easy to induce severe pulverization and subsequent loss of electrical contact within electrodes as well as continual solid electrolyte interphase (SEI) growth on the Sb surface, consequently greatly decreasing the cycling life and rate capability of electrodes.[32, 33] Indeed, pure Sb powder delivered a high initial capacity of 624 mAh g^{-1}, while after 25 cycles the capacity quickly droped to less than 100 mAh g^{-1}.[34]

To address the large volume expansion of Sb, three methods were mainly reported. One is to develop nanosized materials, since reducing the dimension of Sb into nanometer range could improve the tolerance of stress change during alloying/dealloying processes, and shorten electronic and ionic transport, hence gaining long and stable cycling performance

and good rate capability.[35-39] Another effective approach is to prepare Sb materials integrated with conductive matrices such as carbon,[38-40] rGO,[41, 42], MWCNT,[43] and TiO_2[44] that act as a buffer to relieve the mechanical stress generated during the sodiation/desodiation reactions, and prevent particle aggregation as well as offer electronic conduction. Constructing Sb into Sb alloys (such as NiSb,[45, 46] SnSb,[36, 47, 48] and Cu_2Sb[49, 50]) has also been reported to reduce the drastic volume variations and thus to enhance the cycle life of this material. In these Sb alloy anodes, the volume changes and aggregation of active Sb elements are reduced and prevented by the electrochemically inactive component which acts as a buffering matrix to maintain the complete electrode structure during charge/discharge process.

The second challenge of the utilization of electrode additives extremely restricts the further application of Sb in practice. The majority of reported Sb anodes generally include the addition of conductive carbons and organic binders.[38, 48, 51-56] Actually, the binders don't contribute to Na-ion storage, and would lead to insufficient ion permeation and block electron transport, due to reduced available contact area of the active materials and increased polarization of the electrodes.[57] The electrical conductor only provides the minimal improvement of battery performance. The two components also increase the weight of the battery system and make the fabrication process complicated.[57, 58] Therefore, it is greatly essential to develop additive-free electrodes for achieving high-performance SIBs.

In this dissertation, focusing on the aforementioned two major challenges of Sb anode, we propose three novel solutions for realizing remarkably improved electrochemical performance. The key achievements in this dissertation include the following aspects:

A hierarchical Sb structure directly grown on Ti substrate is successfully fabricated, which is composed of well-crystallized Sb nanoparticles to present the morphology of fern leaf. Owing to the merits of directly growing hierarchical structures on the current collector, the fern leaf-like Sb reveals desirable properties for Na-ion storage, such as good electrical conductivity and large surface area. It was applied as the additive-free Sb anode for SIB, showing excellent cyclability and rate capability, which can be attributed to its morphological and structural features that can ensure the fast ion and electron transport, and stable electrode structure.

A performance-oriented electrode structure: highly ordered Sb nanorod array is proposed, which is 1D nanostructure arrays with large-scale high ordering, well vertical alignment, and large interval spacing. The excellent electrochemical performance is achieved in return

for its pathbreaking electrode design which ensures high Na ion accessibility, fast electron transport, and strong structural integrity. The structural factors were also investigated in detail to realize the most optimization of Na-ion storage property.

A novel 3D hierarchical electrode composed of Sb nanoplates on Ni nanorod arrays is proposed to tackle the issues of the rapidly fading capacity and poor rate capability of Sb materials for Na-ion batteries. The 3D Sb-Ni nanoarray anode demonstrates the synergistic effect of the 2D nanoplates, open conductive array structure, and strong structural integrity, rendering excellent Na-ion storage performance by tailoring electrode nanostructures. To explain the high-rate performance, kinetics and quantitative analysis of Na^+ storage mechanism are conducted according to Trasatti's method. The capacitive behavior for the Na-storage reactions in 3D Sb-Ni nanoarrays is verified, clearly indicating that the Na reaction kinetics and durability in 3D Sb-Ni nanoarrays can be elaborately tailored by architecture design. We also systematically investigated the critical factors for achieving high capacity with long-term cyclability under fast-charge and -discharge.

To further present the feasibility of the aforementioned three electrode configurations for Na-ion storage in practice, the full cells were investigated by consisting of P2-$Na_{2/3}Ni_{1/3}Mn_{2/3}O_2$ as positive electrodes and the above three architectures as negative electrodes, respectively. The three different full cells all show the long cycle life, excellent rate capability, and high energy densities.

The excellent electrochemical properties make these anodes promising as a power supply for Na-ion batteries and provide useful guidelines for designing nanostructured Sb electrodes for viable sodium-ion battery applications. These design strategies may also work in other electrode materials for fast and stable sodium storage. Meanwhile, the obtained encouraging results may accelerate further development of SIBs by smart nano-engineering of the electrode materials.

2 Sodium-ion batteries for energy storage

Energy storage and conversion have become significant topics concerning our welfare in daily life. With the fast depletion of fossil fuel resources and growing environmental problems, various clean and renewable energy sources, such as the wind, solar radiation and waves, are rapidly increasing. However, the growing use of renewable energy sources also brings out other problems, including controlling variable renewable resources in time and combining them into the grid safely and smoothly. It is also vital to optimize grid utilization by balancing electricity production and need between daytime and nighttime.[59] Therefore, a large-scale energy storage system (ESS) is greatly necessary to transfer electrical energy from on-peak to off-peak periods to achieve smart grid administration.[4] Among a variety of available energy storage technologies, the electrochemical secondary battery technology is one of the most promising candidates of storing electricity on a large-scale, due to its high energy conversion efficiency, flexibility, no gaseous exhaust, and easy equipment maintenance.[60] Such features make batteries to turn into a viable energy storage technique for the integration of renewable energy sources that offer intermittent energy into the grid.

So far, lithium-ion batteries (LIBs), which have conquered the portable electronic market, have been considered as the most potential candidate to power the next generation of electric vehicles and plug-in electric vehicles.[4, 60-63] Moreover, Li-ion batteries offer the highest energy density and the output voltage of all rechargeable battery technologies in use.[60] The Li-ion battery application raises concerns for a possible storage of the limited lithium (Li) resources in the Earth's crust, the growing price of Li resources and the safety of LIB.[64] Therefore, it is urgent and desired to exploit cheap, highly safe, and long-cycle rechargeable batteries based on abundant resources. Compared with Li, sodium (Na) has similar chemical and physical properties. Thus, recently, rapidly increasing attention has moved to sodium-ion batteries (SIBs) because of the abundant natural Na resources and their low cost.[4, 32, 65, 66] Theoretically speaking, Na-ion batteries would not exceed the energy density of that of LIBs because Na is three times heavier and larger than Li as well as less-reducing potential of Na. But considering its suitable potential of -2.71 V (*vs.* SHE), which is only 0.3 V more positive than that of Li, there is only a small energy sacrifice to pay, meaning that SIBs could be more suitable in the field of large-scale ESS, in which the working cost and long life of the batteries are more vital aspects of a whole system.[67, 68]

Thus, developing Na-ion batteries with a similar working principle as Li-ion batteries for large-scale ESS still is a reasonable alternative.

2.1 Why are sodium ions attractive as charge carriers for energy storage?

The material's abundance is the simplest and the most distinct reason as to why sodium ions are important as charge carriers for rechargeable batteries. Except that, the following merits are also relatively attractive.[7] First, although electrochemical equivalent of Na^+/Na is three times heavier than that of Li^+/Li,[69] the difference in the theoretically reversible capacity of the Na^+-based electrode material and the Li^+-based electrode material becomes smaller. For example, $LiCoO_2$ and $NaCoO_2$ as layered oxides, they possess the same crystal structure. The calculated theoretical capacity is 274 and 235 mAh g^{-1} for $LiCoO_2$ and $NaCoO_2$, respectively.[70] In result, the reversible capacity is decreased by only 14%. This problem can be potentially solved if the material's innovation is conducted in the future. Similarly, the volumetric capacity of Li is much larger than that of Na because the difference in the molar volume of Li and Na metals is large (21.3 $Å^3$ per Li atom and 39.3 $Å^3$ per Na atom; $\Delta V = 18 Å^3$).[69] The gap in the volumetric capacity becomes much smaller when compared for $LiCoO_2$ and $NaCoO_2$ because of the low difference in the molar volume for $LiCoO_2$ and $NaCoO_2$ (32.3 $Å^3$ per $LiCoO_2$ and 37.3 $Å^3$ per $NaCoO_2$; $\Delta V = 5$ $Å^3$). If realizing the battery technology based on the Na ions not metal is the final goal, the energy penalty can be potentially shrunk. Therefore, SIBs are expected to be the competitive battery system for LIBs.[7]

Second, the high ion conductivity of the Na^+-based electrolyte is also helpful to enhance the battery performance compared to the Li^+-based electrolyte.[71] A study of comparing the molar conductivity of $NaClO_4$ and $LiClO_4$ has shown a relatively low viscosity of $NaClO_4$ solutions with aprotic solvents, and the conductivity is also higher (10−20%) than that of $LiClO_4$ solutions. These facts also probably come from the size difference between Na and Li which is related to the solvation energy and solvated states of ions in aprotic polar solvents.

Third, since Na ions are relatively large ions, they provide the possibility to enhance the flexibility of materials design. Therefore, a large range of crystal structures is recorded for polyanionic compounds layered oxides. The structural chemistry of the Na system is much more complicated than that of the Li system. Thus, many materials with different crystal structures are easily fabricated under thermodynamic equilibrium conditions. Indeed, to

date, many Na-containing compounds have been synthesized and used as precursors to obtain new lithium insertion materials by Na^+/Li^+ ion exchange.[7]

Lastly, it is reported that larger ionic radii are weak solvation energy in the polar solvent.[69] Because the desolvation energy plays an important role in the kinetics of alkali-ion insertion processes at the electrolyte interface,[72, 73] the relatively low energy for desolvation is critical to design high-power batteries. As the same monovalent ions, large Na ions have a relatively smaller charge density around ions than Li ions. Therefore, Na ions are not energetically stabilized by accepting/sharing more electrons from/with the solvated polar molecules, namely, Na^+ is considered as a relatively weak Lewis acid. As a result, a relatively small energy for the desolvation process is needed for Na^+ compared with Li^+.[69] Similarly, compared with $LiCoO_2$, results of first-principles calculation indicate that the activation energy of Na^+ diffusion is relatively small for $NaCoO_2$.[5]

2.2 The working principle of sodium-ion batteries

The functionality of SIBs is the same as LIBs wherein the electrodes made of intercalating compounds store electrical energy. The battery is made of a positive electrode (cathode) and a negative electrode (anode) with a porous separator and a conductive electrolyte between them. The potential difference between the two electrodes creates a voltage on the cell.[74] The Na ions move back and forth between the positive and negative electrode through an organic electrolyte during the charge and discharge cycles. The process is similar to a rocking chair, so the system is named as "rocking-chair battery".

A typical working process is illustrated in Figure 2-1. During charge, Na ions are extracted from positive electrode (above 3.0 V *vs.* Na^+/Na) and inserted into negative electrode (below 1.0 V *vs.* Na^+/Na). Meanwhile, electrons are thermodynamically drawn out from positive electrode to negative electrode through the external circuit. During discharge, the reverse mechanism occurs, and the ions and electrons reactions oppositely proceed and thus converting chemical energy into electrical energy.[67] The main role of the separator is to make the positive electrode and negative electrode separated and then to prevent their contact with the short circuit, in addition to the electrolyte ions can pass through. The electrolyte is serving as the medium for ion transport.
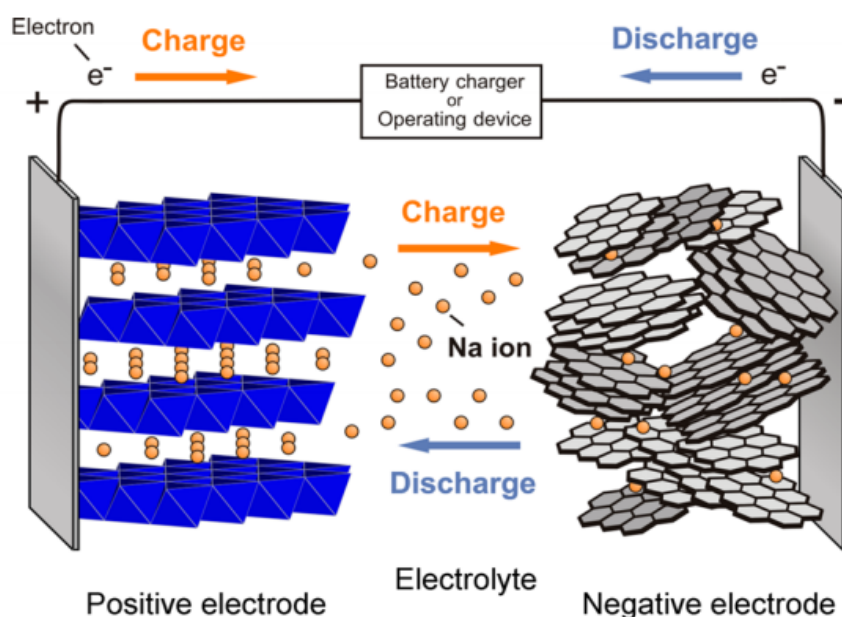
Figure 2-1 The working principle of sodium-ion batteries.[7]

2.3 Positive electrode materials

For positive electrode materials, Na ion intercalation chemistry is very similar to Li, thereby making it possible to apply very similar compounds for both kinds of systems. A great range of compounds is being studied as possible SIBs cathodes, including oxides,[9, 11, 75-80] phosphates,[81-85] fluorophosphates.[14, 86-88] Each family of compounds reveals its own advantages and disadvantages for their practical application in energy storage systems.

2.3.1 Layered oxides - P2-$Na_{2/3}[Ni_{1/3}Mn_{2/3}]O_2$

The layered Na_xMeO_2 (M = Ni, Mn, Cr, Co, *etc.*) oxide is considered to be a promising cathode system for SIBs due to their high capacity, material cost, and safety.[89] The most common layered structures are constructed from a sheet of edge-sharing MeO_6 octahedral. Polymorphisms appear when the sheets of edge-sharing MeO_6 octahedral are stacked with different orientations along the c-axis direction. Na-based layered materials can be classified into two main groups according to the classification proposed by Delmas *et al.*[79]: O3 type or P2 type, in which the Na ions are held at octahedral and prismatic sites, respectively, as shown in Figure 2-2.
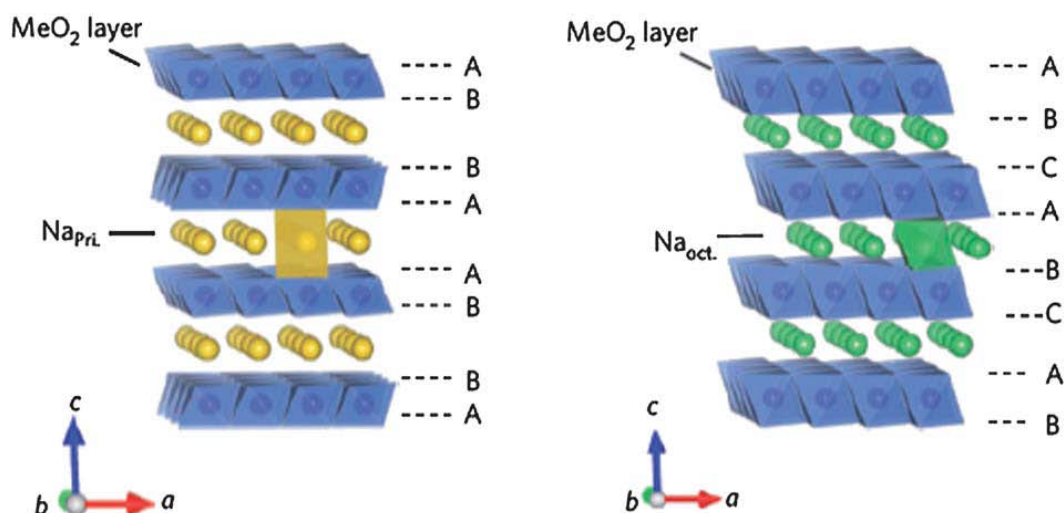
Figure 2-2 Layered structure of P2-type (left) and O3-type (right) Na_xMeO_2.[9]

There is a wide variety of transition metals and their combinations that can generate layered Na_xMeO_2 compounds, as shown in Figure 2-3. Each of them owns a different operating potential and specific capacity, which defines its energy density.
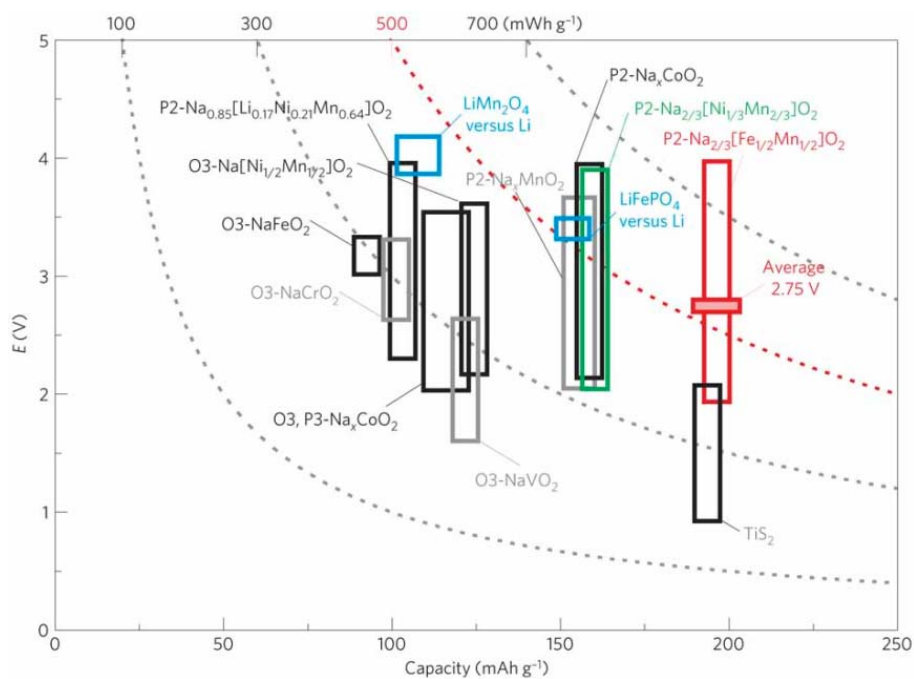
Figure 2-3 The comparison of operating voltage ranges and reversible capacities of the layered Na insertion cathodes. The energy density was calculated on the basis of the voltage *vs.* Na metal for simplicity. $LiMn_2O_4$ and $LiFePO_4$ are also displayed for comparison based on the voltage *vs.* Li metal.[9]

For instance, Na insertion and extraction into and from P2-$Na_{2/3}[Ni_{1/3}Mn_{2/3}]O_2$ phase have been studied. All sodium ions reversibly extract based on the Ni^{2+}/Ni^{4+} redox, which shows high operating voltage as a Na insertion host. The theoretical specific capacity is 173 mAh g^{-1}.[4] As shown in Figure 2-4, several voltage plateaux were observed from 2 to 4.5 V *vs.* Na/Na^+. A long potential plateau at 4.2 V *vs.* Na/Na^+ presents in the range of $1/3 \leq x \leq 2/3$ in $Na_{2/3-x}[Ni_{1/3}Mn_{2/3}]O_2$.[17] It has been proved that there is the two-phase coexistence of P2-$Na_{2/3}[Ni_{1/3}Mn_{2/3}]O_2$ and O2-$Na_{2/3}[Ni_{1/3}Mn_{2/3}]O_2$.[90] Due to the appearance of O2-phase transition, a large volume change (more than 20%) unavoidably presents in this region, then resulting in the poor cyclability. The cyclability can be significantly improved in the electrochemical cycle in the region of $0 \leq x \leq 1/3$ Na $_{2/3-x}[Ni_{1/3}Mn_{2/3}]O_2$ without the O2-pahse transition.[91] P2-$Na_{2/3}[Ni_{1/3}Mn_{2/3}]O_2$ is relatively stable in moist air, and water molecules cannot be inserted into the structure.[92]
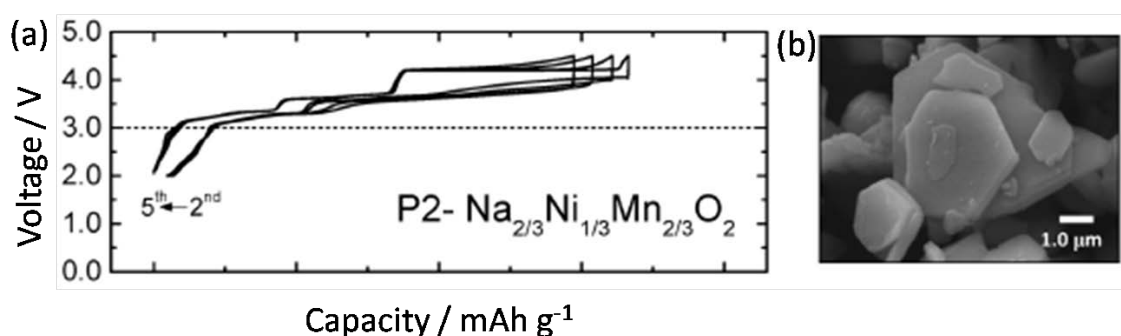
Figure 2-4 (a) Galvanostatic charge/discharge curves and (b) SEM image of P2-$Na_{2/3}[Ni_{1/3}Mn_{2/3}]O_2$.[17]

2.3.2 Phosphates - NASCION $Na_3V_2(PO_4)_3$

Framework materials based on the phosphate polyanion have recently been studied as promising electro-active materials for Na-ion batteries applications. The metal phosphates including olivine and NASICON structures seem to preserve particular potentials. The high inductive effect of the PO_4^{3-} polyanion mitigates the energetics of the transition metal redox couple to produce relatively high operating voltages, structural and thermal stability of these compounds.[93] Table 2-1 reveals some compounds that could be useful as positive SIBs electrodes with their theoretical specific capacities.

Table 2-1 Main phosphate phases that can be used as positive SIBs electrode materials and their theoretical specific capacity.[4]

Compound	e⁻ transfer	Theoretical capacity/mAh g⁻¹
$NaFePO_4$ (olivine)	1	154
$NaVPO_4F$	1	143
$Na_3V_2(PO_4)_2F_3$	2	128
$Na_{1.5}VOPO_4F_{0.5}$	1	130
Na_2FePO_4F	1	124
$Na_3V_2(PO_4)_3$	2	118
$NaFe_2Mn(PO_4)_3$	2	108

NASICON (Na⁺ Superionic Conductor) - related compounds behave a three-dimensional (3D) framework that shows large interstitial spaces through which Na ions can diffuse.[94, 95] A typical NASICON material of $Na_3V_2(PO_4)_3$ was firstly investigated as a cathode material *vs.* Na metal by Goodenough.[96] The structure of $Na_3V_2(PO_4)_3$ can be regarded as each VO_6 octahedron corner sharing with three PO_4 tetrahedrons, and one Na⁺ ion occupying in the two in the M2 (18e) site and one M1 (6b) site of the interstitial sites, where M2 sites are situated between adjacent $[V_2(PO_4)_3]_\infty$ ribbons while M1 sites are located between two adjacent $[V_2(PO_4)_3]_\infty$ units in the same $[V_2(PO_4)_3]$ ribbon (Figure 2-5a).[97] $Na_3V_2(PO_4)_3$ presents two potential plateaux located at 3.4 and 1.6 V *vs.* Na/Na⁺, corresponding to the V^{3+}/V^{4+} and V^{2+}/V^{3+} redox couples, respectively. These two reaction voltages are related to a specific capacity of 117 and 50 mAh g⁻¹ for the high and low voltage regions, respectively. Recently, Lim *et al.* has correlated these two plateaux with the energies calculated for different Na distributions in the phase (Figure 2-5b).[98] As $Na_3V_2(PO_4)_3$ compound has two crystallographical sites for Na, Na1 site keeps totally occupied with one Na ion while Na2 site is active when the Na content goes from $Na_3V_2(PO_4)_3$ to $NaV_2(PO_4)_3$.[89] Moreover, in this range, the formation of the two extreme phases is energetically advantageous, so a two-phase reaction is expected. This structural evolution has been confirmed by in situ XRD measurement. The volume change between them is only 8.26%.[99] Due to good electrochemical and thermal stability, $Na_3V_2(PO_4)_3$ shows promising applications in SIBs.
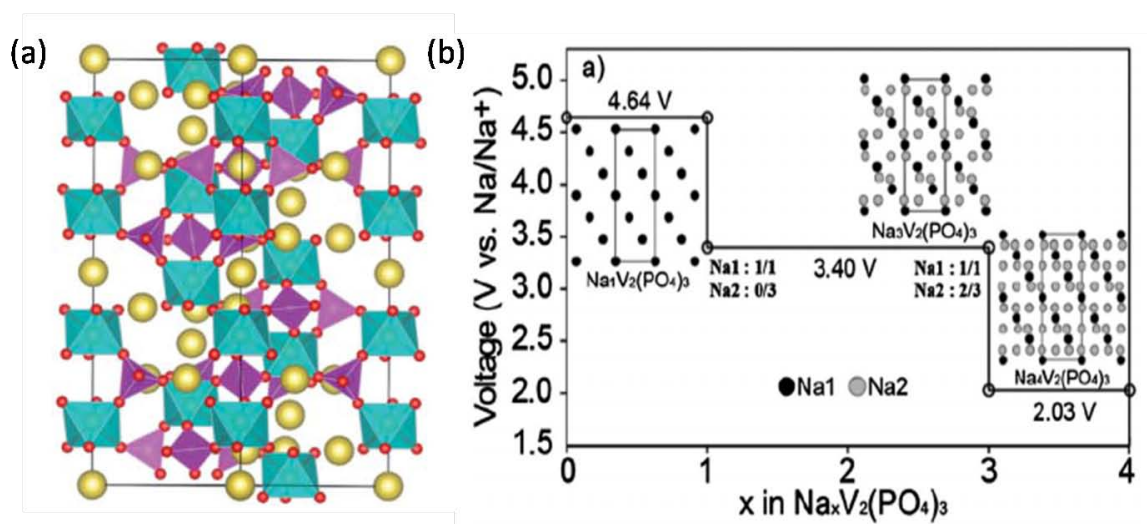
Figure 2-5 (a) The crystalline structure of $Na_3V_2(PO_4)_3$.[59] (b) Voltage profiles estimated from first principle calculations.[98]

2.4 Negative electrode materials

Although a wide range of phases that can potentially be used as positive electrodes have been studied, very few materials have been identified to be useful as negative electrodes. Metal Na is not advisable due to dendrite formation, similar like metal Li. Except that, the safety of Na anodes has been further put into question by its low melting point of 97.7 ℃ compared to 180.5 ℃ for Li, and its high reactivity and the unstable passivation layer in most organic electrolytes also restrict the application of metal Na.[33] Thus, finding an anode with a proper Na storage voltage, large reversible capacity and high structural stability is highly desired for the further development of Na-ion batteries.

2.4.1 Carbon-based materials

Although graphite is widely used as a negative electrode material in Li-ion batteries, graphite is electrochemically less active in Na cells, because Na hardly forms staged intercalation compounds with graphite.[100] However, disordered carbons are recently studied, in which the insertion of Na occurs at a higher voltage than graphite, thus showing the great potential for SIBs.[4]

So far, many carbon materials with various morphologies, such as hollow carbon nanospheres,[22] tailor-made carbon with hierarchical porosity,[24] nanowires,[19] and N-doped porous carbon nanosheets,[101] have been reported for SIBs and demonstrate greatly enhanced Na storage performance and kinetics. However, their initial and following Coulombic efficiencies together with cyclability, cannot meet the requirement of practical

SIB application, due to the side reaction related to the larger surface area resulting from the nanostructures.

2.4.2 Ti-based compounds

Since the potentials for Na insertion in titanates are larger than those of carbon, sodium plating can be avoided in titanates, which makes them also be promising candidates for SIBs negative materials. The most common form of titanium compounds is TiO_2, which is particularly stable, nontoxic, cheap, and abundant materials and has attracted intensive attentions. TiO_2 consists of TiO_6 octahedra with tetravalent titanium ions. Recently, nanosized anatase ($<$30 nm) has been proposed to be electrochemically active in Na-ion batteries.[27, 102] A large reversible specific capacity of about 150 mAh g^{-1} is obtained (corresponding to approximately 0.5 mol of sodium insertion) in the voltage range of 0-2.0 V $vs.$ Na/Na$^+$. Due to a large surface area of nanosized anatase, it inevitably results in low Coulombic efficiency (42%) in the initial cycle. $Na_2Ti_3O_7$ has also been deeply studied as the host material for Na insertion.[29] Its crystal structure consists of a two-dimensional sheet of the composition $(Ti_3O_7)^{2-}$ with edge-shared triple octahedral chains and Na ions are held between the sheets of $(Ti_3O_7)^{2-}$. $Na_2Ti_3O_7$ has the ability to reversibly accommodate two Na ions per formula unit (0.67 Na per Ti with 200 mAh g^{-1}, corresponding to the reduction of 2/3 of the Ti^{4+} to Ti^{3+}) at an average potential of 0.3 V $vs.$ Na/Na$^+$, which is the lowest voltage that ever is reported as topotactic insertion into oxide electrodes in Li/Na-ion batteries. Other forms of titanates can be found in Figure 2-6.
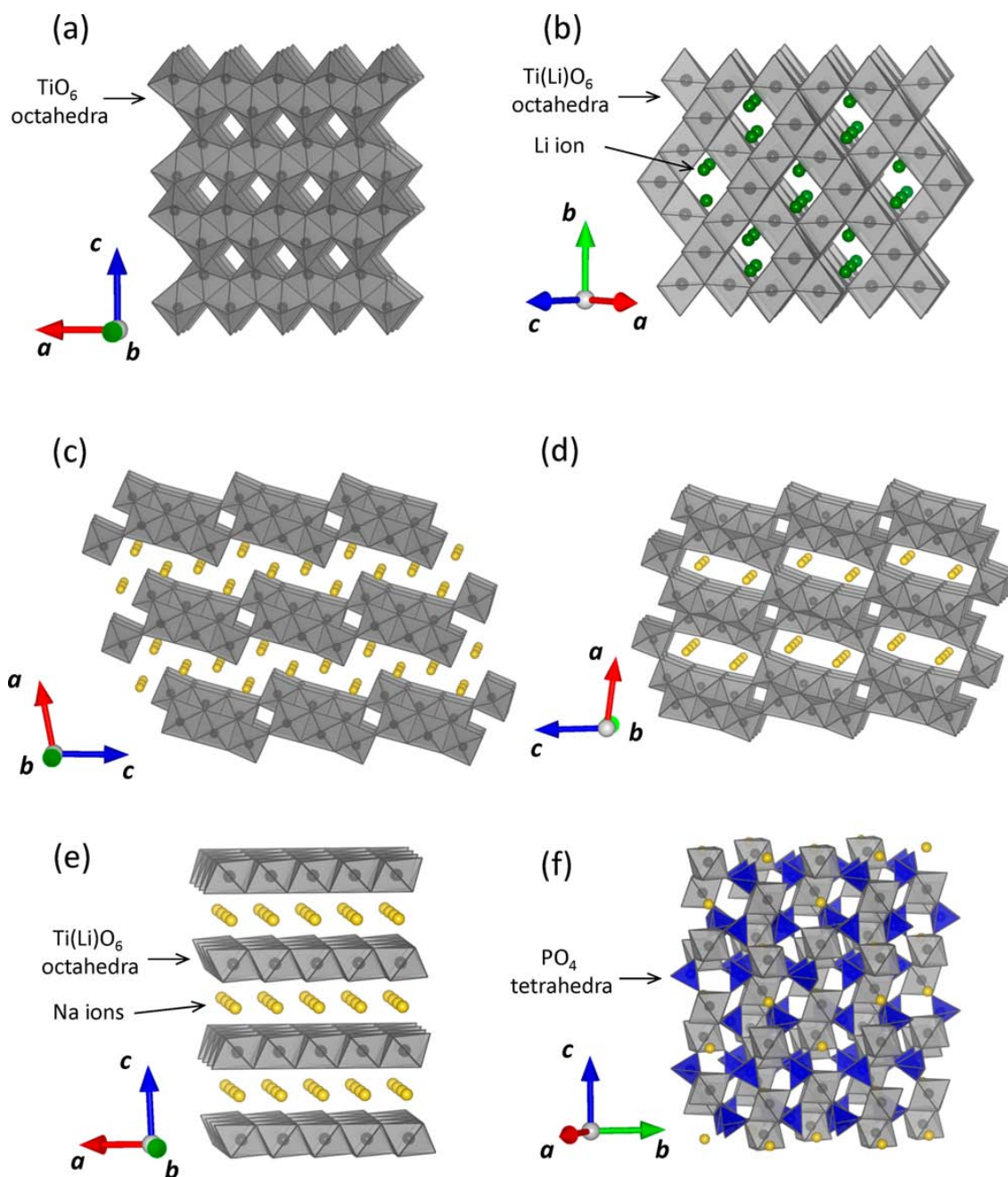
Figure 2-6 Schematic illustrations of (a) anatase-type TiO_2, (b) $Li[Li_{1/3}Ti_{5/3}]O_4$, (c) $Na_2Ti_3O_7$, (d) $Na_2Ti_6O_{13}$, (e) $P2\text{-}Na_{0.66}[Li_{0.22}Ti_{0.78}]O_2$, and (f) $NaTi_2(PO_4)_3$.[7]

2.4.3 Intermetallic Compounds

Group 14 and 15 elements (Figure 2-7a), such as metals (Sn, Pb, Bi), metalloids (Si, Ge, As, Sb), and polyatomic nonmetal (P), are identified to form binary compounds with Na. Their binary compounds can be seen in Figure 2-7. These electrode materials (metals and metalloids), which store Na by forming Na-Me binary intermetallic compounds, have been recently investigated as potential anodes for Na-ion batteries[47, 103-106], due to the high

theoretical capacity and low Na storage potential. They have the property to interact with a larger number of Na (compared to insertion materials), resulting in a much higher capacity than hard carbon and titanium oxides. Metal/metalloid anodes are able to take multiple Na ions per single atom by alloying reactions. Their calculated theoretical capacities of Na combining with Sn, Pb, Ge, Sb and P are 847 ($Na_{15}Sn_4$), 486 ($Na_{15}Pb_4$), 1108 (Na_3Ge), 660 (Na_3Sb) and 2560 mAh g^{-1} (Na_3P), respectively.[36] However, the uptake of multiple Na ions naturally causes large volume changes (*e.g.*, Sn-420%, Pb->400%, Ge- 305%, Sb-390%, P-408%) occurred in the charge/discharge processes, which severely hinders their applications for SIBs.[7, 105, 107-109] Such huge volume expansion could restrict the long-term successive cycling as an electrode material. The large volume expansion, depending on the amount of Na ions incorporated into the structures, is unavoidable in this system, while in many cases the volume expansion for Na insertion materials does not exceed 120%. Therefore, during continuous charge/discharge cycles, the electrode material suffers from high mechanical stress and repeated passivation. The cracking in the composite electrodes leads to a loss of electrical contact, thereby showing a capacity loss. Therefore, studies on metal/metalloid anode materials have mostly focused on improving the cycle stability.

Several strategies have been developed to overcome these problems in relation to the large volume change, including binders, electrolyte additives, preparation of nano-architectured samples, *etc*. The further discussions can be seen in Chapter 3.
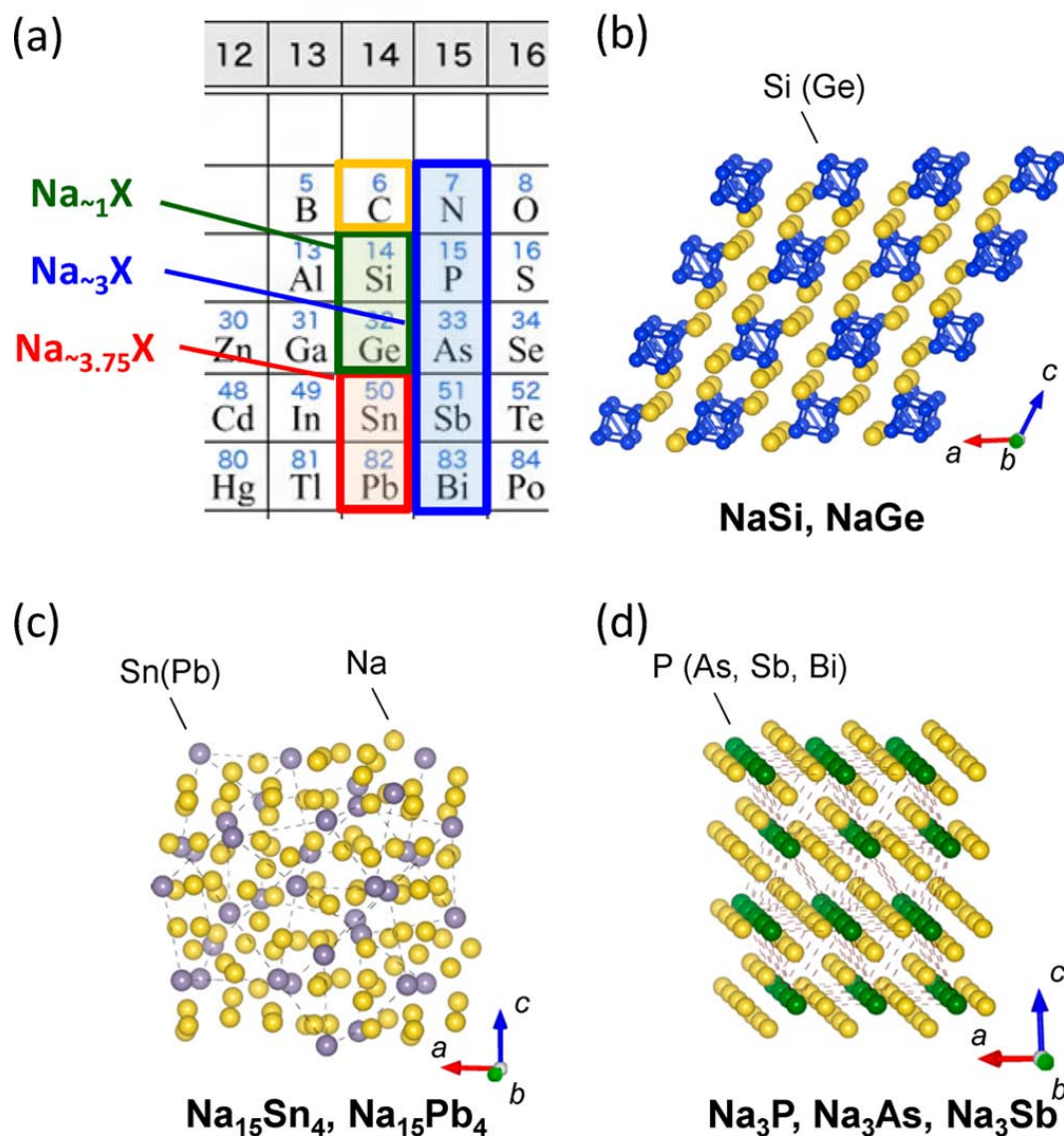
Figure 2-7 (a) Elements of groups 14 and 15 in the Periodic Table to form binary compounds with Na, and schematic illustrations of the most Na-rich phases for Si and Ge (a), Sn and Pb (b), and P, As, and Sb (d).[33]

2.4.2 Organic compounds

Organic molecules with conjugated carboxyl groups have been studied as potential anode materials for the Na system. The electrode performance of disodium terephthalate ($Na_2C_8H_4O_4$) in Na cells as organic materials has been reported.[10, 110, 111] Disodium terephthalate can reversibly insert two sodium ions in terephthalate, as shown in Figure 2-8a. The electrode performance is potentially adjusted by the molecular design with different functional groups and regioisomerism in the structures. $Na_2C_8H_4O_4$ anode delivered a reversible capacity of 250 mAh g^{-1}, corresponding to a two-electron

incorporation at an average voltage of 0.45 V (Figure 2-8b).[110] However, the electronic conductivity of $Na_2C_8H_4O_4$ is rather poor. When preparing the electrode, a large amount of carbon black is needed, thus leading to a low first Coulombic efficiency of about 60%, which is mainly contributed to the side reaction between carbon black and the electrolyte. Therefore, if the electronic conductivity issue can be solved, organic electrode materials with low cost, high storage capacity and facile synthesis can be largely applied as the next-generation electrode material.
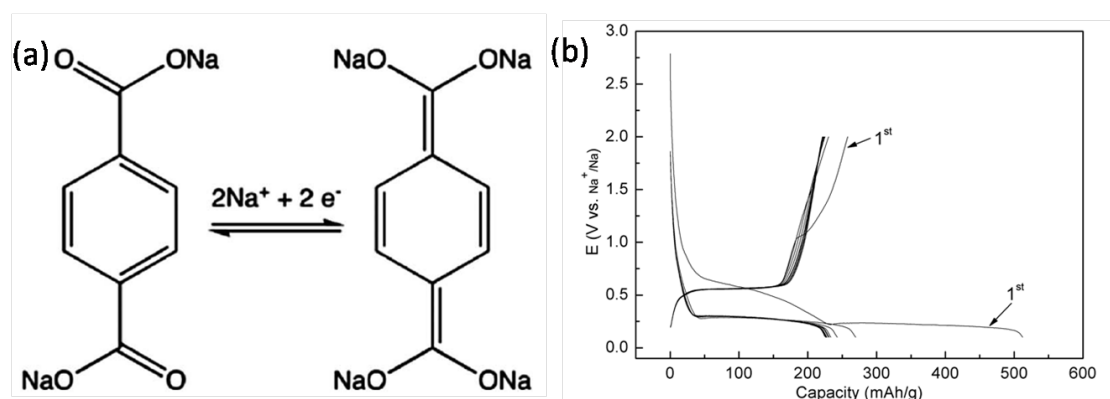
Figure 2-8 (a) The scheme mechanism for Na storage in $Na_2C_8H_4O_4$. (b) The charge/discharge curves of the $Na_2C_8H_4O_4$ electrode.[111, 112]

2.5 Full sodium-ion batteries

In virtue of the abundant Na resources, Na-ion batteries have been considered to be one of the promising alternatives to Li-ion batteries. However, current research concentrates mostly on Na-ion half cells. To exhibit the practicability and commercial value of the materials, full cells have high research value and broad applications in energy storage devices.[32]

Despite the advantages of abundance and low price, the safety issue becomes more important in SIBs, because of the higher activity of Na metal when exposed to oxygen or moisture.[4] Taking these factors into consideration, the construction of Na-ion full-cell systems based on an appropriate set of anode and cathode is extremely significant to guarantee its safety.[113] Current Na-ion full cells are mainly prepared using hard carbon as the anode material, which is capable of offering high voltage when suited with the cathode. However, it suffers from inferior rate capability, and the voltage plateau related to most capacities is too close to the sodium plating voltage, leading to a safety concern.[114]

Recently, a full Na-ion battery with $Na_{0.80}Li_{0.12}Ni_{0.22}Mn_{0.66}O_2$ as the cathode and free-standing Sn@CNT-CP as the anode was constructed, as shown in Figure 2-9, which delivered a reversible capacity of 0.241 mAh at a current of 0.052 mA.[115] Yu *et al.* designed a Na-ion full cell based on nanostructured $Na_2Ti_3O_7$ and $VOPO_4$ materials as the anode and cathode, which showed very promising properties with excellent cycling stability (92.4% capacity retention after 100 cycles) and high rate capability (74 mAh g^{-1} at a high rate of 2C).[116]

However, in order to achieve an even higher energy density Na-ion full cell, asymmetric devices need to be carefully designed and studied. Previous reports about the Na-ion full cell based on a Na storage cathode and a nonmetallic Na anode, and their electrochemical performances are far from a satisfactory breakthrough. Therefore, it remains a challenge to fabricate such a full cell with high safety, outstanding rate capability and cycling stability.
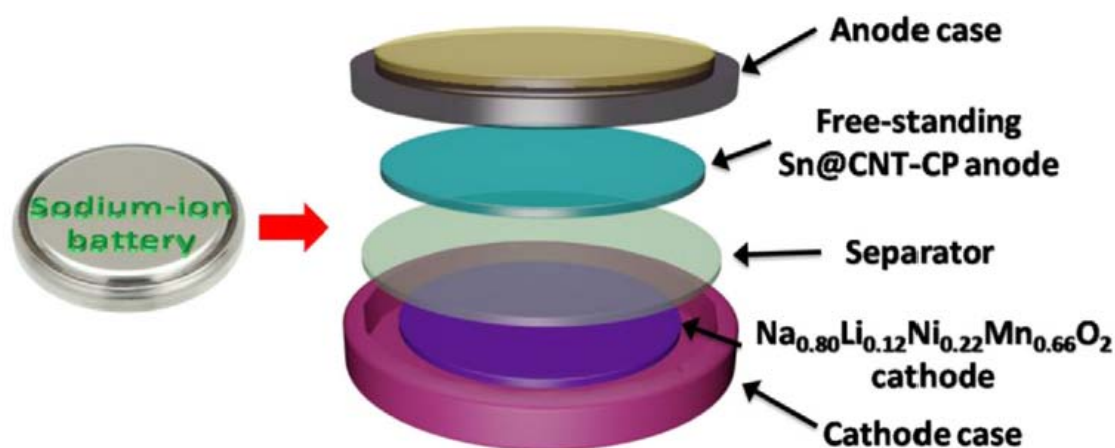
Figure 2-9 Schematic illustration of a full Na-ion battery with $Na_{0.80}Li_{0.12}Ni_{0.22}Mn_{0.66}O_2$ as cathode and free-standing Sn@CNT-CP as anode.[115]

2.6 Challenges of sodium-ion batteries

Due to the fact that Na ion intercalation chemistry is very similar to Li, in the field of positive materials, the replacement of Li by Na has become a common route for finding good electrodes, thus making it possible to employ very similar compounds for both kinds of systems. A wide range of compounds is being investigated as possible SIBs cathodes. Among a variety of positive materials, polyanionic compounds and transition metal, layered oxides show the excellent electrochemical performances. However, in order to achieve the effective application of Na-ion batteries, the identification of suitable negative electrodes still features the big challenge to face. The inability of Na to insert into graphite,

and the up-to-now uncertain formation of a stable SEI layer is hindering the advance towards preparing Na-ion full batteries. In fact, the most recent advances of anode materials for Na-ion batteries have been mainly accompanied by the addition of electrolyte additives or more stable binder compositions. Carbon materials and Ti-based compounds are largely restricted by their low capacities, especially at high rates. In addition, Na-ion full batteries have mainly used $NaTi_2(PO_4)_3$ as anode material, despite its Na insertion occurring at voltages as high as 2.0 V *vs.* Na^+/Na.[89] It is well known that critical battery performance characteristics including reversible capacity, cycle life and rate capability are mainly evaluated by the electrochemical properties of the electrode materials and the electrode architectures. Thus, identifying new anodes or new electrode architectures or both is urgently needed to realize a proper Na storage voltage, large reversible capacity, long cycle life and high structural stability for the enhancement of Na-ion batteries.

3   High-performance SIB anode: Sb

3.1 Features of Sb

Antimony is a member of group 15 and has an electronegativity of 2.05.[117] Sb is stable in air at room temperature, but reacts with oxygen if heated to produce antimony trioxide. The abundance of Sb in the Earth's crust is estimated to be 0.2 to 0.5 parts per million, comparable to thallium at 0.5 parts per million and silver at 0.07 ppm. Even though this element is not abundant, it is found in more than 100 mineral species.[118, 119]

Figure 3-1 displays the crystal structure of Sb . It belongs to rhombohedral phase , which space group is N 166, $R\overline{3}m$, a = b = 0.4307 nm, c = 1.1273 nm. Elemental Sb adopts a layered structure in which layers consist of fused, ruffled, six-membered rings. The nearest and next-nearest neighbors form an irregular octahedral complex, with the three atoms in each double layer slightly closer than the three atoms in the next.[120]
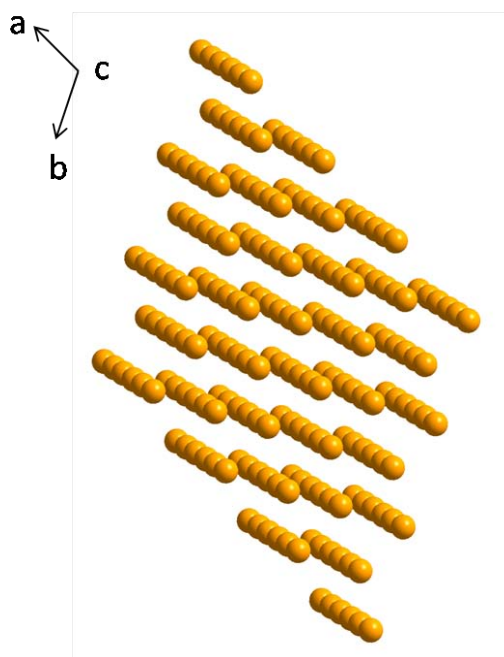
Figure 3-1 The crystal structure of Sb.

Sb has attracted considerable attention as an alternative anode material in Na-ion batteries, because of its high theoretical Na storage capacities (660 mAh g^{-1} or 1890 mAh cm^{-3}) upon full sodiation to Na_3Sb, unique puckered-layer structures, moderate working voltage (0.8-0.9 V), and small electrode polarization ($\approx$ 0.2 V).[121] The puckered-layer structure in a low stacking density (about 39%), could facilitate the fast diffusion of Na ions and the

accommodation of the structure stress, increasing the rate capability and maintaining the electrochemical stability.[6] The small polarization could reduce the self-heating effect upon cycling and the risk of thermal runaway. The moderate discharge voltage could minimize the risk of Na dendrite formation during fast charge process.

The electrochemical reactions in the Sb/Na cells can be seen as follows[122]:

Discharge：$Sb + Na^+ + e^- \rightarrow NaSb$ (1)

$$NaSb + 2Na^+ + 2e^- \rightarrow Na_3Sb_{hex}/Na_3Sb_{cub} \rightarrow Na_3Sb_{hex}$$ (2)

Charge: $Na_3Sb_{hex} \rightarrow Sb + 3Na^+ + 3e^-$ (3)
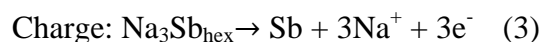
In the discharge process, Sb will alloy with one Na to form NaSb phase, and then NaSb will continue to react with two Na to generate Na_3Sb phase. In the charge process, Na_3Sb phase will dealloy to become Sb phase again.

3.2 Research progress of Sb anode

Commercial bulk Sb is investigated in a Na cell, which delivered a reversible capacity of 540 mAh g^{-1} in the first cycle at the current density of 330 mA g^{-1}, however, after 40 cycles, the capacity decreased to 100 mAh g^{-1}.[122] Wu *et al.* developed Sb nanospheres on graphene *via* oxygen bonds. It revealed that the in-situ constructed oxygen bonds play a significant role on enhancing Na-storage properties, especially the ultrafast charge/discharge capability. The oxygen-bond-enhanced Sb-O-G composite can give a high capacity of 220 mAh g^{-1} at a superhigh current density of 12 A g^{-1}, which is obviously excellent to the similar Sb/G composite (130 mAh g^{-1} at 10 A g^{-1}) just without Sb−O−C bonds.[123] Lou *et al.* synthesized unique Sb@C coaxial nanotube anodes which exhibited excellent Na storage properties. Specifically, it delivered a stable capacity of 240 mAh g^{-1} that can be maintained at 1.0 A g^{-1} even after 2000 cycles. High capacities of 350 mAh g^{-1} and 310 mAh g^{-1} can be obtained at large current densities of 10 and 20 A g^{-1}, respectively.[124] A nanoporous-antimony anode was fabricated by depending on the regulation of the Al-Sb alloy composition. Due to its innovative electrode design, the Sb anode showed a high capacity of 573. 8 mAh g^{-1} after 200 cycles at a rate of 100 mA g^{-1}.[125]

3.3 Challenges of Sb anode

3.3.1 Large volume expansion

Sb anode faces great challenges because of the large volume changes (around 390%) upon sodium insertion into Sb, which lead to fracture and loss of electrical contact as well as

continual solid electrolyte interphase (SEI) growth on the Sb surface, eventually leading to overall capacity loss and failure of the battery.[32, 33] Indeed, pure Sb powders reported a high first capacity of 624 mAh g^{-1}. However, their capacity rapidly faded to be less than 100 mAh g^{-1} after only 25 cycles.[34]

3.3.2 Electrode additive

Most reported Sb anodes are fabricated by using the conventional film-based methods. Traditional paste-based electrodes usually contain the addition of insulating organic binders to inhibit the collapse of the active materials from current collectors, and conductive carbons to keep the electrode conductivity onto the metal current collectors. Actually, the binders make no contribution to Na storage, and the conductive carbon only contributes to the minimal battery performance. In addition, these two components will add a redundant weight, ultimately reducing the specific capacity of the electrode and the energy density of SIBs. What's worse, the presence of binders generally induces insufficient Na ion permeation and blocks electron transport in relation to the reduced available contact area of the active materials and increased polarization of the electrodes.[126, 127] Additionally, the presence of a binder also could lead to thermal runaway, necessitating incorporation of additional safety features in the battery.[128] Therefore, it is urgently needed to develop highly stable Sb structures directly grown on current collectors without using any additives, which can not only effectively decrease the weight of the SIB system, but also enhance the energy density of Na-ion batteries.

3.4 Design strategies of preparing high-performance Sb anode

3.4.1 Conventional optimization methods

3.4.1.1 Electrolyte additive

It is well-recognized that the SEI films formed on the alloy anodes are fragile and easy to damage during repeated cycling, leading to the continuous creation of new surfaces and reconstruction of new SEI films.[129] If these reactions continue to proceed, the SEI films on the anodic alloy particles turn into thicker and denser, thereby showing a loss of the electric contact between the electro-active structures and therefore a rapid deterioration of the electrode. Since fluoroethylene carbonate (FEC) is an effective electrolyte additive for improving SEI films and cycle life, it has been frequently used in Li-ion batteries. FEC can also form a compact SEI film mainly making up of stable alkali fluoride or fluoroalkyl

carbonate in the Sb anode, which can tolerate the volume expansions of the alloy particles at repeated charge and discharge cycles.

To evaluate the long-term cycling stability of the Sb material, Qian *et al.* cycled the Na-Sb/C half cells with and without the addition of 5% FEC. As shown in Figure 3-2, the Sb/C electrode in the FEC-free electrolyte can only be cycled in the first 50 cycles and then failed to give any available capacity after 80 cycles, whereas the Sb/C electrode in the 5% FEC-containing electrolyte can maintain an almost constant capacity of 575 mAh g^{-1} over 100 cycles, exhibiting a superior cycling stability.[34] These very different cycling behaviors can be well accounted for the effect of FEC electrolyte additive on the structural stability of SEI film on the Sb/C electrode.
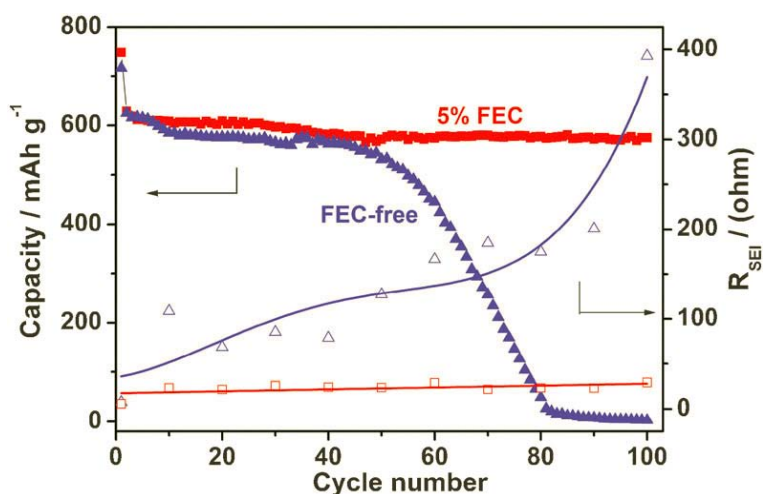
Figure 3-2 Changes of the reversible capacities and SEI film resistances of the Sb/C anodes in the 1.0 mol L^{-1} NaPF$_6$ + EC-DEC electrolyte with (red) and without (blue) the addition of 5% FEC additive.[34]

3.4.1.2 Sb/carbon composite

A large number of Sb/carbon composites are reported to show the improved Na storage performance, such as Sb/MWCNT nanocomposite,[43] Sb nanocrystals embedded in carbon microspheres,[40] Sb nanoparticle decorated N-rich carbon nanosheets,[130] mechanically milled Sb/C nanocomposites,[34] peapod-like Sb@C submicron-structures,[131] rGO/nano Sb.[41] The role of carbon is to not only act as an electrical conduction path, but also use as a barrier to accommodate the aggregation and pulverization of active particles as well as increase the conductivity, which enhance the stability of active materials during cycling. For example, Sb-C nanofiber electrode delivered a large reversible capacity of 631 mAh g^{-1} at C/15, which greatly improved rate capability and superior cycling stability (90%

capacity retention after 400 cycles).[132] The excellent electrochemical performances of the Sb-C nanofibers are owing to the unique nanofiber structure and uniform distributions of Sb nanoparticles in carbon matrix, which offer a conductive and buffering matrix for effective release of mechanical stress caused by Na ion insertion/extraction and prevent the aggregation of the Sb nanoparticles.

3.4.1.3 Sb-based alloy compound

It is suggested that Sb alloys including NiSb,[45, 46] CoSb$_3$,[133, 134] ZnSb,[135-137] Cu$_2$Sb,[49, 50] Mo$_3$Sb$_7$,[138] FeSb$_2$,[139, 140] and SnSb[36, 47] have been proposed to reduce the drastic volume changes and thus to extend the cycle life of this material. In these Sb-based alloy materials, the volume changes and aggregation or coarsening of active Sb elements are diminished and prevented by the electrochemically inactive component which serves as a buffering matrix to maintain the electrode microstructure during the sodiation–desodiation process. For instance, Figure 3-3 exhibits the comparison of cycling performance between BiSb-C composite and Sb-C anodes, in which BiSb-C composite shows the better cycling performance and larger capacities than Sb-C anode.[141] The cycling stability is generally improved by the introduction of an inactive or carbon element. However, this would be simultaneously at the cost of sacrificing some specific capacities compared with metallic Sb.[142]
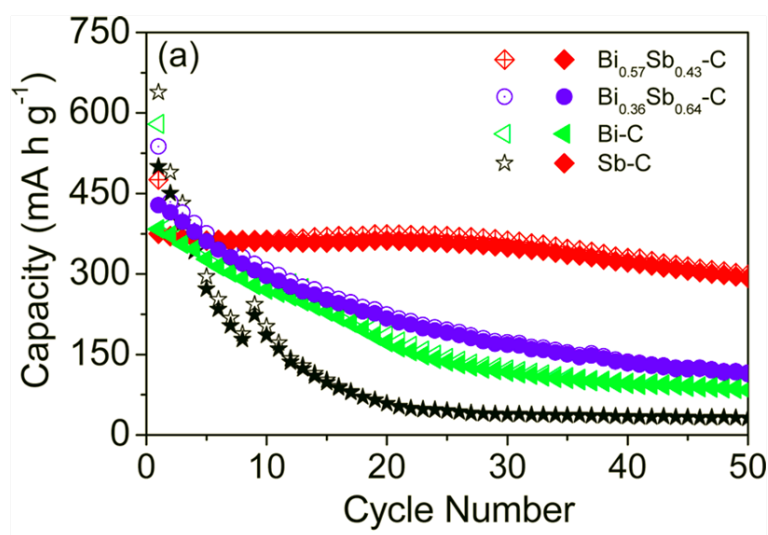
Figure 3-3 Cycling performance of the electrodes (BiSb-C, Bi-C and Sb-C) in SIB at a current density of 100 mA g^{-1}.[141]

3.4.1.4 Metallic Sb with nano/micro morphology

Downsizing of the active material original size to nanoscopic or microscopic forms is presently studied as a major approach for alleviating the effects of the volume variations and to enhance the reaction kinetics.[143] Various Sb morphologies have been studied and showed the enhanced cycling and rate performance, such as Sb porous hollow microspheres,[142] Sb nanocrystals,[40] rod-like Sb–C composite,[144] cypress leaf-like Sb,[145] pitaya-like Sb@C microspheres.[146] Sb porous hollow microspheres (Sb PHMSs) showed a high reversible capacity of 617 mAh g^{-1} at a current density of 100 mA g^{-1} after 100 cycles with a high capacity retention of 97.2%.[142] Even at a high current density of 3200 mA g^{-1}, the reversible capacity can also reach 312.9 mAh g^{-1}. The superior electrochemical performance of Sb PHMSs porous hollow microspheres can be accounted to the unique structural characteristic of Sb with porous and hollow structure, which can mitigate the volume expansion and facilitate the Na^+ diffusion during the repeated sodiation and desodiation processes. Although these reports have confirmed that novel nanostructured designs can deeply alleviate the large volume strain to enhance the electrochemical performance of alloy materials, the relationship between the structural evolution and electrochemical performance during cycling is still far from well understood.[146]

3.4.2 Rational design of hierarchical additive-free anode

To mitigate the massive volume expansion of Sb, designing Sb with special structural features is considered to be an efficient strategy for improved electrochemical performance and high energy density.[40, 125, 144, 146] Sb anodes with various nano-structures have been proposed to deliver enhanced Na-ion storage properties, since nanomaterials can provide short ion and electron diffusion pathways, facile strain relaxation, and large electrode/electrolyte contact areas.[35, 37-39] The disadvantage of nanomaterials is that they are often self-aggregated related to their high surface energy, reducing their available contact areas among active materials, additives, and electrolyte, ultimately leading to a large initial capacity loss, low rate capacity, and poor cyclability.[147] Therefore, it is still a major challenge to maintain the effective contact areas large and fully realize the merits of active materials at nanometer scale.

Hierarchical structures showing a synergistic joining of two different size scales, which usually refer to micro/nanoscale aggregates with well-defined morphologies formed by the self-assemble of nanoscale primary building blocks (*e.g.*, nanoplates,

nanoparticles, and nanorods).[148, 149] So far, hierarchical materials have drawn intensive attentions on improving the properties of chemical sensing, energy storage and conversion, and chromatography, *etc.*[150-156] Besides the small particle size and high specific surface area, structural features such as open porous systems, resistance to aggregation, and large void spaces can also be introduced to a hierarchical architecture through the self-assembly of the building blocks.[151-156] The porous system ensures fast transport of the electrolyte within the electrode. The large surface area increases the electrode/electrolyte contact, facilitating Na ions diffusion. The shortened diffusion distance of Na ions may improve the rate capability of the electrode materials. The large void space within hierarchical structures may buffer the possible volume expansion derived from the insertion of Na ions, leading to good cycling stability of the electrode materials. Another merit of hierarchical structures is the relatively large dimensions, keeping the high tap densities of the electrode materials.[157] The utilization of hierarchical structures may efficiently improve the electrochemical properties of electrode materials. To date, various hierarchically structured electrode materials were fabricated.[158, 159] For example, a hierarchical Sb anode termed cypress leaf-like Sb has been successfully prepared through chemical replacement reaction between commercial Mg powder and Sb^{3+}.[145] In this hierarchical structure, the void space among the branches of cypress can alleviate the volume change and offer active sites for sodiation. Used as SIB anode, it gave a high reversible capacity of 550 mAh g^{-1} after 120 cycles. However, the rate capability is still not satisfactory, where it only showed a capacity of 300 mAh g^{-1} at the current density of 3.2 A g^{-1}.

The reports showed that additive-free anode configuration could provide better rate capability and cycling performance than the traditional paste-based electrode architecture.[57, 160, 161] Conventional paste-based electrodes (*e.g.*, cypress leaf-like Sb) usually contain the addition of insulating organic binders to inhibit the collapse of the active materials from current collectors, and electrical conductors to ensure the electrode conductivity onto the metal current collectors.[51] Actually, the binders make no contribution to Na storage, and the electrical conductor only contribute to the minimal battery performance. Additionally, these two components will greatly decrease the energy density of SIBs. What's worse, the presence of binders generally induces insufficient ion permeation and blocks electron transport, because of reduced accessible contact area of the active materials and increased polarization

of the electrodes.[57] Therefore, it is highly expected to build highly stable hierarchical Sb structures directly grown on current collectors without using any additives, which can not only effectively decrease the weight of the SIB system, but also enhance the energy density of SIBs.[162] Furthermore, the direct growth of hierarchical structures on current collector can guarantee convenient Na ion diffusion pathways and electron transport channels, and ensure sufficient structural interspaces for mitigating the volume expansion, eventually resulting in satisfactory rate performance.[162]

3.4.3 Highly ordered nanostructured arrays based on AAO template

3.4.3.1 Highly ordered nanostructured arrays for batteries

It is worth noting that there are some disadvantages in the majority of currently available commercial ion battery electrodes that are fabricated by mixing active material powders, conductive carbons, and organic binders, forming thin films with the thickness of hundreds of micrometers. First, the ion transport resistance in the electrolyte will be increased in random stacking of the active material and conductive carbon, and then ions cannot reach the bottom of the film. Second, the incomplete contact between ions and the active material can result in unfinished electrochemical reactions, thus showing the loss of storage capacity. Third, since the charges will jump through the inter-particle contact area in the disordered material network, both large ion and electron transport resistance is shown in the electrode, which is harmful to realize great rate capability. Additionally, the extra weight of the additives can lead to more loss of specific capacity, and post-treatment with high pressure and temperature can cause a dense or even damaged structure.

Highly ordered nanostructured array (HONA) is proposed as a promising architecture for a large variety of energy-related applications, due to its superior geometric features.[163-166] When it is applied as electrode for rechargeable ion battery applications, the HONA electrodes possess the oriented nanostructured array directly growing on the conductive substrate that serves as both structure support and current collector. The constructing units of the array can be various, such as nanowalls, nanorods, nanosheets, nanotubes, nanowires, *etc*. Besides the general benefits originating from the morphologic features, the HONA electrodes also own outstanding characteristics that can simultaneously enhance the four transport pathways which are ion transport in the electrolyte, ion transport in the electrode, ions and electrons related in the electrode to finish the electrochemical reaction, and

electron transport in the electrode, respectively. As shown in Figure 3-4, using nanorod array as an example, the characteristics and benefits include[67]:

(a) An interconnected network that facilitates ion transport in the electrolyte: The interval space formed among nanoarrays offers a directional ion transport pathway from electrolyte to reach the interior area of electrode, making it possible that each subunit contributes to the electrochemical reaction; (b) A short ion transport length that decreases ion diffusion resistance in the electrode as small as possible: The ion diffusion resistance in the electrode can be reduced by directly growing the short length scale of the subunits on the current collector; (c) A large surface area that maximizes electrochemical reactions in the electrode: The large surface area can result in more active sites and electrode/electrolyte contact; (d) A directional pathway that facilitates rapid electron transport: The integrated architecture with a strong adhesion to the substrate offers fast electron transport pathways to the current collector; (e) The nanostructured array that accommodates the volume strain of ion insertion along a specific direction: The interval space can serve as a protective structural buffer zone to mitigate the structure damage related to large volume expansion/contraction and against pulverization, agglomeration, and exfoliation of active materials during repetitive charge/discharge cycles. In addition, the robust arrayed structure and strong adhesion between the active material and the substrate can guarantee the stability of the electrode.

In summary, the feature (a) and (c) can contribute to large reversible capacity for the HONA electrodes, the feature (b) and (e) donating long cycle life, and the feature (b) and (d) promoting high rate capability. Furthermore, HONA electrodes also are the additive-free electrodes which omit the complicated electrode fabrication processes and reduce the cost of battery system.
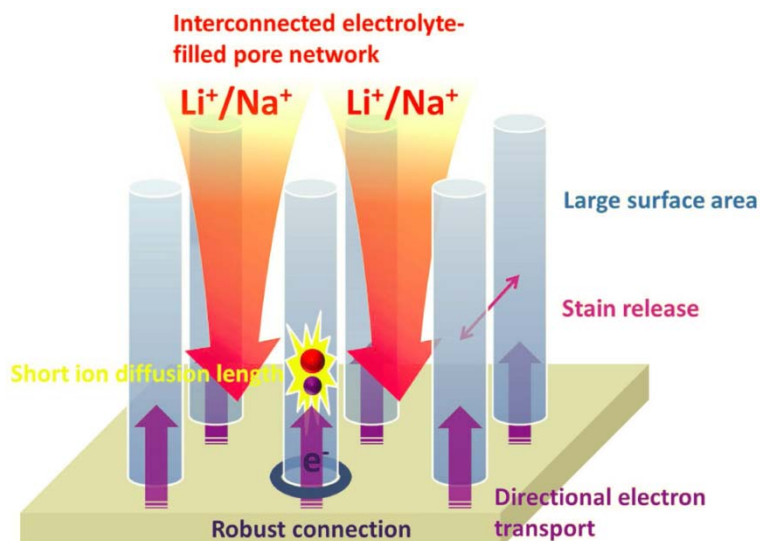
Figure 3-4 Schematic of the HONAs showing their outstanding characteristics.[67]

HONA electrodes have been extensively applied to rechargeable ion batteries. Self-supported $Li_4Ti_5O_{12}$-C nanotube arrays directly growing on stainless steel foil were fabricated as LIB anodes.[167] Due to the short Li^+ diffusion distance, large contact surface area, good conductivity, and the stable nanotube arrays, the anode showed remarkable rate capability (a reversible capability of 135 mAh g^{-1} and 80 mAh g^{-1} at 30 C and 100 C, respectively) and cycling performance (about 7% capacity loss after 500 cycles at 10 C). SnO_2 nanorod arrays were prepared on large-area metallic substrates (Figure 3-5a and b), delivering a reversible capacity of as high as 580 mAh g^{-1} after 100 cycles and showing excellent rate capability (350 mAh g^{-1} at the 5C rate).[168] By contrast, the disordered SnO_2 nanorods and nanoparticles of SnO_2 mixed with carbon and polymer binder, revealed reversible capacities of only 465 and 350 mAh g^{-1} after 30 cycles (Figure 3-5c).
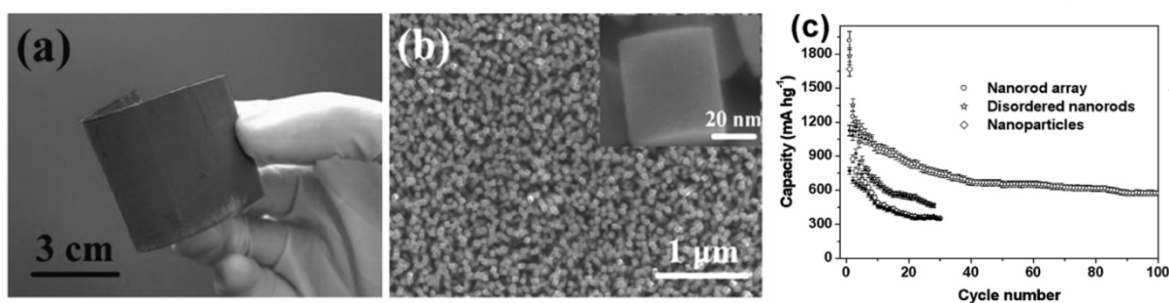
Figure 3-5 (a) Optical image, (b) top-view SEM image of the as-prepared SnO_2 arrays on a large-area alloy substrate. Inset in (b) reveals an individual rod. (c) Cycling performance at the rate of 0.1 C for the nanorod array, disordered nanorods, and nanoparticles, respectively.[168]

Inspired on the above prominent features of the HONA electrode and associated excellent electrochemical performance, it is highly desired to apply this HONA design into the material of Sb, thereby improving its electrochemical performance.

3.4.3.2 Template-directed growth

In general, template-directed growth is a convenient and versatile preparation method used to generate nanomaterials or the dismounting of bulk materials into the desired structures. Any substance with nano-patterned features, including natural and artificial nanostructured materials, can be devoted as templates for the construction of nanostructure arrays. To date, much effort has been used to preparing electrodes of rechargeable ion batteries using templates. According to the requirement that the HONAs should directly grow on conductive substrates so that obtained electrodes don't involve any binders or conductive additives, hard templates are dominantly applied in this regard. The "hard templates" generally are defined with well-confined pores in the form of channels, or connected hollow spaces. Normally, the fabrication process includes three steps: (a) precursors fill in templates through incorporation or impregnation; (b) products grow through reactions; (c) products are achieved by etching templates. Numerous materials (*e.g.*, metals, polymers and semiconductors) can be constructed into nanoarrays through template-directed strategies by integrating various synthetic techniques, such as atomic layer deposition (ALD), electrochemical deposition (ED), chemical vapor deposition (CVD), and physical vapor deposition (PVD), sol-gel process, *etc*.

Template-directed synthesis provides distinct advantages for energy-related device applications. First, due to its flexibility and simplicity, preparing the large-scale nanostructure arrays is easily realized by using template-directed growth, which is significant for practical applications. Second, template-directed nanostructure arrays have flexible structural controllability in nano-scale dimensions, such as shape, interval space, size, *etc.*, which is highly favorable for the performance optimization of energy-related devices. Third, the spatial orientation or arrangement of template-directed nanostructure arrays can be predefined by the spatial structure of the templates. By adjusting the spatial orientation/alignment of these nanostructure arrays, the performance of energy devices can be further enhanced. Fourth, the template-directed method is an efficient way to fabricate HONAs that can be easily obtained on the basis of some highly ordered templates (*e.g.*, porous anodic aluminum). Depending on the above merits, template-directed approach has great potentials for constructing HONAs for highly efficient energy storage and conversion

devices, mainly including batteries, supercapacitors, solar water splitting devices and photovoltaic devices.

3.4.3.3 AAO template

Since 1995, when Masuda et al. developed a two-step anodization process to prepare well-ordered anodic aluminum oxide (AAO) nanoporous strucutre,[169] AAO template has inspired intensive interests for fabricating HONAs. As can be seen in Figure 3-6, AAO template has a self-ordered, honeycomb-like and highly-oriented pore structure, with tunable pore diameter, pore density, pore length and inter-pore distance, which is obtained by anodizing aluminum (Al) foil under proper conditions (potential, acid and temperature).[169-171] By changing the acid and potential as well as wet-chemical pore-widening process, the pore diameter and density can be tuned in a wide range of 10-400 nm and 109-1011 pore cm^{-2}, respectively. By changing the anodization time, the pore length can be tuned from several tens of nanometers to several tens of micrometers.[172]
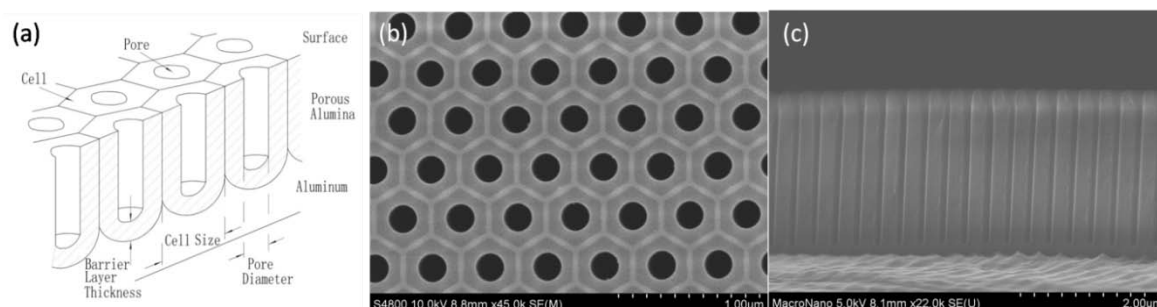
Figure 3-6 (a) Schematic structure of AAO template after the anodization on Al foil. SEM images of AAO template: (b) top surface, (c) cross section.

It should be noted that the high controllability of the geometric parameters of the AAO template leads to the high controllability of the obtaining arrays because the formed solid product inside the pores replicates the shape of the void space in the template. Thereby, during the last decades, AAO template has been extensively developed in the fabrication of various ordered nanostructure arrays of nanopores,[173-175] nanowires,[176, 177] nanotubes,[176, 178] nanodots,[179] and nanocones.[180] Due to the high compatibility of the AAO template integrated with various synthetic techniques, many kinds of materials can be fabricated into nanostructure arrays, such as metal,[181-183] polymers,[184, 185] carbon,[186-189] semiconductors,[190-192] and organic materials.[177, 193, 194] Moreover, nanostructure arrays with multi-components and multi-segments could also be achieved by using AAO template.

Thus, AAO template offers a good scaffold to fabricate nanostructure arrays for practical device applications.

The AAO template prepared through self-organization process has a poly domain structure, meaning the honeycomb-like pore arrangement is in short-range order but long-range disorder, consequently resulting in the same arrangement of the obtained nanoarrays. To achieve perfectly ordered nanoarrays, nanoimprinted AAO templates have been largely developed recently,[195-198] which are fabricated by anodizing the surface pre-patterned Al foil.[169] Compared with the short-range ordered pore arrangement of the self-organized AAO, the pore arrangement and inter-pore distance of the nanoimprinted AAO are only decided by the initial surface patterns that have a long-ranged order and different pore arrangements (triangular, rectangular and hexagonal). Therefore, such perfectly ordered arrangements can be well succeeded by the resulting nanoarrays.

3.4.4 Multi-dimensional electrodes

Three-dimensional (3D) architecture showing a periodic array of current collector and effective inclusion of active materials has been proposed as a promising LIB electrode configuration to maximize power and energy density and simultaneously maintain short ion transport distance.[199-203] Unfortunately, to date, little has been done on the end of SIBs regarding such 3D heterostructured electrode.[204, 205] Owing to the relatively large size of the Na ion, facile electron and ion transport as well as stable electrode structure play an important role on enhancing electrochemical performance, especially rate capability, for a material with intrinsically low electric conductivity. Highly ordered 3D metallic core/active shell nanoarrays have attracted extensive attention in LIBs, because they can simultaneously provide sufficient electrons and short ion diffusion pathway, as well as rigid electrode frame resulting from the robust electric contact between the structural components and substrate, as seen in Figure 3-7.[205] The electrochemically inactive components (3D current collector) have high hardness to provide structural integrity to the active material, thereby improving capacity retention.[206]
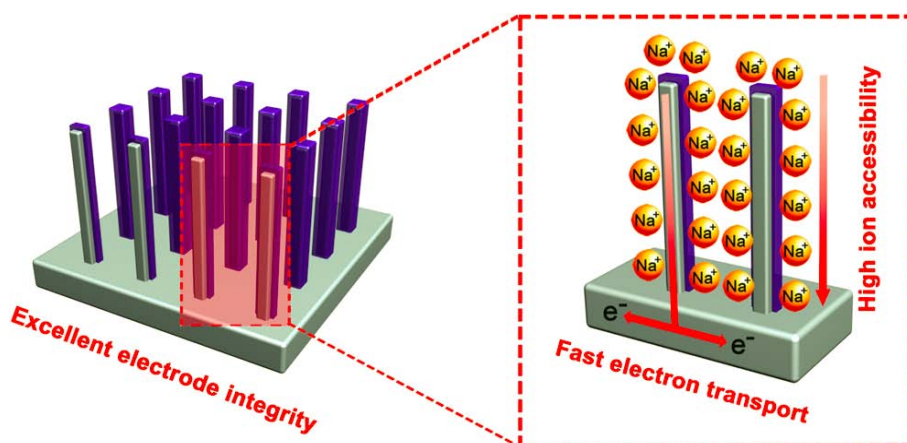
Figure 3-7 Schematic illustration of the highly ordered 3D electrode configuration with arrayed current collector.

In specific, the conductive metal core was grown on the current collector forming a 3D current collector substrate, which allows for effective electron transport to enhance the high rate capability. Besides, the robust metal core provides structural reinforcement to overcome the mechanical damage during the volume expansion and contraction of the active shell. Moreover, the space between the nanoarrays can improve ion accessibility and accommodate large volume change of active shell.[200] Highly ordered 3D metallic core/active shell nanoarrays greatly benefits from the use of group-IVA and group-VA elements such as Si, Ge, Sn, Bi, and Sb. For example, 3D nanoarchitectured current collectors consisting of 1D Cu/C core/sheath nanowires were fabricated as LIBs anodes, which exhibited a large reversible capacity of 933 mAh g^{-1} at a rate of 1 C over 1000 cycles and an excellent rate capability of 1017 mAh g^{-1} at a rate of 10 C over 200 cycles.[207] Tin-coated viral nanoforests (3D C/Sn/Ni/TMV1cys) binder-free composite electrode evenly assembled on a stainless steel current collector, and exhibited supreme capacity utilization and cycling stability toward Na-ion storage and release. An initial capacity of 722 mAh (g Sn)$^{-1}$ along with 405 mAh (g Sn)$^{-1}$ retained after 150 deep cycles.[204] Additionally, this 3D multi-dimensional current collector structure can possibly avoid any use of binders or conductive additives, which would add extra weight to the battery. These advantages inspire us to apply this electrode design on the end of Sb anode.

3.4.5 Summary

To achieve Na-ion batteries with both high energy and power densities, it is necessary to understand the Na ions and electrons transport mechanisms inside a SIB system. Whether

it is a charge or discharge process, the transport pathways of the charges normally involve: (1) Na ion transport in the electrolyte to arrive at the electrode/electrolyte interface; (2) Na ion diffuse in the electrode; (3) Na ions and electrons be related in the electrode to fulfill the electrochemical reaction; (4) electron transport in the electrode and current collector. The kinetics limitation can be greatly reduced by decreasing the resistances of the above four transport pathways at the same time, which should be the guideline for rationally designing the electrode architectures.

Therefore, based on the above mentioned four transport pathways, we propose three different electrode architectures which are hierarchical additive-free structure, highly ordered nanostructured arrays, and multi-dimensional current collectors, respectively. All three architectures can be well applied to Sb anode. The resulting Sb structures can not only address the challenges of Sb anodes (large volume changes and electrode additives) but also simultaneously reduce the resistances of the above four transport pathways. As a result, large capacity, long cycle life and high rate capability can be realized in Sb anodes for Na-ion batteries.

4 Experiments and instrumentations

All experiments and methods throughout this dissertation are performed and carried out according to the procedures described in this section. The structures are fabricated from a combination of imprinted AAO templating technique and electrochemical deposition method. The morphology, chemical composition, and structural features of the nanostructures are investigated by X-ray diffraction spectroscopy (XRD), Field emission scanning electron microscopy (SEM), Transmission electron microscopy (TEM), Energy-dispersive X-ray spectroscopy (EDX). The device measurements are conducted by the electrochemical workstation and LAND-CT2001A test system (Wuhan, China).

4.1 Synthesis techniques

4.1.1 Nanoimprinted AAO templating technique

Nanoimprinted AAO template was prepared using nanoimprinting technique followed by an anodization process. Clean high-purity (99.99%) Al foil of about 0.22 mm thickness was used as the starting material. The Al foil was first successively washed with acetone and ethanol for 10 min, and then it was electrochemically polished in a 1:7 (v:v) solution of perchloric acid ($HClO_4$) and ethanol at a voltage range of 20-30 V.

The nickel (Ni) imprinting stamp was placed on polished Al foil, and the imprinted Al foil was achieved using an oil pressing system under a pressure of about 10 kN cm^{-2} for 3 min. Then the anodization was performed at a constant voltage of 160 V in 0.4 M phosphoric acid (H_3PO_4) at 5°C for 30 min, in which the anodization voltage was chosen to satisfy the distance periods in the imprinting stamp according to the linear relationship (2.5 nm V^{-1}) between the interpore distance (400 nm) and anodization potential (160 V). After anodization, a 50 nm thick layer of Au were evaporated by using physical vapor deposition (PVD), and then a thick layer of Ni was electrochemically deposited on the top of the AAO template with Au as current-carrying substrate, where Au was used to improve the adhesion between Ni layer and template. The backside Al was removed by a mixture solution of copper (II) chloride ($CuCl_2$, 85 wt%) and hydrochloric acid (HCl, 15 wt%), and then was transferred to H_3PO_4 solution (5 wt%) at 30 °C to remove the barrier layer and widen the size of the pores. The time for the barrier layer removal and pore-widening process depends on the desired sizes of pores in the AAO template. At last, a through-pore

AAO template with conductive substrate was obtained. The fabrication procedure is schematically illustrated in Figure 4-1.
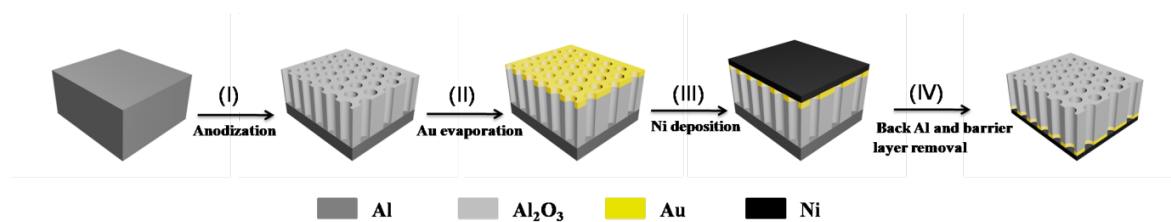
Figure 4-1 Schematic illustration of the fabrication processes of nanoimprinted AAO template.

4.1.2 Electron beam physical vapor deposition

Electron beam physical vapor deposition is a form of physical vapor deposition (PVD), in which a target anode is bombarded with an electron beam given off by a charged tungsten filament under high vacuum. The electron beam causes atoms from the target to transform into the gaseous phase. These atoms then precipitate into solid form, everything in the vacuum chamber (within line of sight) with a thin layer of the anode material.[208, 209] In this dissertation, the deposition of Au is carried out using Kurt J. Lesker.

4.1.3 Electrochemical deposition

Electrochemical deposition (ED) is a facile and cost-effective method that has been widely applied to prepare films or electrode materials with various morphologies, due to the following advantages: (i) the morphology and thickness of the nanostructure can be precisely controlled by changing the electrochemical parameters, (ii) relatively uniform and compact depositions can be prepared in template-based structures, (iii) higher deposition rates are achieved, and (iv) the equipment is not expensive because of the non-requirements of either a high reaction temperature or a high vacuum.[210] All the electrochemical depositions in this dissertation are conducted using electrochemical workstation (BioLogic, Inc.).

4.1.3.1 Deposition of Ni film and Ni nanorods

Ni film deposition was carried out in a Ni plating solution containing 8.41×10^{-2} M Nickel (II) chloride ($NiCl_2$, Sigma-Aldrich), 1.59 M Nickel sulfamate (II) tetrahydrate ($Ni(SO_3NH_2)_2\cdot4H_2O$, Sigma-Aldrich), and 0.33 M Boric Acid (H_3BO_3, Sigma-Aldrich). The AAO template and Ni foil were used as the working electrode and the counter

electrode, respectively. The current density for Ni film was 10 mA cm^{-2}. Ni nanorods were deposited with a current density of 2.0 mA cm^{-2} in the same Ni plating solution.

4.1.3.2 Deposition of fern leaf-like Sb

3.6 mmol antimony trichloride (SbCl$_3$, Sigma-Aldrich) was dissolved in 100 mL ethylene glycol under vigorous magnetic stirring for 30 min. The electrodeposition was conducted in a two-electrode cell with Ti foil as the working electrode and platinum (Pt) foil as the counter electrode at a constant current density of 1.0 mA cm^{-2}. The product was washed with ethanol and deionized water, and dried at 80 °C under vacuum.

4.1.3.3 Deposition of Sb nanorod arrays

Sb nanorod arrays were electrodeposited inside the above nanoimprinted AAO templates at a constant current density of 1.0 mA cm^{-2} in an electrolytic bath containing SbCl$_3$ and sodium citrate (C$_6$H$_5$Na$_3$O$_7$·2H$_2$O). The electrodeposition was conducted in a two-electrode cell with AAO template as the working electrode and Pt foil as counter electrode. Sb nanorod arrays are released by dissolving the AAO template in a sodium hydroxide solution (NaOH, 3.0 M) for 30 min, followed by a rinsing process with deionized water. As reference samples, A-Sb NRs, A-2-Sb NRs, and A-2-Sb NRs were also prepared using the similar procedures. The fabrication processes can be found in Figure 4-2.
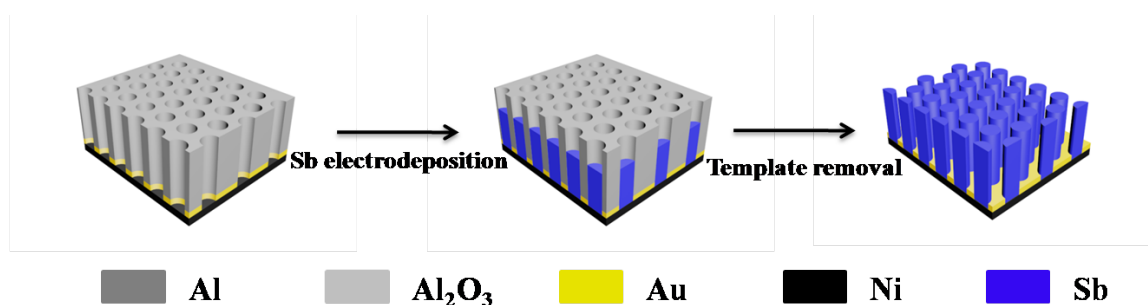
Figure 4-2 Schematic illustration of the fabrication processes of Sb nanorod arrays by using the nanoimprinted AAO templating technique with the assistance of an electrodeposition process.

4.1.3.4 Deposition of 3D Sb-Ni nanorod arrays

Ni nanorod arrays were released by dissolving the AAO template in a NaOH solution (3.0 M) for 30 min, followed by a rinsing process with deionized water. The Ni nanorod arrays were immersed in an electrolytic bath containing SbCl$_3$ and Na$_3$C$_6$H$_5$O$_7$·2H$_2$O, and then placed in the vacuum oven for a while. 3D Sb-Ni nanoarrays were prepared by

electrodepositing Sb on Ni nanorod arrays at a constant current density of 1.0 mA cm^{-2}. The electrodeposition was also conducted in a two-electrode cell with Ni nanorod arrays as the working electrode and Pt foil as the counter electrode.

4.1.4 Co-precipitation synthesis of layered P2-Na$_{2/3}$Ni$_{1/3}$Mn$_{2/3}$O$_2$

The P2-Na$_{2/3}$Ni$_{1/3}$Mn$_{2/3}$O$_2$ was prepared by a co-precipitation method with nickel and manganese nitrates in a stoichiometric amount with sodium hydroxide. Sodium carbonate (Na$_2$CO$_3$) was added afterward as the sodium source. The calcinations were taken at 600 °C for 4 h and 900 °C for 10 h in air.

4.1.5 Sol-gel synthesis of Na$_3$V$_2$(PO$_4$)$_3$/C

Na$_3$V$_2$(PO$_4$)$_3$/C was prepared by using a typical sol-gel method. Citric acid (C$_6$H$_8$O$_7$, 0.2627 g), NaOH (0.515 g), ammonium metavanadate (NH$_4$VO$_3$, 0.9746 g), and ammonium dihydrogen phosphate (NH$_4$H$_2$PO$_4$, 1.4375 g) were added into 200 mL deionized water under constant stirring at 80 °C. After several hours, most of the water was evaporated. Then, the solution was dried at 80 °C for 12 h under vacuum. The mixture were then preheated at 300 °C for 4 h and heated at 850 °C for 8 h under nitrogen (N$_2$) atmosphere to obtain Na$_3$V$_2$(PO$_4$)$_3$/C sample.

4.2 Analysis instruments

4.2.1 Field emission scanning electron microscopy

Field emission scanning electron microscope (FESEM) is a very useful tool for high resolution surface imaging in the fields of nanomaterials science. Electrons are released from a field emission source and accelerated in a high electrical field gradient. Within the high vacuum column, these so-called primary electrons are focused and deflected by electronic lenses to generate a narrow scan beam that bombards the object.[211, 212] In result, secondary electrons are emitted from each spot on the object. The velocity and angle of these secondary electrons involves the surface structure of the object. A detector catches the secondary electrons and delivers an electronic signal. This signal is amplified and transformed to a video scan-image that can be observed on a monitor or to a digital image that can be saved and processed further. Meanwhile, energy-dispersive detector X-rays (EDX) emitted from the sample owing to the high-energy electron beam penetrating into the sample.[213, 214] X-ray spectra can be collected and analyzed, delivering quantitative elemental information about the sample. A "standardless" routine is used, which produces

an accuracy of 1-2% and sensitivities for some elements down to 0.1% by weight. Line scanning and X-ray mapping can also be obtained. SEM measurements and parts of TEM measurements in this dissertation were carried out on an ultra-high resolution Hitachi S4800 FE-SEM at 8 to 15 mm working distance with acceleration voltages in the range of 10 to 30 KeV. EDX measurements were conducted using Auriga Zeiss FIB system equipped with Oxford detector.

4.2.3 Transmission electron microscopy

The transmission electron microscope (TEM) is a very powerful tool for material science. A beam of electrons is transmitted through an ultra-thin specimen and interacts with the specimen as the beam of electrons passes through it.[215, 216] An image is formed from the interaction of the electrons transmitted through the specimen. The image is magnified and focused onto an imaging device. The TEM operates on the same basic principles as the light microscope, but the TEM uses electrons instead of light. Since the wavelength of electrons is much smaller than that of light, the optimal resolution attainable for TEM images is many orders of magnitude and it is better than that from a light microscope. Therefore, TEM can be used to investigate features such as the crystal structure and features in the structure like grain boundaries and dislocations. Chemical analysis can also be conducted. TEM can be used to study the growth of layers, their defects and composition in semiconductors. High resolution can be used to analyze the shape, quality, size and density of quantum wells, dots and wires. The TEM measurements in this dissertation were performed on a Tecnai 20 S-Twin from Philips and a FEI Titan 80-300 operated at 300 KV.

4.2.4 X-ray diffraction spectroscopy

X-ray diffraction (XRD) is a rapid analytical technique primarily. It is used for phase identification of a crystalline material and can show information on unit cell dimensions. The XRD measurements in this dissertation were performed on a Bruker-axs Discover D8 radiation equipment, using the Cu Kα (1.54056 Å) radiation.

4.3 Electrochemical characterization

Electrochemical measurements of half cells were taken using CR2032 coin-type cells with sodium metal as both counter and reference electrode, and the electrode configuration can be seen in Figure 4-3. The Sb materials were used anodes without any additives of

conductive carbon and binder. P2-$Na_{2/3}Ni_{1/3}Mn_{2/3}O_2$ was employed as the cathode which was prepared by mixing 80% P2-$Na_{2/3}Ni_{1/3}Mn_{2/3}O_2$, 10% acetylene black, and 10% poly(vinylidene fluoride) (PVDF) by weight with an appropriate amount of 1-methyl-2-pyrrolidinone (NMP). The above mixture was pressed onto an Al foil which served as a current collector with a subsequent drying process at 120 °C in vacuum for 12 h. $Na_3V_2(PO_4)_3$/C positive electrode was also prepared using the above steps and mass ratios. The full cell was assembled using Sb materials as negative electrodes and P2-$Na_{2/3}Ni_{1/3}Mn_{2/3}O_2$ or $Na_3V_2(PO_4)_3$/C as positive electrodes. The full cells were excessive positive electrode mass.

The coin batteries were assembled in a nitrogen-filled glove box with a glass fiber separator (Whatman, GFB/55) and the electrolyte solution of 1.0 M $NaClO_4$ in EC: PC (1:1 by volume) with the addition of 5% fluoroethylene carbonate (FEC). Cyclic voltammetry (CV) was tested on an electrochemical workstation (BioLogic VSP potentiostat). Electrochemical impedance spectroscopy (EIS) was also conducted on a BioLogic VSP potentiostat with the frequency of 1 MHz to 10 mHz. The galvanostatic charge-discharge tests were performed at various current densities on a LAND-CT2001A test system (Wuhan, China). All of these experiments were conducted at room temperature.
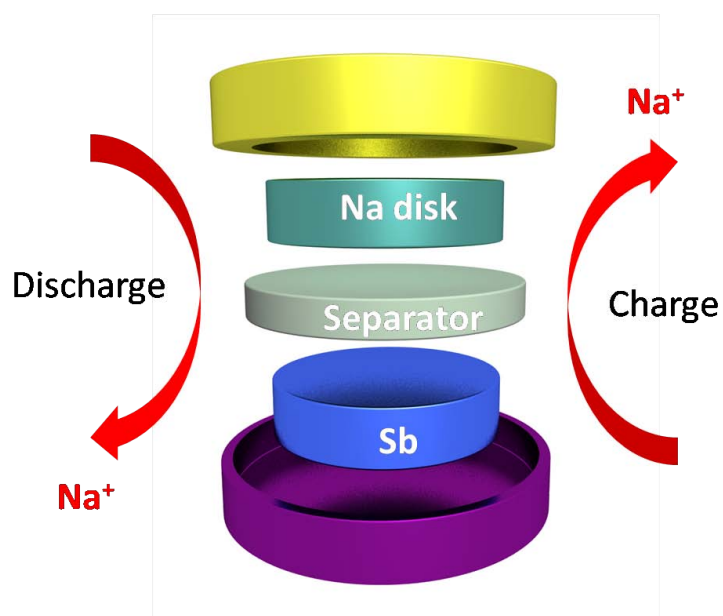
Figure 4-3 Schematic illustration of a half Na-ion battery with Sb as the working electrode and Na disk as the counter electrode.

5 Results and discussions

In this chapter, focusing on the challenges of Sb anode (large volume change and electrode additives), we rationally designed three different types of Sb electrode architectures. In return for these electrode designs, high ion accessibility, fast electron transport, and strong electrode integrity are presented here. Used as additive-free anodes for Na-ion batteries, they exhibit greatly improved electrochemical performance. The structural factors that affect the Na-ion storage properties and electrochemical reaction mechanisms are also investigated in detail. Moreover, the successful application of the three Sb structures in Na-ion full cells further confirms their feasibility in practice. These excellent electrochemical performances shall pave a way to develop more interesting and useful of Sb structures in energy storage devices.

5.1 Hierarchical fern leaf-like Sb as additive-free SIB anode

Hierarchical structures have attracted extensive attention due to the synergistic effects of their nanometer-sized building blocks and overall micrometer-sized structures. These hierarchical structures not only provide characteristic size effects, but also give desirable mechanical strength, facile ion transportation. Meanwhile, fabricating additive-free electrodes to yield favorable electrochemical performance is a hot spot of current research in the energy storage area. Hence, we synthesized a hierarchical Sb structure directly grown on Ti substrate using one-step electrochemical deposition. Structural and morphological characterizations reveal that the as-prepared hierarchical Sb is composed of well-crystallized Sb nanoparticles, finally showing the morphology of fern leaf. The growth mechanism of fern leaf-like Sb was also further investigated. It exhibits desirable properties for Na-ion storage, such as high electrical conductivity and large surface area. Applied as the additive-free anode for SIB, hierarchical Sb shows excellent cycling stability and rate capability, which can be accounted to its morphological and structural features that can ensure the fast electron and ion transport, and stable electrode structure. We believe that the excellent performance of Sb obtained here shall arouse increasing attention on preparing more interesting and efficient hierarchical Sb electrodes without any additives for energy storage devices.

5.1.1 Structural and morphological investigations

The crystallographic structure and phase purity of the as-prepared Sb sample is examined by XRD, as shown in Figure 5-1. Except for the reflections of the substrate (Ti), the rest of diffraction peaks can be indexed to the rhombohedral Sb phase (JCPDS No. 35-0732). No impurity diffraction peaks, such as antimony oxides, were seen, suggesting the successful synthesis of pure crystalline Sb phase.
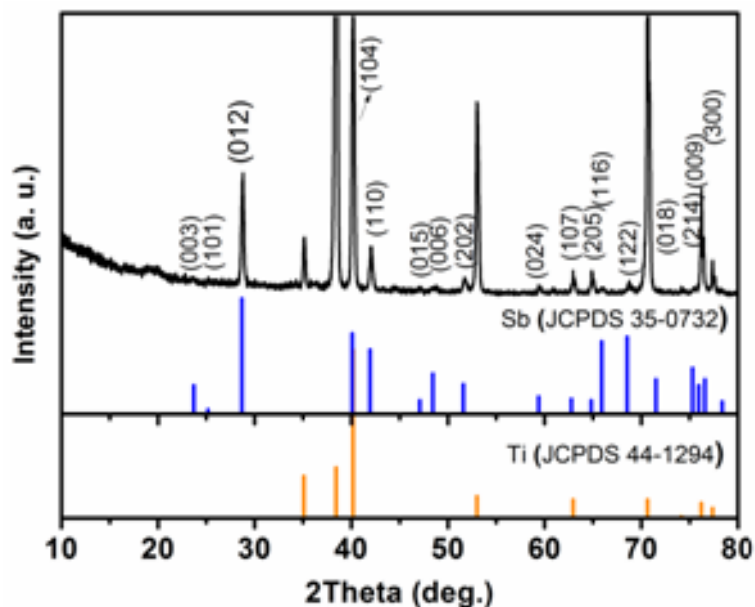
Figure 5-1 XRD pattern of fern leaf-like Sb.

The representative SEM images provide the morphological information of the as-prepared Sb sample. The low magnification SEM image in Figure 5-2a confirms the formation of a large number of hierarchical Sb structures, in which hierarchical Sb is uniformly distributed in a large-area on the Ti foil. Figure 5-2b reveals hierarchical Sb with a diameter of about 0.5 to 1 μm and a length of 1.5 to 3 μm. These hierarchical Sb structures still retain much space among the leaves, forming a porous morphology that could facilitate electrolyte penetration to reach the interior side of Sb structure as well as offer extra space to relieve volume expansions and contractions of Sb upon cycling. Figure 5-2c and d exhibit the magnified SEM images, where many nanoparticles can be seen and they irregularly stack together to show a fern leaf-like morphology.
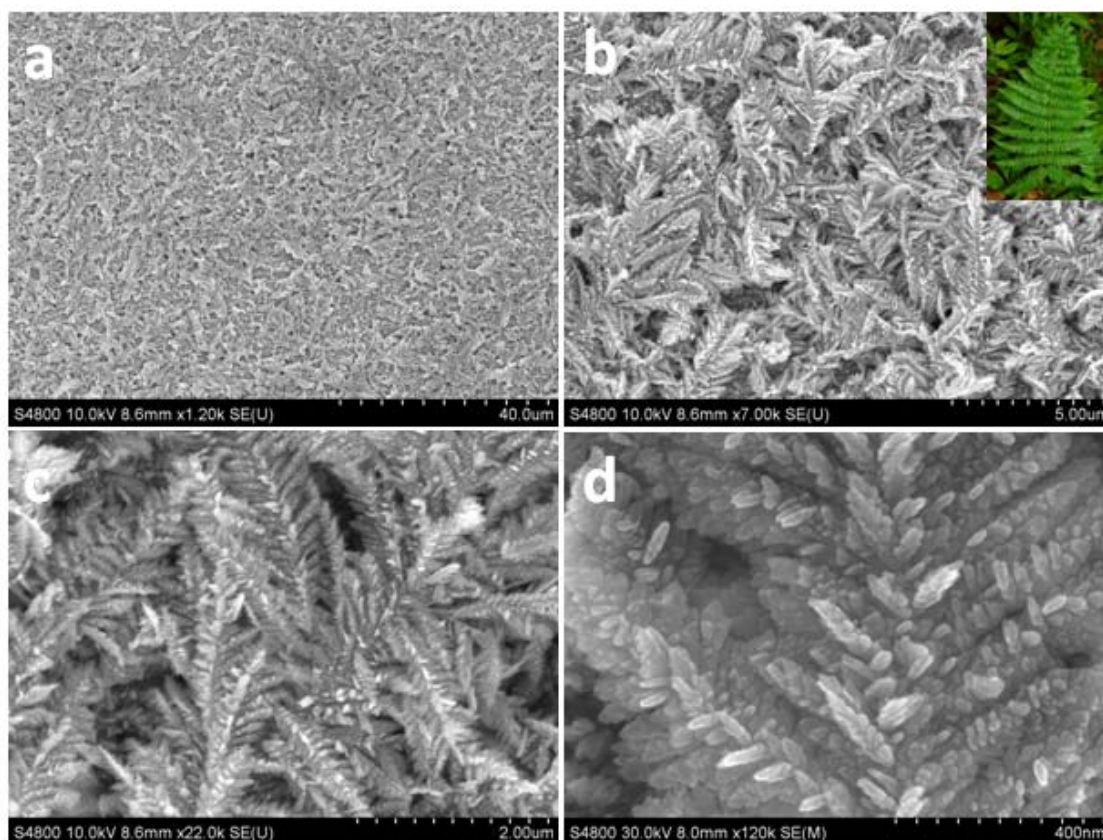
Figure 5-2 SEM images of fern leaf-like Sb, (b inset) a photo of a fern leaf.

TEM image (Figure 5-3a) further shows the well-defined fern leaf-like structure, where the nanoparticles are exhibited in a much clearer way and some are highlighted in red circles. As seen in Figure 5-3b, the average size of nanoparticles is from 20 to 70 nm. Figure 5-3c further presents a HRTEM image of this fern leaf-like Sb. It is obvious that clear lattice fringes can be observed, which shows its crystalline nature. Additionally, the lattice fringe with distances of 3.73, 3.11, and 2.30 Å correspond to the (003), (012), and (104) planes of the rhombohedral Sb, respectively, indicating the high crystallinity of fern leaf-like Sb. The selected area electron diffraction (SAED) pattern in Figure 5-3d proves that the fern leaf-like Sb is polycrystalline.
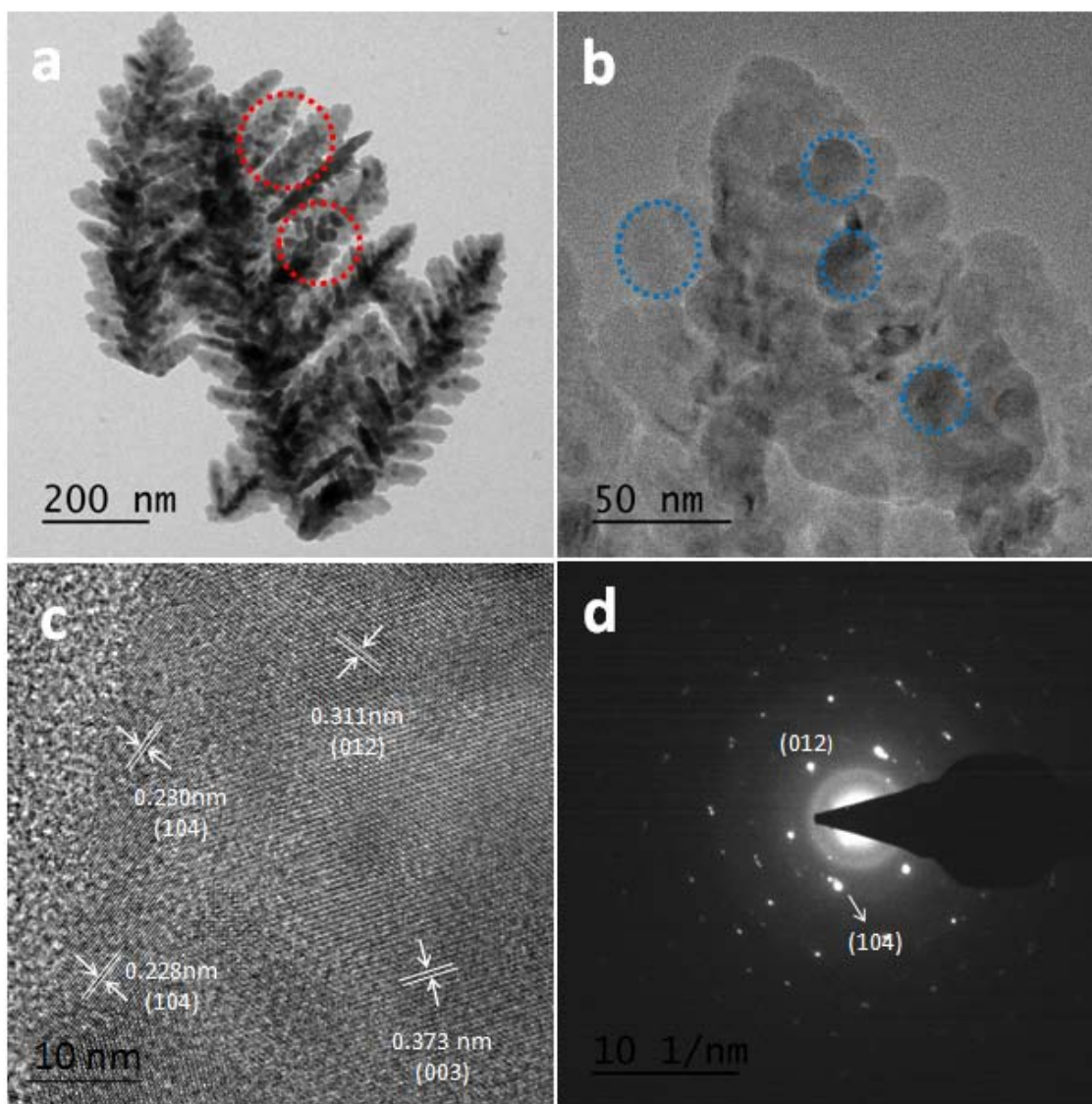
Figure 5-3 (a, b) TEM images, (c) HRTEM image, and (d) SAED pattern of fern leaf-like Sb.

5.1.2 The formation mechanism of the fern leaf-like Sb

The growth mechanism of fern leaf-like Sb is illustrated in Figure 5-4. In the initial stage, Sb nanoparticles uniformly dispersed on Ti foil. With increasing deposition time, due to the strong crystalline anisotropy, Sb nanoparticles directionally aggregated, and the large aggregated particles grew along the preferred growth direction, resulting in the formation of the fern leaf-like structure.[145, 217-220] The time-dependent morphology of the products is presented in Figure 5-5. When the electrodeposition time is 3 min, a large number of nanoparticles are presented (Figure 5-5a), implying that in the initial stage, the preferred morphology is nanoparticles. With the oriented aggregation prcocess proceeding, the

growing fern leaf-like structure is constructed (Figure 5-5b and c). Lastly, well-defined fern leaf-like Sb is achieved, as shown in Figure 5-5d.
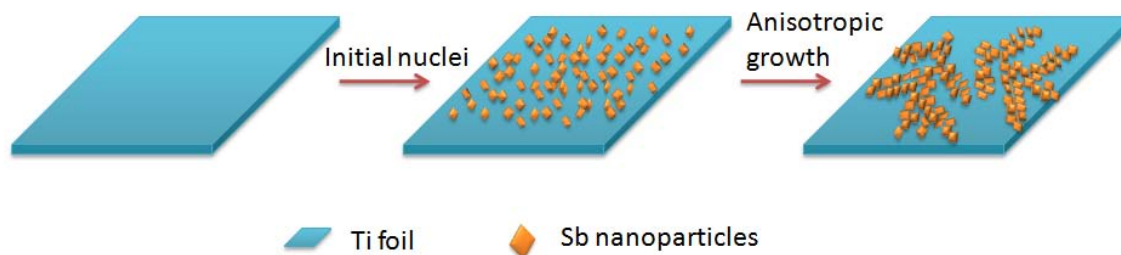
Figure 5-4 Scheme illustration of the formation of fern leaf-like Sb on Ti foil.
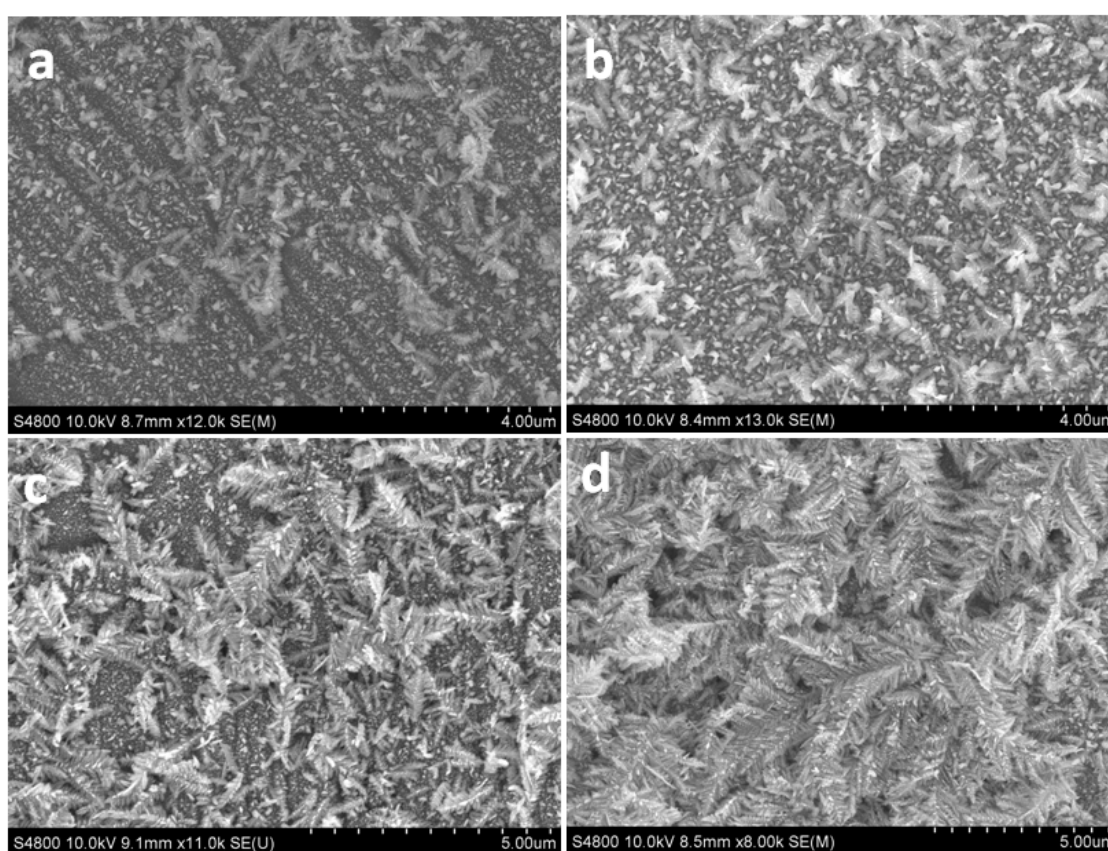
Figure 5-5 Fern leaf-like Sb prepared in different electrodeposition time: (a) 3 min, (b) 5 min, (c) 10 min, (d) 15 min.

5.1.3 Na-ion half-cell performance

To evaluate the SIB performance motivated by its unique structural characteristics, fern leaf-like Sb was employed as an additive-free anode for SIB. Cyclic voltammograms (CVs) were taken of the samples within a potential window between 0.01 and 2 V (*vs.* Na/Na$^+$) at

a scan rate of 0.5 mV s^{-1} to investigate the electrochemical reactions that occur during the initial three Na-ion sodiation/desodiation cycles (Figure 5-6a). In the first cathodic scan, there is only one strong broad peak located at 0.33 V, corresponding to the combination of the formation of a SEI layer and Na$_x$Sb alloy which is subsequently transformed into Na$_3$Sb. During following cathodic scans, three reduction peaks located at 0.6, 0.4 and 0.35 V are observed, which could be due to the multistep transformation of Sb into hexagonal Na$_3$Sb alloy phase by Na-ion insertion. The difference between the first and following cathodic scans is mainly ascribed to the formation of SEI layer and the rearrangement of the structure.[130] In all of the anodic scans, a strong peak at 0.94 V is clearly seen, deriving from the phase transformation from Na$_3$Sb to Sb.[122]

Figure 5-6b depicts the charge-discharge capacity and Coulombic efficiency versus cycle number plots at a current density of 0.5 A g^{-1}, providing a direct evidence of the excellent Na storage performance. The voltage profiles with different flat plateaus indicate the redox reactions associated with Na alloying and dealloying in the discharge and charge curves, respectively, which owns typical features of Sb anodes[36] and are in good agreement with CVs results in Figure 5-6a. The first charge cycle shows a capacity of 590 mAh g^{-1} and hence, an irreversible capacity loss of 35%. However, the following discharge and charge cycles almost maintain or even exceed the reversible capacity from the first cycle. The voltage profiles of both charge and discharge have excellent reproducibility from the 1st to 100th cycles, suggesting the stable structure of fern leaf-like Sb and high reversibility during cycling.
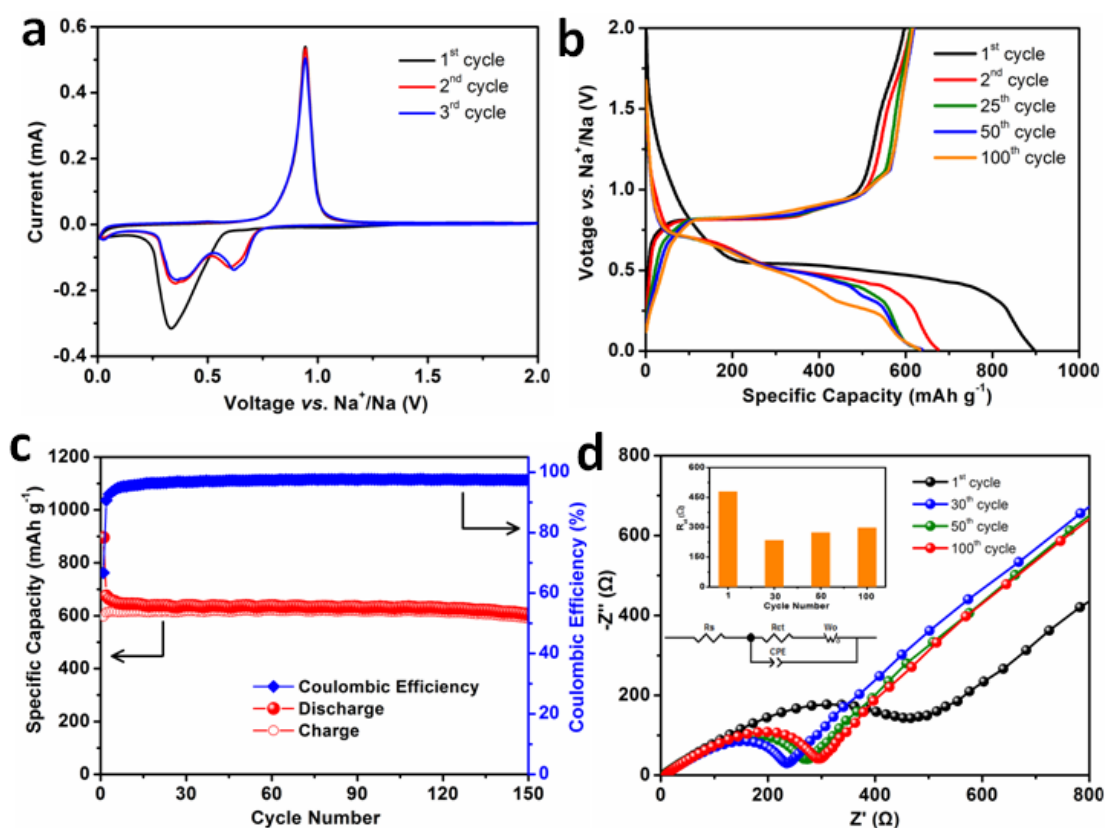
Figure 5-6 Electrochemical performance of the fern leaf-like Sb anode. (a) CV curves at a sweep rate of 0.5 mV s^{-1} between 0.01 to 2.0 V (*vs.* Na$^+$/Na). (b) Galvanostatic charge/discharge voltage profiles in different cycles at a current density of 0.5 A g^{-1}. (c) Cycling performance at 0.5 A g^{-1}. (d) Nyquist plots at charge state (2.0 V) from 1 MHz to 10 mHz.

Figure 5-6c presents the cycling performance of fern leaf-like Sb anode cycled at a current density of 0.5 A g^{-1}. The Sb anode exhibits an excellent cycling stability, where the reversible capacity is 589 mAh g^{-1} after 150 cycles, which is 98.5% of the initial reversible capacity. Except for the initial several cycles, the Coulombic Efficiency (CE) is about 97%, indicating facile ion and electron transport in this fern leaf-like Sb anode.[122, 221] To highlight the excellent cyclability of fern leaf-like Sb, these results were compared with results obtained in previously published Sb-based anodes, as shown in Table 5-1. It is clearly seen that both of the capacity and cycle life of fern leaf-like Sb are among the best values for reported Sb-based SIBs anodes.

Table 5-1 Cycling performance comparison of the as-prepared fern leaf-like Sb with some previously reported Sb-based anodes.

Materials	Current density (A g^{-1})	Reversible Capacity (mAh g^{-1})		Capacity retention
		2nd cycle	150th cycle	
Bi$_{0.36}$Sb$_{0.64}$-C[141]	0.2	~494	~320	~64.8%
Sb/C fibers[222]	0.1	~422	~380	~90%
rGO/nano Sb composite[41]	0.328	~590	~528	~89.5%
Sb/MWCNT nanocomposite[43]	0.2	~502	~382 (120th)	~76.1%
Porous Sb/Cu$_2$Sb[49]	0.066	~616	~485 (120th)	~78.7%
Bulk Sb[122]	0.33	~540	~570	~105.6%
Sb@C coaxial nanotubes[124]	0.1	~500	~410	~82%
Nanoporous Sb[125]	0.1	~630	~600	~95.2%
Sb-NiSb-Ni heterostructures[223]	0.066	~500	~450	~90%
Rod-like Sb-C composite[144]	0.05	~560	~450 (110th)	~80.4%
Sb porous hollow microspheres[142]	0.66	~575	~502	~87.4%
Sb/graphene[41]	0.328	~600	~530	~88.3%
Sb nanocrystals[40]	0.66	~600	~580 (100th)	~96.7%
Fern leaf-like Sb	0.5	~612	~589	~96.2%

To demonstrate the electrode kinetics of the fern leaf-like Sb during Na-ion sodiation/desodiation, the electrochemical impedance spectroscopy (EIS) at different cycles were tested at charge state (2.0 V) from 1 MHz to 10 mHz (Figure 5-6d). The Nyquist plots illustrate a depressed semicircle from high to medium frequency followed by a straight sloping line at the low-frequency end. The compressed semicircle refers to the charge transfer resistance (R_{ct}) for the electrode, and the inclined line describes the Na ion diffusion in the electrode electrolyte interface.[224-226] The correspondence between frequency-dependent impedance and equivalent circuit elements in this work can be logically distinguished after fitting to the equivalent circuit (the inset of Figure 5-6d). The resistor R_s and R_{ct} corresponds to the electrolyte resistance and charge transfer resistance, respectively.[224-226] The constant phase element CPE and the Warburg element W_o represent double-layer capacitance and the ion diffusion in the host material, respectively. The fitting values for charge transfer resistances (R_{ct}) are illustrated in the inset of Figure 5-6d. The large charge transfer resistance (480 Ω) in the high frequency region of the first cycle may be ascribed to the influence of SEI layer. With the increasing cycling numbers, it is evident that the charge transfer resistances (234 Ω for 30th, 273 Ω for 50th, and 297 Ω for 100th) keep relatively stable only with minimal increase (inset of Figure 5-6d), suggesting well-maintained electrical contact and relatively stable SEI layer.[227] These results further

confirm that the ion diffusion pathways and electron conduction in the electrode were well maintained and the stable electrode structure well relieved the large volume changes during charge/discharge cycles.[228]
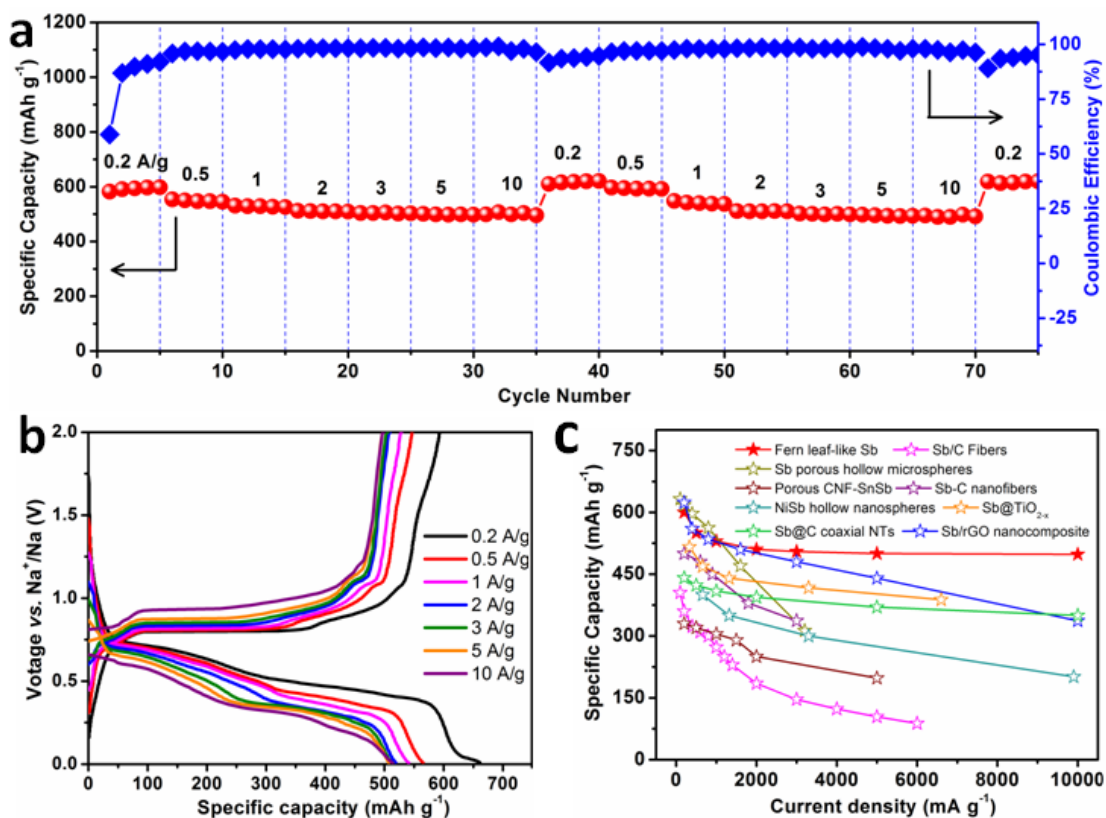
Figure 5-7 Electrochemical performance of the fern leaf-like Sb anode. (a) Rate capability and (b) charge/discharge voltage profiles at various current densities from 0.2 to 10 A g^{-1}. (c) Ragone plots of fern leaf-like Sb anode and other Sb-based SIBs anodes from literature (Sb/C fibers,[222] Sb@TiO$_{2-x}$,[44] porous CNF-SnSb,[229] Sb-C nanofibers,[132] NiSb hollow nanospheres,[46] Sb/rGO nanocomposites,[41] Sb@C coaxial NTs,[124] Sb porous hollow microspheres[142]).

The rate capability of the fern leaf-like Sb was also studied, which was tested at various current densities from 0.2 to 10 A g^{-1}, as revealed in Figure 5-7a. The Sb anode delivers reversible capacities of 600, 550, 530, 510, 505, 500 and 498 mAh g^{-1} at the current densities of 0.2, 0.5, 1.0, 2.0, 3.0, 5.0 and 10 A g^{-1}, respectively. At the rate of 10 A g^{-1}, the charging time is only 3 minutes. Figure 5-7b shows the corresponding voltage profiles of the Sb anode at various current densities. Despite the increasing current densities from 0.2 to 10 A g^{-1}, both charge and discharge voltage profiles still display quite similar shapes with minimal increase of the voltage offset. A second round of rate testing was taken to

further demonstrate the excellent rate capability of the sample. The capacities are rather stable at each rate, regardless the rate cycling history. When the rate was returned to 0.2 A g^{-1}, the reversible capacity fully recovered to 610 mAh g^{-1}. The excellent rate performance indicates that the fern leaf-like Sb has good structure tolerance for repeated alloying/dealloying processes and can endure large rate changes while simultaneously keeping high energy densities. To the best of our knowledge, the presented rate capability and specific capacities are among the best results of the reported Sb-based anodes (Figure 5-7c).

5.1.4 Reasons for excellent electrochemical performance

The benefits of fabricating fern leaf-like Sb structure, directly grown on a Ti current collector, as the anode material in Na-ion batteries can be understood from the below aspects. First, the hierarchical Sb structure inhibits the self-aggregation of Sb nanoparticles and ensures the surface remain uncovered to keep the effective and large contact areas. Therefore, the merits of Sb nanoparticles can be fully achieved, leading to short pathways both for Na ions and electrons. Second, the microsized structures are considered to contribute to the enough void space among the branches, which can mitigate the volume change upon cycling and simultaneously offer more active sites for Na ions. Third, metallic Sb with excellent electrical conductivity reacts with Na to form Na_xSb alloy which is also a good conductor. Therefore, the fern leaf-like Sb can be used as the additive-free anode without any addition of other conductive materials. Sb leaves closely contact with each other, which is conducive to transporting electrons from the substrate to Sb leaves. Additionally, Sb leaves build a powerful conductive network, promoting the efficient functioning of these leaves. Furthermore, the Sb anode reveals the good structural stability, which still retained the fern leaf-like morphology even after 100 cycles at a high rate of 0.5 A g^{-1} (Figure 5-8). All these beneficial factors of fern leaf-like Sb on the Ti current collector aid in enhancement of the capacity of the anode and provide excellent electrochemical performance.
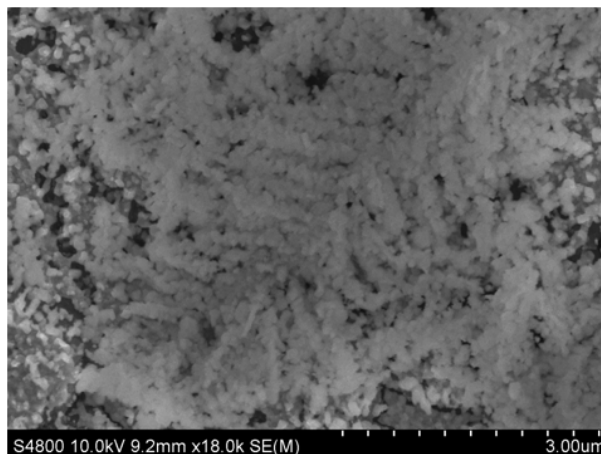
Figure 5-8 SEM image of fern leaf-like Sb after 100 cycles at 0.5 A g^{-1}.

5.1.5 Summary

Hierarchical Sb was firstly synthesized by using one-step electrodeposition method, which shows the morphology of fern leaf. As the additive-free anode for Na-ion storage, the obtained fern leaf-like Sb shows long lifespan and fast charge/discharge rates. The excellent electrochemical performance can be ascribed to morphological and structural features of the fern leaf-like Sb. The fern leaf-like Sb composed of self-assembled nanoparticles not only relieves the volume expansion well, but also facilitates the transport of Na ions and electrons. The synthesis method used in this work for hierarchical Sb structures is cost-effective, simple, high efficiency, and easily scaled up to large areas. The structural design and synthetic method reported in this work may provide an effective way to stabilize electrochemical performance of Na-storable alloy materials and therefore provide a new prospect for creation of cycle-stable alloy anodes for high capacity Na-ion batteries.

5.2 Large-scale highly ordered Sb nanorod array anode

The vertically aligned 1D nanostructure array is considered to be an efficient electrode configuration to enhance the electrochemical performance of batteries.[166, 188, 203, 230] However, for the majority of reported arrays, some defects are shown on their electrode structure design, which seriously weakens the electrochemical performance. More or less agglomerated morphology is demonstrated instead of perfect vertical alignment in these reported arrays. Due to the existed stress among these nanostructures upon cycling, the joint parts tend to break, thereby leading to the severe pulverization and collapse of the electrode. Additionally, limited interval spacing in attached arrays decreases the ion

transport rate to the inner regions of the electrode, which is not beneficial to high rate property. Although using nanostructure arrays as electrodes omits the complex processes of mixing conductive carbons and organic binder, the conductivity of most of arrays is not good enough to support the electrode to finish fast Li/Na ions insertion/extraction and still keep high capacity and long lifespan.[168, 204, 231, 232]

Nanoimprinted AAO templating technique can be used to fabricate 1D nanostructure arrays with perfect long-range regularity, fine size controllability, and very large area (up to cm^2).[175, 196, 233] In particular, using this technique, it is also achievable to prepare perfectly vertically aligned 1D nanostructure arrays with large interval spacing (*e.g.* about 200 and 400 nm interval spacing by using different template cell size of 400 and 800 nm). However, so far, very few reports are proposed on the end of SIBs using such 1D nanostructure arrays electrode. We believe that if using these 1D nanostructure arrays with large-scale high ordering, well vertical alignment, and large interval spacing as SIBs electrodes, the electrochemical performance shall introduce a great enhancement.

Here, the large-scale highly ordered Sb nanorod arrays with uniform large interval spacing is firstly reported as an excellent SIBs anode, which is fabricated by the nanoimprinted AAO templating technique and an electrochemical deposition process. In such a unique architecture, some critical features are helpful to improve the Na-storage property. First, nano-sized Sb could shorten Na ions diffusion pathway. Second, the perfect vertical alignment and attendant large interval spacing provide direct channels for electrolyte to permeate into the interior portions of arrays, and then Na ions can fully contact Sb nanorods without dead angels, finally revealing high Na ions accessibility. Meanwhile, the large interspace in arrays can also accommodate the volume expansion and contraction of Sb. Third, Sb nanorods themselves as electric conductors directly connecting with the conductive Au/Ni substrate, offering fast and accessible electrons transport, which is greatly conducive to the enhanced rate capability. Finally, the good adhesion between arrays and conductive substrate can ensure the robust arrays integrity to relieve volume changes upon cycling.

In return to its pathbreaking electrode design, the as-prepared Sb nanorod arrays, as additive-free anodes for SIBs, show a high capacity of 620 mAh g^{-1} at the 100th cycle with a retention of 84% up to 250 cycles, and superior rate capability for delivering reversible capacities of 579.7 and 557.7 mAh g^{-1} at 10 and 20 A g^{-1}, respectively. We believe that these excellent electrochemical performances shall arouse high attention to develop more efficient electrode structures for energy storage system.

5.2.1 Structural and morphological characterizations

The morphologies of nanoimprinted AAO template and Sb nanorod arrays are firstly investigated by SEM. As displayed in Figure 5-9a and b, the AAO template has hexagonal arranged pores that are perfectly uniform in large-area, in which the pore diameter is about 210 nm. It is worth noting that both the size and depth of pores can be accurately adjusted to obtain the desired size depending on the time of pore-widening and anodization, respectively. Figure 5-9c-f illustrates the top and tilted views of the as-prepared Sb nanorod arrays which keep the highly ordered and vertically well-aligned growth in large-scale. As is clearly observed from the insets in Figure 5-9d and f, Sb nanorods possess the uniform diameter of about 210 nm, and the interval distance among nanorods is as large as 190 nm, as defined by the pore size of as-prepared AAO template.

Figure 5-9g reveals an optical image of Sb nanorod arrays directly grown on Au/Ni substrate. It clearly exhibits that Sb nanorod arrays with Au/Ni substrate can be severely rolled without visible signs of degradation, which proves the good adhesion and mechanical robustness of the arrays. This feature might imply a possible application of our electrodes for in flexible electronics. As shown in Figure 5-9g inset, highly ordered Sb nanorod arrays are obtained over a large area (around cm^2-sized range). Larger areas can also be easily achievable by using the larger-sized Ni imprinting stamp combined well-established roll to roll process.

More structural information of Sb nanorod arrays are studied by TEM. Figure 5-9h clearly shows the diameter and length of Sb nanorod is about 210 nm and 1.5 μm, respectively. HRTEM image in Figure 5-9i shows the lattice fringes with the distance of 3.09 Å, corresponding to the (012) planes of rhombohedral Sb, further confirming the high crystallinity of the sample. The SAED pattern in Figure 5-9i inset proves that the Sb nanorods are polycrystalline.
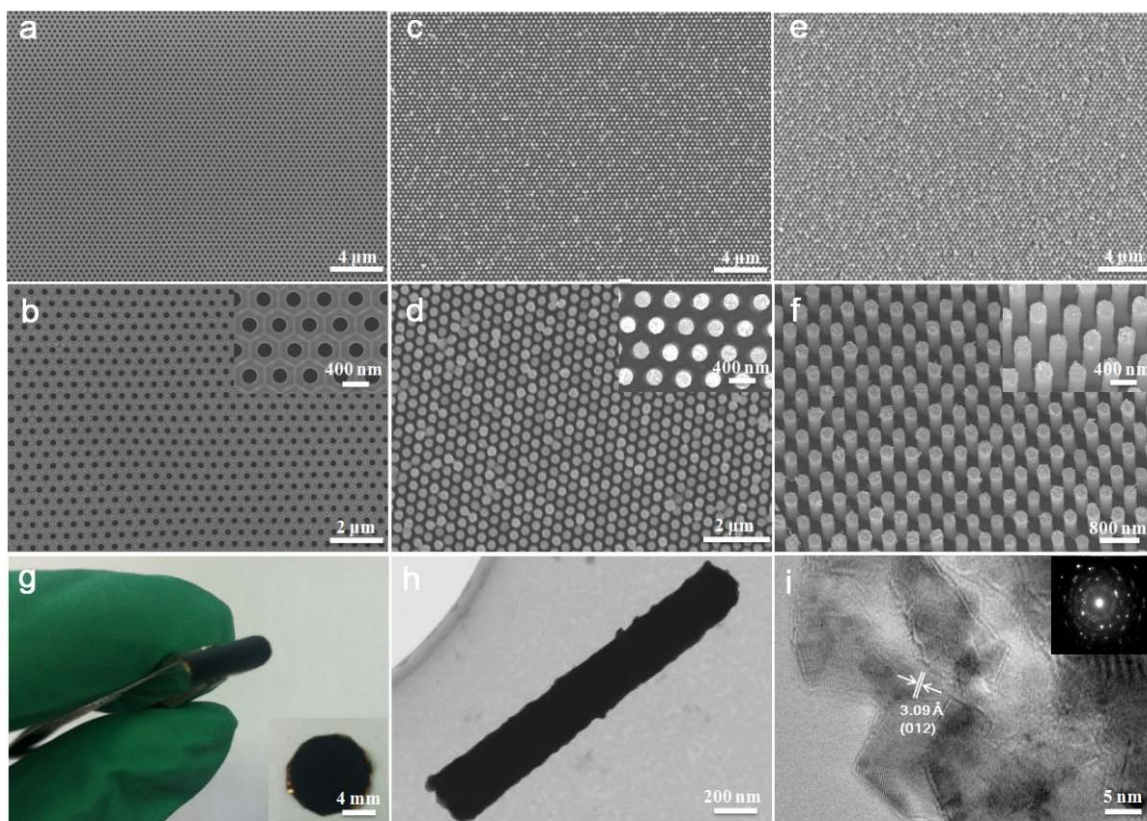
Figure 5-9 SEM images of nanoimprinted AAO template (a, b), top view (c, d) and tilted view (e, f) of Sb nanorod arrays. (g) Optical image of Sb nanorod arrays on Au/Ni substrate. (h) TEM image of a single Sb nanorod. (i) HRTEM image of Sb nanorods and SAED pattern (inset).

The crystalline structure of the as-prepared Sb nanorod arrays is revealed by XRD, as presented in Figure 5-10. Except for the reflections of the substrate (Au and Ni), all the other diffraction peaks can be assigned to the rhombohedral Sb phase (JCPDS No. 35-0732) without any impurity, indicating the pure phase of Sb generated.
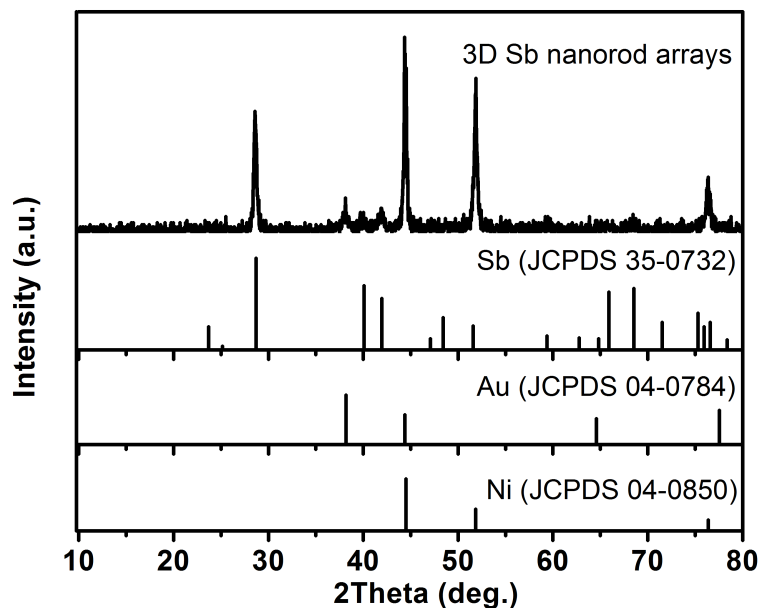
Figure 5-10 XRD pattern of Sb nanorod arrays on Au/Ni substrate.

5.2.2 Na-ion half-cell performance

Successful fabrication of such highly ordered and vertically well-aligned Sb nanorod arrays with large interval spacing may provide high ion accessibility, direct electron and ion transport, and robust electrode integrity. Therefore, a promising electrochemical performance is highly desired.

5.2.2.1 Electrochemical reaction mechanism

The sodiation/desodiation behavior of the prepared Sb nanorod arrays was evaluated in a voltage range of 0.01-2.0 V (*vs.* Na^+/Na). Figure 5-11a shows representative CV curves of the initial ten cycles measured at a scan rate of 0.5 mV s^{-1} to identify the electrochemical reactions involved during cycling. In accordance with previous reports,[36, 39, 222] the first sodiation scan curve is distinctively different with that of the following ones, suggesting that an activation process may occur during the first sodiation process. In the first sodiation scan, one sharp current peak at 0.323 V, together with two obscure current peaks at 0.461 and 0.283 V are observed. However, in the second sodiation scan, there are four distinct current peaks at 0.614, 0.355, 0.309, and 0.130 V. The peak at 0.130 V may be induced by the incomplete sodiation of the former steps in the activation process,[122] and then disappears in the following ones. Other three sodiation peaks are continuously shown, whereas shifting to higher potentials and remaining stable in their shapes and intensities in the following ones, indicating the occurrence of stable sodiation reactions.[229] In the first

54

desodiation scan, there are one broad peak at 0.835 V and one sharp peak at 0.977 V, which retain showing in the subsequent scans, while slightly shifting to lower potentials. As a result, the potential difference between sodiation and desodiation process is lessening, reflecting smaller polarization.

Galvanostatic charge/discharge curves of Sb arrays electrode at a current density of 0.5 A g^{-1} are illustrated in Figure 5-11b, which exhibit typical characteristics of Sb electrodes.[132, 142, 146] In the first discharge curve, it shows the presence of three sodiation plateaus, which are a short slope at 0.590 V, a long plateau at 0.502 V, and a much shorter one at 0.391 V. These three plateaus constantly show in the following curves, corresponding to the sequence from amorphous Sb to amorphous Na_3Sb next to Na_3Sb(hex) / Na_3Sb(cub) then to Na_3Sb(hex).[122] In the first charge curve and the subsequent ones, two pronounced disodiation plateaus are constantly shown, which are a long plateau at 0.800 V and another short one at 0.898 V, corresponding to the process of Na_3Sb(hex) $\rightarrow$ amorphous Sb transition and partial crystallization of Sb, respectively. The plateaus seen in the charge and discharge curves are consistent with the peaks seen in the CV curves. Furthermore, it is worthwhile to be noted that the voltage profiles of both sodiation and desodiation are perfectly reproducible from cycles 1 to 100, indicating the stable structure of Sb nanorod arrays and excellent electrochemical reversibility during cycling.
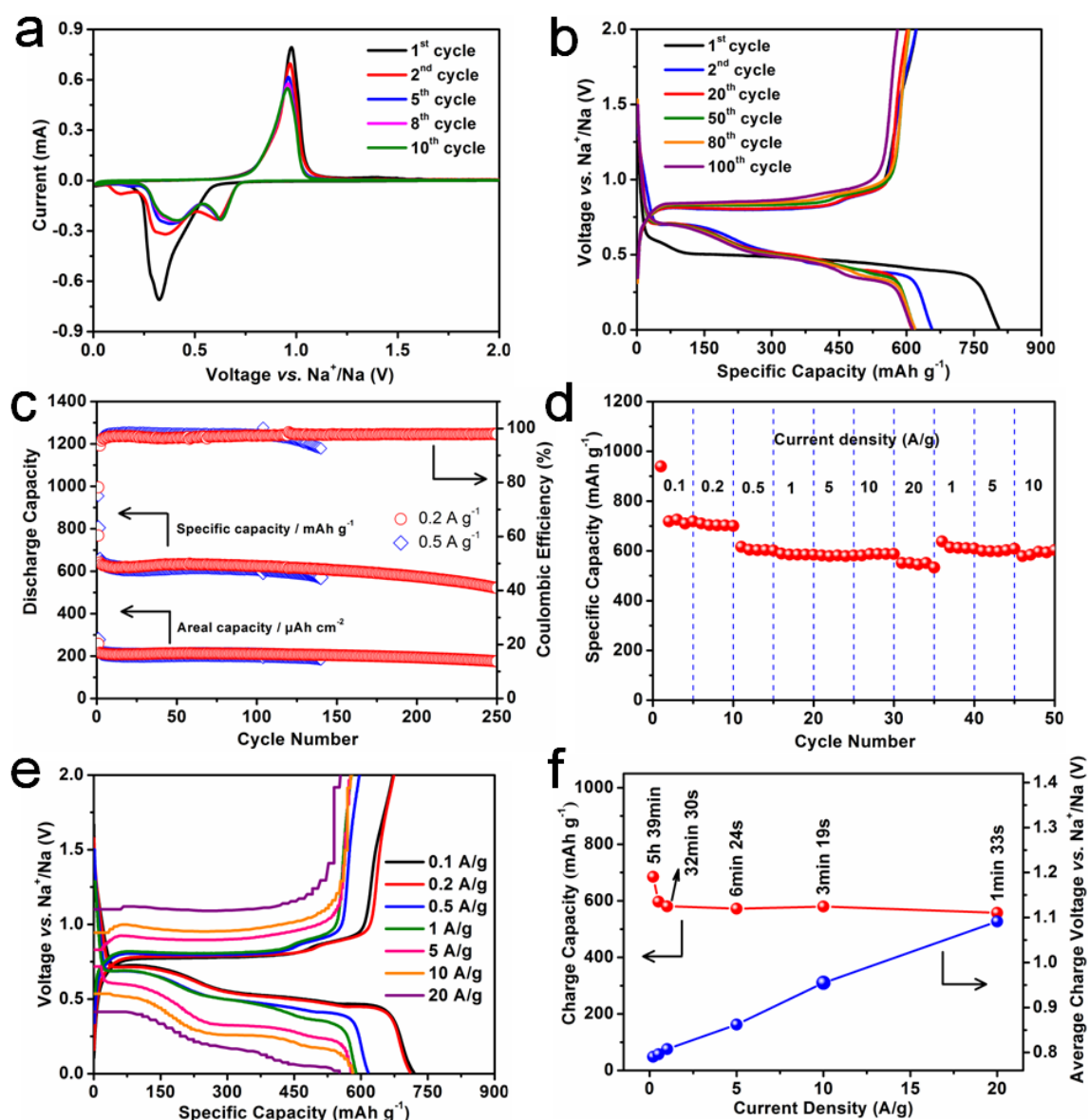
Figure 5-11 Electrochemical performance of Sb nanorod arrays anode. (a) Cyclic voltammetry at a scan rate of 0.5 mV s^{-1} between 0.01 to 2.0 V (*vs.* Na$^+$/Na). (b) Galvanostatic charge/discharge voltage profiles in different cycles at a current density of 0.5 A g^{-1}. (c) Cycling performance at current densities of 0.2 (80 μA cm^{-2}) and 0.5 A g^{-1} (32 μA cm^{-2}). (d) Rate performance and (e) corresponding charge/discharge voltage profiles at various current densities from 0.1 to 20 A g^{-1}. (f) Respective charge capacity and average charge working potential at various current densities.

5.2.2.2 Cycling performance

Figure 5-11c shows the cycling stability of Sb nanorod array anode. At a current density of 0.2 A g^{-1}, it delivered a high capacity of 620 mAh g^{-1} at the 100th cycle, and 521 mAh g^{-1} at the 250th cycle with a capacity retention of 84%. The excellent cyclability is comparable to that of recent research on Sb-based anode (Table 5-2). The capacity decay of Sb nanorod arrays was attributed to inevitable increasing thick SEI film and huge volume changes of Sb anode upon cycling, as shown in Figure 5-12. The decay is also accordingly reflected on charge/discharge profiles in different cycles (Figure 5-13). With the increasing cycles, the plateaus of charge and discharge profiles gradaully go up and go down, respectively, and the voltage differences between charge and discharge curves are growing, suggesting the occurrence of capacity decay and polarization.

Table 5-2 Cycling performance comparison of the as-prepared Sb nanorod arrays with previously reported Sb-based anodes.

Materials	Current density/A g^{-1}	Cycles	Retention	Last cycle capacity /mAh g^{-1}
Monodisperse Sb Nanocrystals[39]	0.66	100	> 90%	~580
SnSb-porous carbon nanofibers[229]	0.1	205	> 90%	~345
Bulk Sb[122]	0.33	160	> 90%	~576
rGO/Sb$_2$S$_3$[234]	0.05	50	~90%	~620
Sn-Ge-Sb thin film alloys[235]	0.425	50	~73%	~662
Sb-C nanofibers[132]	0.2	400	> 90%	~450
Sb/C fibers[222]	0.1	300	~83%	~350
S-Sb NRs (this work)	0.5	140	> 90%	~571
	0.2	100	> 90%	~620
		250	~84%	~521

Although the cycle life was prolonged at a relatively low current density, there should still have some space for further improvement. Therefore, we analyzed the fading mechanism by investigating the structure change during cycling and provided the directions for further improvement. Figure 5-12 shows the SEM images of Sb nanorod arrays anode after various cycles at a current density of 0.2 A g^{-1}. The highly ordered and vertically well-aligned feature with clear interval spacing still was maintained after 100 cycles (Figure 5-11c and Figure 5-13). Meanwhile, a thin layer of SEI film around Sb nanorod can be

observed. The SEI film gradually became thicker upon cycling, as shown in Figure 5-12c and d, which is attributed to continuous formation of new SEI film deriving from large volume changes of Sb (390%) in repeated Na alloying/dealloying processes. After 150 cycles, the SEI film (as indicated by red circle) has filled the part of interval spacings, whereas there still had enough spacing for electrolyte infiltration (as shown by yellow arrow), which is beneficial for cycling stability. After 200 cycles (Figure 5-12e and f), most of interval spacing had been filled by the thicker SEI film, leading to slow ions diffusion, then followed by the slight decay of capacity (as shown in Figure 5-11c). Except the adverse effect of SEI film, as far as we know, the large volume change of Sb is another factor for the capacity decay, which is also considered to be the major reason for capacity decay of bare alloy-based materials. Before 200 cycles, due to the chemical and mechanical robustness of our arrays electrode, the Sb nanorod maintained its integrity, resulting in stable cycling performance. However, with longer cycling, this huge volume change caused the pulverization, and then the surface of nanorod became cracked, as indicated by the blue circles in Figure 5-12g and h. We scratched Sb nanorods off the current collector in order to observe the single nanorod, as shown in Figure 5-12i. The magnified SEM image displays the clear cracks on the surface of Sb nanorod compared to the pristine Sb nanorod before cycling (Figure 5-12j) which shows the complete nanorod structure without any cracks. The increasing volume change damaged the electrode integrity, resulting in a loss of contact between active material and current collector. As a consequence, upon cycling, more capacity fading was observed. The decay can also be accordingly reflected on charge/discharge profiles at various cycles (Figure 5-13). At high rates, the phenomenon of volume changes would be more obvious, thus accelerating the capacity decay. Therefore, Sb nanorod arrays anode showed a shorter cycle life at the larger current density of 0.5 A g^{-1} than at 0.2 A g^{-1} (Figure 5-11c).
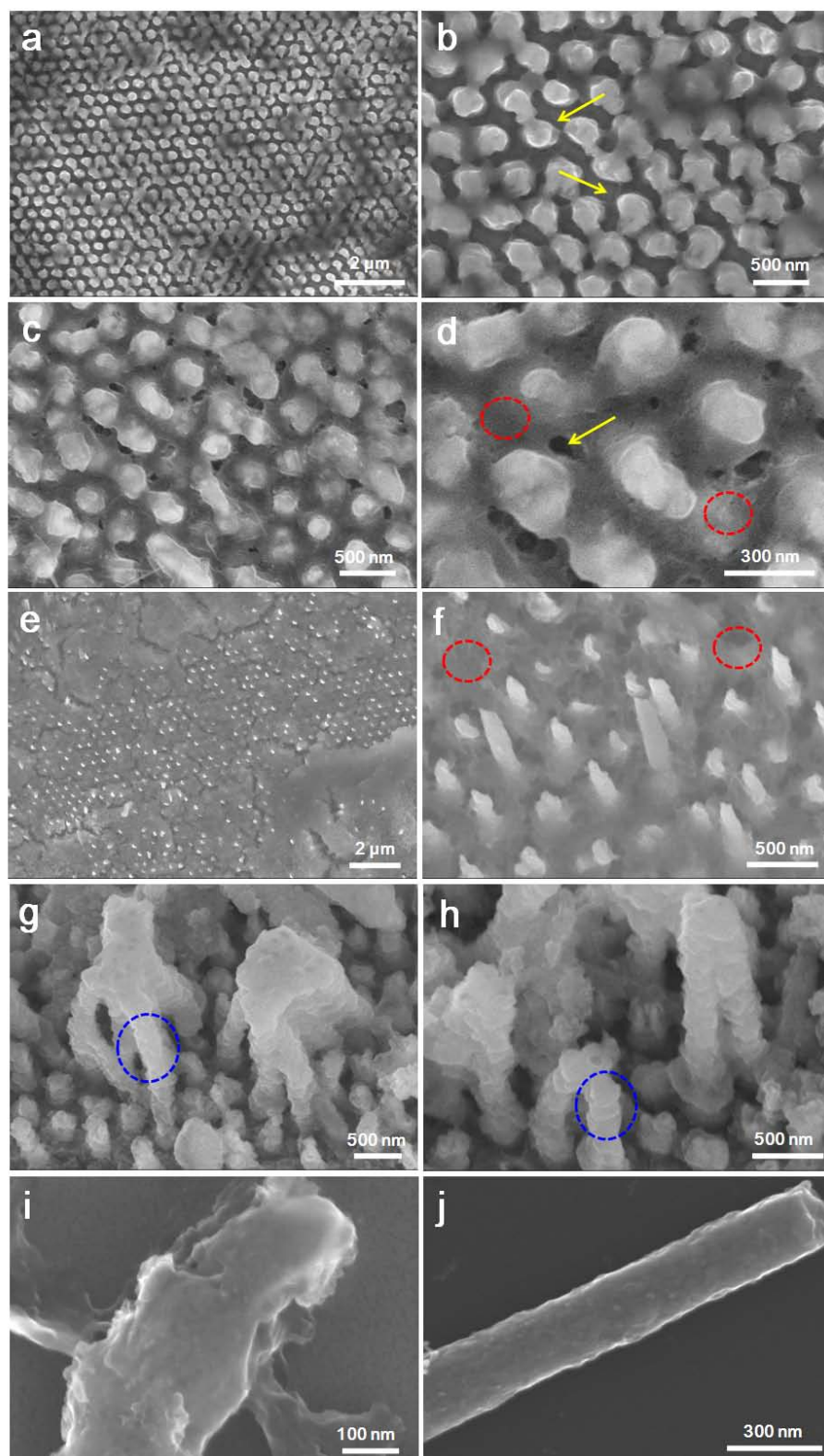
Figure 5-12 SEM images of Sb nanorod arrays after different charge/discharge cycles. (a) and (b) after the 100th cycle. (c) and (d) after the 150th cycle. (e) and (f) after the 200th cycle. (g-i) after the 250th cycle. (j) before cycling.

It is worthwhile noting that the cycling performance of this anode was obtained without any sophisticated chemical modification of Sb material. It is reported that the protective coating by carbon or other materials can effectively tolerate the massive volume changes and alleviate the stress strain during the Na alloying/dealloying reaction.[34, 41, 124] Therefore, we deduce that such strategy could be the direction of further improvement on cycling performace. The areal capacity of Sb nanorod arrays is also calculated, which is about 215 μAh cm^{-2} at a current density of 80 μA cm^{-2}. The Coulombic Efficiency for the first cycle is around 78.2%, while it stabilizes at around 97.8% for the following cycles, indicating facile and efficient ions and electrons transport in this electrode.[221, 236, 237] When cycled at a large current density of 0.5 A g^{-1}, Sb nanorod arrays showed almost the same capacity with that at 0.2 A g^{-1}, but shorter cycle life due to more serious morphology changes.
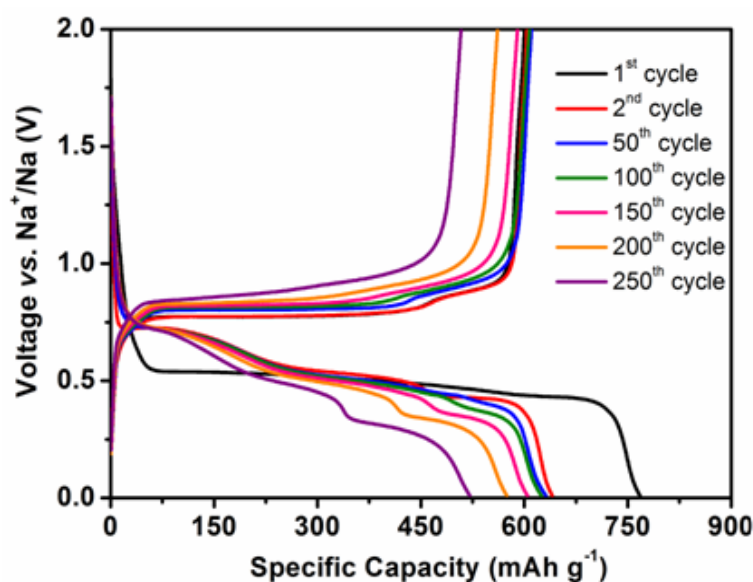
Figure 5-13 Galvanostatic charge/discharge voltage profiles of Sb nanorod arrays at a current density of 0.2 A g^{-1}.

5.2.2.3 Rate performance

Except for the high capacity and cyclability, Sb nanorod arrays anode also presents remarkably high rate capability. The rate performance was investigated using various current densities, which are increased stepwise from 0.1 to 20 A g^{-1}, as shown in Figure 5-11d. For each step, 5 cycles were tested in order to evaluate the rate performance. It is striking to note that Sb nanorod arrays electrode still can be reversibly cycled at super high current densities of 10 and 20 A g^{-1} and deliver large capacities of 579.7 and 557.7 mAh g^{-1}, respectively, indicating the fast transfer of Na ions and electrons through Sb nanorod

arrays. When the current densities are reset to 1, 5, and 10 A g^{-1}, the capacities fully recovered and are even slightly higher than those of the first set at the same current densities, proving that the unique electrode structure can preserve the integrity of the electrode and accommodate huge change of current density, which is highly crucial for high power applications of rechargeable batteries. This rate performance is among the best values of the previously reported Sb-based anodes in SIBs, as shown in Table 5-3.
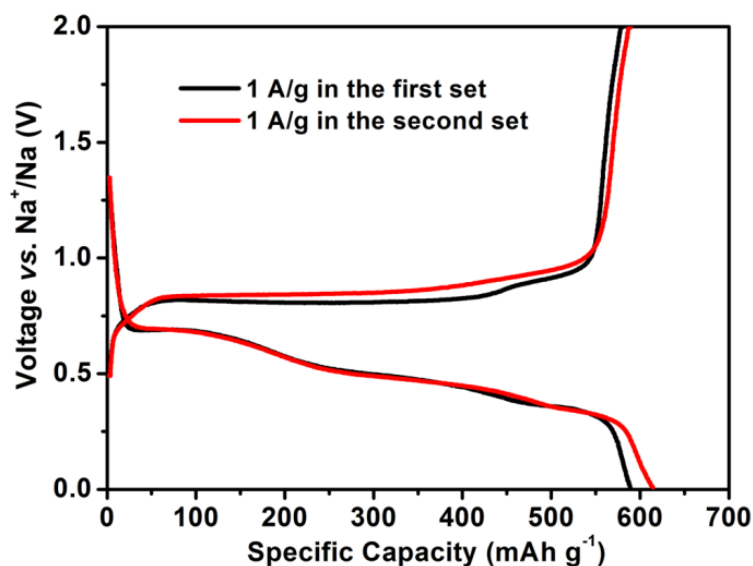
Figure 5-14 Galvanostatic charge/discharge voltage profiles of Sb nanorod arrays at the current density of 1 A g^{-1} in different rate sets.

Figure 5-11e depicts the corresponding voltage profiles of the electrode at various current densities. As current density increasing from 0.1 to 20 A g^{-1}, the charge/discharge voltage profiles have similar shapes, with minimal increase of the voltage offset, even at ultra-high current density of 20 A g^{-1}, suggesting facile electron transport and small mechanical energy loss of the electrode. Moreover, when the current density is reduced back to 1 A g^{-1} (Figure 5-14), the voltage profiles recovered and are perfectly reproducible in comparison with that of the first set at the same current density (1.0 A g^{-1}), reflecting the stable structure of Sb nanorod arrays to strongly tolerate the repeated and rapid Na alloying/delloying reactions. Charge working potentials of the electrode at different current densities are shown in Figure 5-11f. The potentials only display a small increase of 0.027 V when the current is raised from 0.1 to 1 A g^{-1}, and an increase of 200 times of the current brings an increase of the potential of only 0.311 V when the current is raised to 20 A g^{-1}, indicating the excellent structure stability of Sb nanorod arrays and fast electron transport. In addition, the charging time are 6 min 24 s, 3 min 19 s, and 1 min 33 s at the current

densities of 5, 10, and 20 A g^{-1}, with high charge capacities of 572.4, 579.7, and 557.7 mAh g^{-1}, respectively. The electrodes can be charged and discharged at such high rates with such large capacities in such short time, which are highly desired for high power and energy devices.

Table 5-3 Electrochemical performance comparison of the as-prepared Sb nanorod arrays with previously reported Sb-based anodes.

Materials	Current density, A g^{-1}	Cycling Capacity, mAh g^{-1}			Rate Capability, mAh g^{-1} (current density, A g^{-1})	
		2nd	50th	100th		
Nanocomposite Sb/C[34]	0.1	610	570	575	489 (1)	309 (2)
SnSb/C nanocomposite[36]	0.1	~540	435	/	433 (0.2)	274 (1)
Sb/C fibers[222]	0.1	~425	~420	400	300 (1)	104 (6)
Monodisperse Sb Nanocrystals[39]	0.66	~590	~560	~580	~550 (5.28)	~520 (13.2)
Bulk Sb[122]	0.33	~540	~560	~570	506 (1.32)	491 (2.64)
Sb/MWCNT nanocomposite[43]	0.2	~510	~450	~400	350 (1)	225 (2)
Sb porous hollow microspheres[142]	0.66	574.9	~520	502.3	470.3 (1.6)	312.9 (3.2)
SnSb-porous carbon nanofibers[229]	0.1	349	350	350	198 (5)	113 (10)
Sb-C nanofibers[132]	0.2	~495	~500	~490	382 (1.8)	337 (3)
Porous Sb/Cu$_2$Sb anode[49]	0.066	~660	~550	~480	~470 (0.66)	~170 (3.3)
Rod-like Sb-C composite[144]	0.05	~650	~440	~431	~500 (0.05)	~259 (0.25)
Sn-Ge-Sb alloys[235]	0.085	833	662	/	~420 (4.25)	381 (8.5)
Sb nanorod arrays (this work)	0.5	655.7	618.4	612.6	579.7 (10)	557.7(20)

5.2.4 Analysis of structural features

The above electrochemical characterization demonstrates that highly ordered Sb nanorod arrays developed in this work have high reversible capacity, rate capability and cycling stability for Na-ion storage. The excellent electrochemcial properties are preliminarily attributed to its pathbreaking electrode design on the basis of the following factors. First, the nano-sized diameter of Sb nanorods can shorten Na ion diffusion pathway compared to the bulk Sb powders. Nanostructuring of the active materials can also moderate the effect of volume changes and enhance kinetics of the conversion and alloying reactions.[238-240] Second, Sb nanorod arrays themselves as electric conductors directly connect to the conductive Au/Ni substrate offering fast and accessible electron transport, giving rise to

superior rate capability. Third, Sb nanorod arrays show well vertical alignment and uniform large interval spacing (about 190 nm), which provide direct channels for electrolyte and ions to permeate into all the portions of arrays, and thus Na ions can fully contact Sb nanorods without any dead angels, improving Na ion accessibility. This point surpasses the traditional materials including powder-based materials and disordered network that charge carriers must move through the interstitial regions or spaces within materials to access the internal part. Owing to this feature as well as the large surface area of Sb nanorod arrays, large capacities at high rates are obtained. Moreover, the large interval spacing in arrays can prevent the pulverization by facile strain relaxation during cycling. The third point is extremely significant to ensure Sb nanorod arrays to show high capacities, long-term cycling stability, and excellent rate capability.

In order to better reveal the advantages of highly ordered arrays with large interval spacing, we conducted parallel comparative tests between vertically well-aligned Sb nanorod arrays (S-Sb NRs) and attached Sb nanorod arrays (A-Sb NRs) with very limited interval spacing for the permeation of electrolyte (relating to Na ion transport and strain release) on the electrochemical performance. These two arrays have the same length of 1.5 μm, and more detailed structure parameters of A-Sb NRs can be found in Table 5-4.

Table 5-4 Structure and electrochemical performance comparison of four different Sb nanorod arrays.
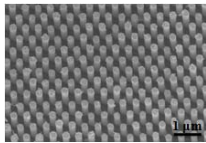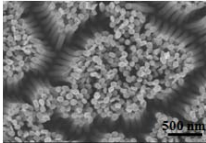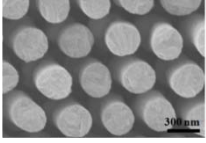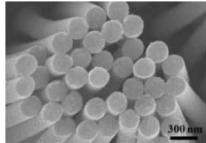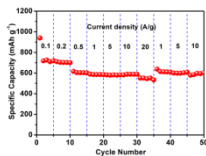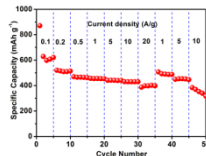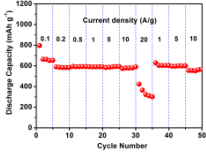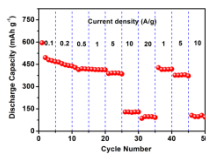
Name	S-Sb NRs	A-Sb NRs	S-2-Sb NRs	A-2-Sb NRs
Cell Size	400	110	400	400
Diameter/nm	210	70	300	210
Length/μm	1.5	1.5	1.5	6.0
Interval Spacing	190	Limited	100	Limited
Aspect Ratio (L *vs.* D)	7.14	21.43	5	28.57
Well-aligned	√	/	√	/
Attached	/	√	/	√
Morphology				
Electrochemical Performance				

Figure 5-15 demonstrates the different Na ion transport modes in these two arrays, noting that metal Sb is a good electric conductor and it can effectively transfer electrons between conductive substrate and nanorods without the help of conductive additive carbon. As shown in Figure 5-15a and b, due to the large interval spacing in vertical well-aligned arrays, Na ions can easily diffuse into the matrix in S-Sb NRs, resulting to superior Na ion accessibility, thus large capacities are highly expected, especially at high current densities. In contrast, SEM image (Figure 5-15c) of A-Sb NRs displays severe agglomerated nanorods and attendant very limited interval spacing in arrays. Therefore, the electrolyte is very difficult to directly penetrate into the bottom region of A-Sb NRs through the top of attached nanorods (Figure 5-15d). As a substitute, Na ions have to diffuse through interstitial regions within arrays, which would lead to incomplete active sites for Na^+, then showing decreased capacities of A-Sb NRs. On the other hand, the large interval spacing in S-Sb NRs can provide a facile strain relaxation during cycling, thereby preventing the pulverization. However, for A-Sb NRs, the joint parts tend to break since the stress existed among these entangled Sb nanorods, leading to poor transport of electrons and ions, thereby rapid capacity decay.[241, 242]
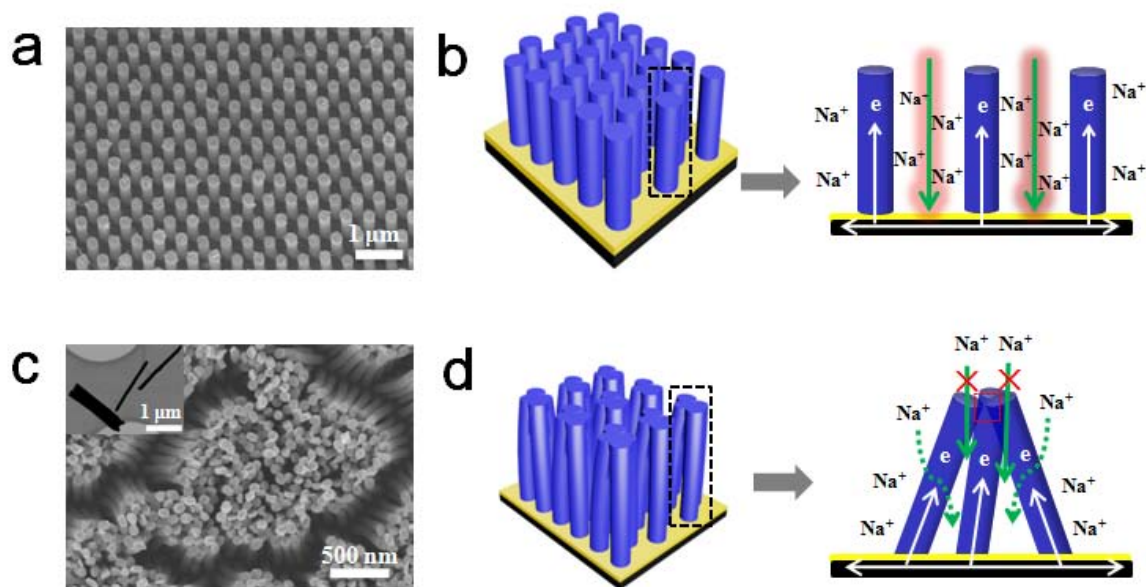
Figure 5-15 SEM images of (a) S-Sb NRs and (c) A-Sb NRs (Inset: TEM image of A-Sb NRs). Corresponding schematic illustration of transport mechanism of Na ions and electrons in (b) S-Sb NRs and (d) A-Sb NRs.

Based on the above analysis of different Na ion transport and strain release modes, we investigated the electrochemical performance of A-Sb NRs and S-Sb NRs under the same testing conditions. As shown in Figure 5-16a, the A-Sb NRs have the similar CV curves with S-Sb NRs (Figure 5-11a), indicating the identical sodiation/desodiation mechanism. However, the capacities and cycling stability are far less than those of S-Sb NRs. In Figure 5-16b, A-Sb NRs show a first discharge capacity of 529.5 mAh g^{-1} and CE of 79.5% at a current density of 1 A g^{-1}. In the following 50 cycles, A-Sb NRs keep stable discharge capacity of around 475 mAh g^{-1}, however, the CE gradually decreases, implying the irreversible reactions occurred during this period. From the 50th cycle, A-Sb NRs undergo rapid capacity decay, delivering only 345.1 mAh g^{-1} in the 60th cycle. The galvanostatic charge/discharge voltage profiles of A-Sb NRs (Figure 5-17a) further reveal this decay phenomenon from another point of view. In the 50th cycle, the discharge plateau appears a big decrease from 0.37 V in 10th cycle to 0.17 V and the flat charge plateau at 0.87 is replaced by a big slope. In contrast, an excellent cycling stability of S-Sb NRs is observed at the same current density and the electrode still can retain a constant and even slightly ahead of capacity of 625.2 mAh g^{-1} over 60 cycles and high CE of around 98% (except the first cycle of 83%) (Figure 5-16c). Furthermore, the voltage profiles of S-Sb NRs (Figure 5-17b) present perfect reproducibility during 50 cycles. Notably, it is as expected that the capacity, CE, and cycling stability of S-Sb NRs are much better than those of A-Sb NRs, which is largely ascribed to more efficient ion transport, as well as more facile strain release in S-Sb NRs.

Nyquist plots of A-Sb NRs and S-Sb NRs are displayed in Figure 16d and e to investigate their resistance change with the increased cycles. From the first cycle to 50th cycle, A-Sb NRs show a gradually increased resistance (Figure 5-16d). However, for S-Sb NRs, the change of resistance is negligible (Figure 5-16e), further confirming relatively easier Na ion transport in S-Sb NRs, thereby reducing the irreversible capacity loss and enhancing cycling performance. For the rate performance of A-Sb NRs electrode (Figure 5-16f), it demonstrates the similar trend with S-Sb NRs in the first 45 cycles but with lower capacities. In addition, from the 46th cycle (a current density of 10 A g^{-1} in the second rate set), the capacities rapidly decrease. Under high current densities, the electrode needs to finish the charge and discharge processes in a very short time. Therefore, high ions accessibility, good electrical conductivity, and stable electrode structure are essential. A-Sb NRs electrode shows limited ions accessibility, and the attached structure of is not conducive to release strain induced by volume expansion, resulting in unstable electrode

structure. As a sum result, under the high current density of 10 A g^{-1} in the second rate set, A-Sb NRs electrode displays rapid capacity decay. The largely different electrochemical performance between A-Sb NRs and S-Sb NRs fully supports our assumption of the predominance of this highly ordered alignment with large interval spacing electrode design for Na-ion storage. To more comprehensively reveal the importance of highly ordered arrays with interval spacing, we also compared the electrochemical performance of another two kinds of arrays, as shown in Table 5-4 and Figure 5-18.
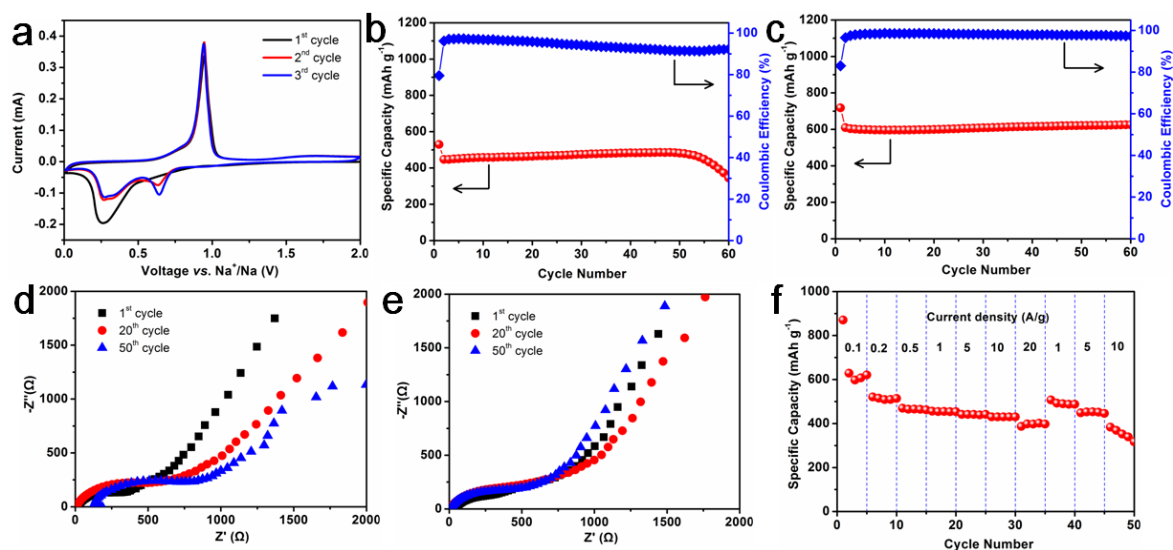
Figure 5-16 (a) Cyclic voltammetry of A-Sb NRs electrode at a scan rate of 0.5 mV s^{-1} between 0.01 to 2.0 V (*vs.* Na$^+$/Na). Cycling performance of (b) A-Sb NRs and (c) S-Sb NRs at a current density of 1 A g^{-1}. Nyquist plots of (d) A-Sb NRs and (e) S-Sb NRs at discharge state (0.01 V) from 1 MHz to 10 mHz. (f) Rate performance of A-Sb NRs electrode at various current densities from 0.1 to 20 A g^{-1}.

In the above, the comparison between S-Sb-NRs and A-Sb-NRs has shown the effect of the spacing between rods on the electrochemical performances. The difference of spacing was realized by using the templates with different cell size, *i.e.*, 400 nm for S-Sb-NRs and 110 nm for A-Sb-NRs. To further demonstrate the effect of spacing between rods, another reference sample (S-2-Sb-NRs) with the same cell size of 400 nm was fabricated. By changing the diameter of the rods from 190 to 300 nm, the spacing between rods has been changed from 210 to 100 nm. SEM images can be found in Figure 5-18a. The electrochemical performance of S-2-Sb NRs (Table 5-4) displays the large and stable capacities from the current density of 0.1 to 10 A g^{-1}, due to its highly ordered alignment. However, a capacity decay was observed at 20 A g^{-1}, supposed to that the interval spacing

of 100 nm is not enough to accommodate the huge volume changes of Sb nanorod arrays at such a large current density. It is worth noting that, the above-mentioned results also reflect the effect of the diameter since the two samples, S-Sb-NRs and S-2-Sb-NRs, possess identical structural parameters except for the diameter.
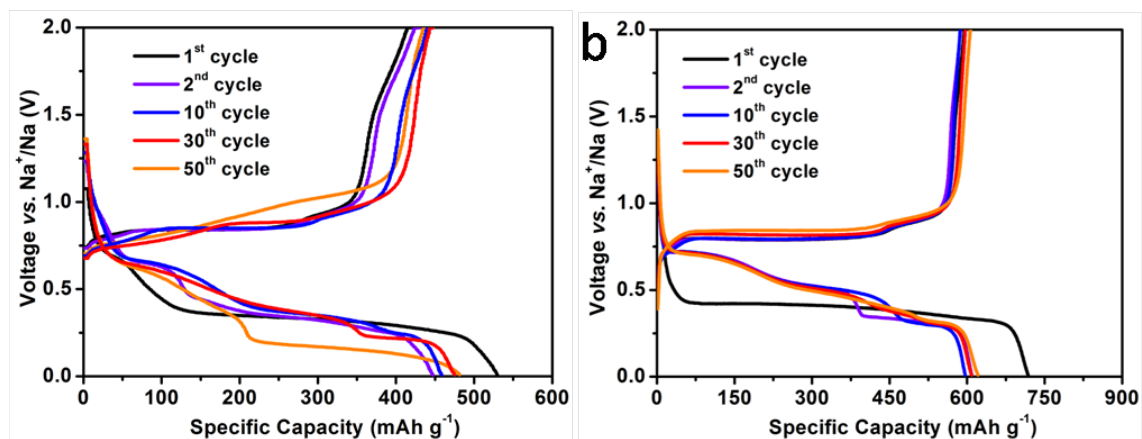
Figure 5-17 Galvanostatic charge/discharge voltage profiles of (a) A-Sb NRs electrode and (b) S-Sb NRs at a current density of 1 A g^{-1}.

To demonstrate the effect of aspect ratio (L *vs.* D), a reference sample (A-2-Sb-NRs) was fabricated. The sample has the same structural parameters with S-Sb-NRs except for the length which has been increased to 6.0 μm (Figure 5-18b), giving rise to an aspect ratio of 28.57 (*vs.* 7.14 for S-Sb-NRs). A-2-Sb NRs displayed lower capacity than S-Sb NRs, and serious capacity decay at the large current densities of 10 and 20 A g^{-1}. Because it is difficult for electrolyte transferring into the internal region of attached arrays, in particular at large rates, and very limited interval spacing is adverse to the stress strain.
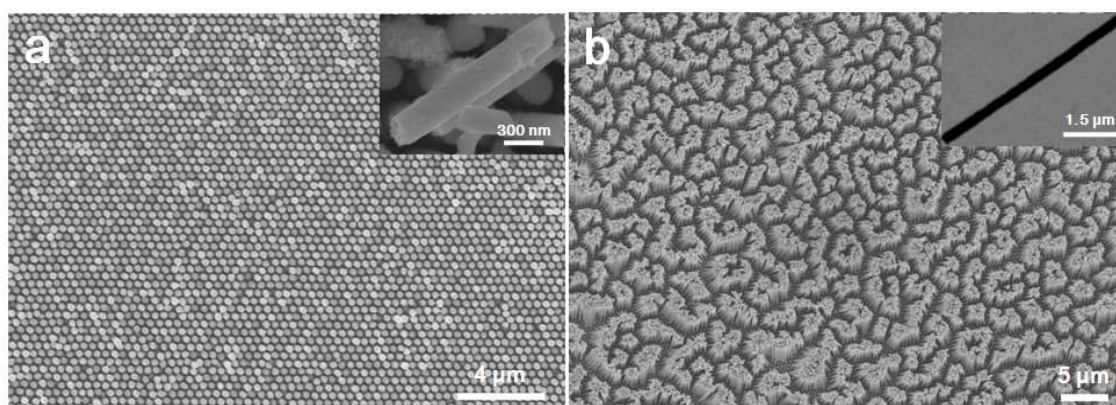
Figure 5-18 SEM images of (a) S-2-Sb NRs and (b) A-2-Sb NRs. The single Sb nanorod was observed by scratching Sb arrays off the Ni/Au substrate.

On the basis of the above results, it is reasonable to conclude that, although the aspect ratio has effects on the electrochemical performance of Sb nanorod arrays to some extent, highly ordered alignment and large enough interval spacing are determinate factors. The above results are consistent with those in the above where highly ordered arrays with large interval spacing are largely beneficial to the electrochemical performance.

Lastly, the remarkable electrode integrity is also largely beneficial for the excellent electrochemical performance. The good adhesion between Sb nanorod arrays and conductive substrate can ensure the robust arrays integrity to accommodate volume expansion/contraction upon cycling, resulting in good cycling and rate performance. To better verify this point, the morphology of Sb nanorod arrays after long-term cycling was also investigated. Figure 5-19 shows SEM and TEM images of Sb nanorod arrays cycled at a current density of 10 A g^{-1} after 70 cycles in fully desodiation state. As can be seen from the top (Figure 5-19a) and side view (Figure 5-19b), Sb nanorod arrays still maintain their highly ordered and vertically well-aligned feature with clear interval spacing after long-term cycling at such high current density, which prevents pulverization and preserves electrode integrity, giving rise to excellent cycling and rate performance. We scratched Sb nanorods off the substrate and observed the uniform and well-preserved Sb nanorods on TEM (Figure 5-19b inset) image. The diameter and length of the cycled Sb nanorod are around 300 nm and 2.1 μm, respectively, and larger than those of the pristine Sb nanorod (Figure 5-9h) with rough surfaces, deriving from the volume expansion/contraction in repeated sodiation/desodiation processes. Despite the volume change, there is no structural collapse and agglomeration of Sb nanorod arrays, suggesting the chemical and mechanical robustness of the arrays electrode. Benefiting from the above four major advantages of the electrode structure, Sb nanorod arrays anode showed the overall excellent electrochemical performance for Na-ion storage.
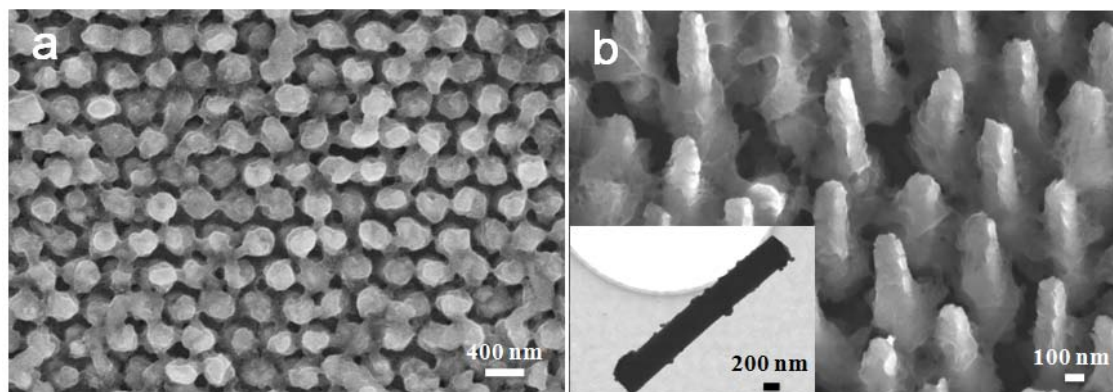
Figure 5-19 SEM images of (a) top view and (b) tilted view of Sb nanorod arrays electrode after 70 cycles at a current density of 10 A g^{-1}. (Inset: TEM image of a single Sb nanorod.)

5.2.5 Summary

We introduce a large-scale highly ordered Sb nanorod arrays with uniform large interval spacing and demonstrate its meaningful improvement in cycling life and power rate for Na-ion batteries. Used as additive-free SIBs anode, Sb nanorod arrays delivered a high capacity retention of 84% up to 250 cycles. Remarkably, the anode showed superior rate capability with high capacities of 579.7 and 557.7 mAh g^{-1} at 10 and 20 A g^{-1}, respectively, and fully recovered the low rate capacities. Significantly enhanced properties of this anode could be related to its pathbreaking electrode design which ensures high Na ion accessibility, excellent conductivity, and strong bonding with the substrate. These excellent electrochemical performances shall pave a way to develop more applications of Sb nanorod arrays in energy storage devices.

5.3 Hierarchical Sb-Ni nanoarray anode

To address the issue of drastic volume expansion, one effective method is to design integrated electrodes where nanosized active materials are grafted to a secondary matrix.[115, 146, 207, 243, 244] The unique electrodes can not only accommodate the large volume variation, but also provide fast electron transport and high ion accessibility. Their combination are three indispensable elements for excellent electrochemical performance. Growth of nanostructures with controllable dimensions has attracted growing interest due to the fact diverse properties can be generated by tailoring the morphology. Thereby, growing attention has been paid to designing metallic Sb with special morphologies, in particular in terms of the interparticle space and particle size.[39, 40, 245] It is widely accepted that

preparing nanosized Sb could enhance the tolerance of strain during alloying/dealloying processes, and shorten ion/electron transport pathways, consequently leading to high reversible capacity, long lifespan, and fast rate performance.[38, 44] For example, monodisperse antimony nanocrystals were used as SIB anodes and showed high capacities of about 550 and 520 mAh g^{-1} at current densities of 5.28 and 13.2 A g^{-1}, respectively.[39] A nanoporous-antimony anode was reported to show a high capacity of 573.8 mAh g^{-1} after 200 cycles at 100 mA g^{-1}.[125] Recently, due to the unique structural and mechanical strength with high surface-to-volume ratios, nanoplates have been extensively investigated and applied. Nanoplates-based electrode materials display short ion diffusion length, and large surface contact with electrolyte and conductive materials, which are conducive to enhancing the capacitive charge storage, thereby rendering excellent rate capability and high power density.

A promising electrode configuration have proven effective in constructing kinetically favourable Na-ion storage electrode, which is composed of three dimensional (3D) nanoarrayed current collectors as the secondary matrix for the graft of active materials. This 3D conductive open network increases contact area between current collectors and active materials and produces open channels for ions transport, hence resulting in large electrode/electrolyte interface area and fast ion/electron transport. Moreover, the unique 3D core/shell structures could effectively inhibit the aggregation of active materials and then provide better accommodation of large volume change upon cycling.[205, 223, 246-248] Traditional electrodes with a film structure generally need to use polymeric binders, which often suffer from insufficient ion permeation and block electron transport caused by insulated binder.[126, 127] By contrast, 3D additive-free nanoarrayed electrodes with excellent electric conductivity and self-integrity have many merits over the conventional electrodes.[58, 249] 3D additive-free nanoarrayed electrodes present the directly grown active materials on the current collector, thus avoiding the binder completely. In this way, it reduces harmful effect of binder and increase specific capacity. Due to growth, each active material is well bonded to the current collector, thus all of them contribute to the capacity. Taken together, the above mentioned features result in enhanced cycle life and high rate capability.

Based on the above concept, we herein report the synthesis of a new 3D nanostructured configuration for high-performance SIBs, in which Ni nanorod arrays are decorated with Sb nanoplates (3D Sb-Ni nanoarrays) by a nanoimprinted AAO template technique and a facile electrodeposition approach. This heterostructured electrode shows the synergetic

effect exerted by 2D nanoplates, open conductive array structure, as well as strong structural integrity. These combined electrode design significantly promotes the electron and ion transport and the mitigation of large volume expansion. Used as binder-free SIB anodes, 3D Sb-Ni nanoarrays demonstrated high specific capacity, long lifespan, and excellent rate performance. The encouraging results could provide insights of designing anode materials and provoke deeper understanding of material engineering strategies to improve SIBs performance.

5.3.1 Structural and morphological characterizations

Figure 5-20 illustrates a typical preparation procedure of the electrode. The design involves 3D Ni nanorod arrays as the electron collection and transport medium as well as the structural support and inactive condining buffer. Sb nanoplates are deposited on the Ni nanorod arrays as the electrochemical active material for Na-ion storage. Specificlly, first, a through-pore AAO template with conductive substrate (Au and Ni) is prepared, as seen in Figure 5-20a. The SEM image in Figure 5-20d clearly shows uniform AAO template with the pore diameter of around 210 nm. Next, by using the electrodeposition method, 3D Ni nanorod arrays are synthesized through AAO template that was subsequently dissolved (Figure 5-20b). Figure 5-20e displays that Ni nanorods are smooth, regular, and vertically aligned to the substrate. The bases of the rods show an average diameter of about 210 nm and the interval distance of 190 nm among nanorods. The unique Ni nanorod arrays could be used as efficient current collectors and skeletons for directly spontaneous growth of active materials with a high specific surface area and many active sites. The fabrication is finally finished by depositing Sb nanoplates on Ni nanorod arrays using electrodeposition method with the assistance of vacuum. As a result, 3D Sb-Ni nanoarrays with robust adhesion are achieved as a binder-free SIB anode, as shown in Figure 5-20c. Such an electrode configuration can enable fast ion/electron transport, large electrode/electrolyte interface area, and relieve the volume expansion upon cycling to ensure the electrode integrity. Figure 5-20f shows a typical SEM image of the Sb-Ni composite structure. It reveals that the products exhibit the hierarchical structures with high-quality and uniform in a large scale, from which rough surface of arrays can be observed, suggesting the successful deposition of Sb. Moreover, there is much uniform interspace available among arrays, indicating a highway of electrolyte penetration and a good volume variation accommodation. The magnified SEM image (Figure 5-20g) clearly presents the formation of Sb nanoplates grafted on Ni nanorod arrays, in which the Sb shell is composed of

randomly oriented Sb nanoplates that form a hierarchical architecture. A single Sb-Ni nanorod is observed in Figure 5-20h and i, in accordance with the above SEM results, where Sb nanoplates with about 20 nm in thickness are intercrossed with each other, forming highly porous nanoarchitectures with abundant open areas and electro-active surface sites. The views (Figure 5-20f-i) reveal that the morphology of the resulting electrode is composed of many densely packed nanoplates with regular shapes, implying that the prependicularly grown Ni nanorods are all covered by the Sb coating.
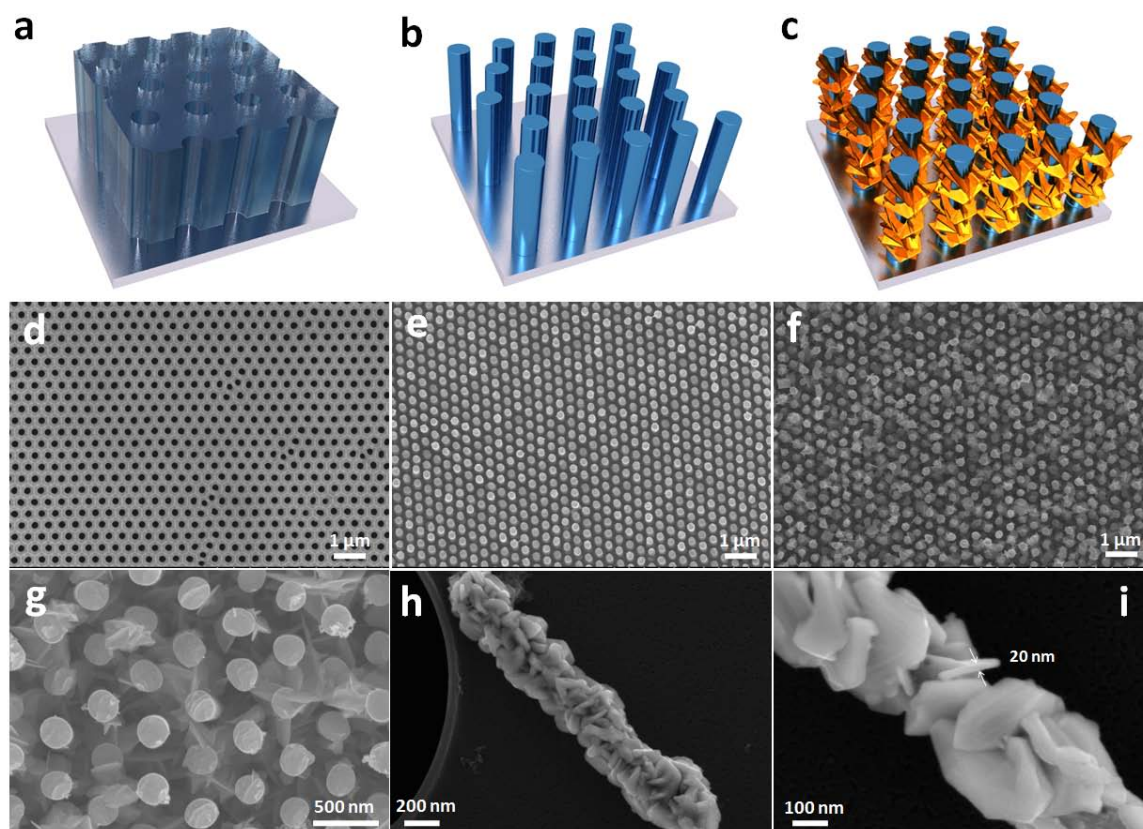
Figure 5-20 Schematic illustration of AAO template (a), Ni nanorod arrays (b), 3D Sb-Ni nanoarrays (c). SEM images of AAO template (d), Ni nanorod arrays (e), 3D Sb-Ni nanoarrays (f-i).

The crystalline phase of the prepared sample was investigated using XRD, as shown in Figure5-21a. Except for the reflections of the substrate (Au) and current collector (Ni), all the rest diffraction peaks for 3D Sb-Ni nanoarrays match well with those of standard XRD patterns of the rhombohedral Sb phase (JCPDS No. 35-0732), which further confirms the successful fabrication of Sb/Ni heterostructure. Further information of the hierarchical structure was achieved by performing HRTEM characterizations. Figure 5-21b-d display a dark-field SEM image, line scan profile, and EDX mapping results of a Sb-Ni nanorod,

distinctly manifest that the Ni nanorod is uniformly surrounded by the Sb nanoplates coating. A closer observation on a typical Sb-Ni nanorod is depicted in the HRTEM image (Figure5-21e), where the interface of the Sb layer and Ni nanorod is well-knit and seamless because the deposition process renders a good adhesion between the deposited coating and the substrate so that they retain contact during volume changes thereby increasing the cycability. Figure5-21f reveals that the Sb crystallites have distinct lattice spacing, in which the lattice fringes with the distances of 0.310 and 0.354 nm correspond to the (012) and (101) planes of rhombohedral Sb, respectively. The fast Fourier transform (FFT) pattern in Figure5-21f inset depicts the single crystalline characteristic of Sb.
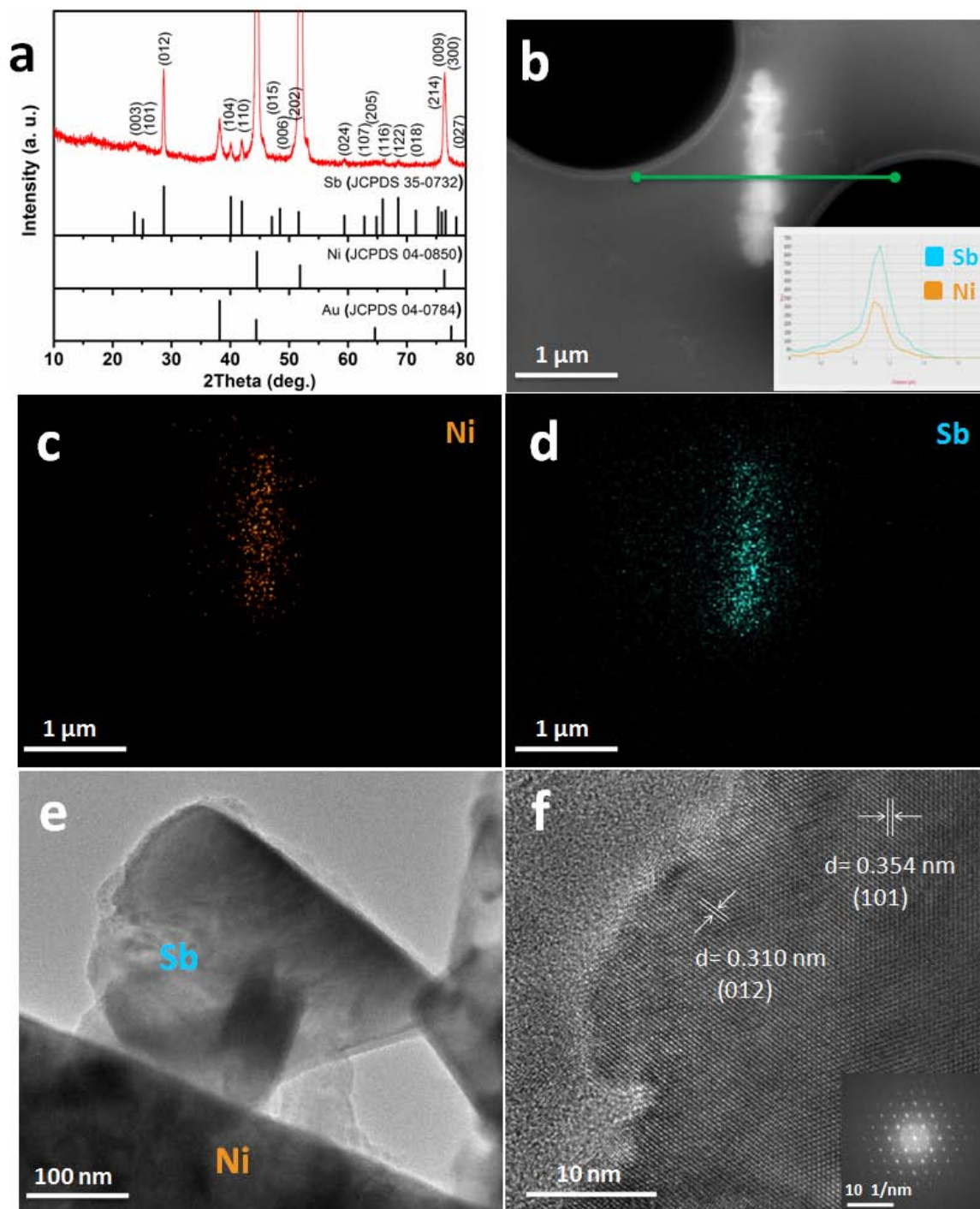
Figure 5-21 (a) X-ray diffraction pattern of 3D Sb-Ni nanoarrays. (b) Dark-field SEM image of Sb-Ni nanorod, and the corresponding line scan profile (b inset). EDX mapping for (c) Ni and (d) Sb elements. HRTEM images of Sb-Ni nanorod (e), Sb nanoplate (f), and FFT pattern (f inset).

5.3.2 Na-ion half cell performance

To evaluate the SIB performance of 3D Sb-Ni nanoarrays without overestimation, they are investigated as binder-free anodes in a Na-ion half cell. Figure 5-22a shows representative CV curves of the first three cycles at a scan rate of 0.1 mV s^{-1}. In the first sodiation scan, two strong broad peaks located at 0.42 and 0.37 V are shown, corresponding to the formation of a SEI layer, and amorphous Na$_x$Sb alloy phase which is subsequently transformed into cubic and hexagonal Na$_3$Sb through further sodiation.[250, 251] In the second sodiation scan, three distinct peaks at 0.67, 0.43 and 0.37 V are clearly observed, which are indexed to the multistep sodiation reactions between Sb and Na ions until a hexagonal Na$_3$Sb alloy is formed.[122] The difference between the first and second sodiation scan is mainly attributed to the formation of SEI layer and the rearrangement of the structure.[229, 237] In the desodiation scans, a broad peak ranging from 0.70 to 0.96 V is demonstrated, which derives from the phase transformation from Na$_3$Sb to Sb.

Figure 5-22b reveals the galvanostatic charge-discharge capacity and Coulombic efficiency versus cycle number plots at a current density of 0.5 A g^{-1}, offering a direct evidence of the excellent Na storage performance. The voltage profiles with different flat plateaus suggest the redox reactions associated with Na alloying/dealloying in the charge and discharge curves, which are in good accordance with the peaks observed in CVs. The first discharge and charge capacity are 880 and 640 mAh g^{-1}, with a low initial CE of 72.7%. The irreversible capacity ratio of 27.3% can be assigned to the initial formation of a SEI layer on the electrode surface as discussed above, and to the irreversible alloying of Na ions into Sb the coating. However, the efficiency gradually increase in the following cycles (about 98%). Furthermore, the excellent reproducibility of voltage profiles is presented from 1 to 100 cycles for both sodiation and desodiation have excellent, which suggests the high reversibility and stable structure of 3D Sb-Ni nanoarrays and during cycling.[229]

The cycling performance of 3D Sb-Ni nanoarrays anodes were studied at current densities of 0.5 and 1.0 A g^{-1}, respectively. As shown in Figure 5-22c, large reversible capacities and high capacity retentions are clearly observed. For example, at a current density of 0.5 A g^{-1}, a reversible capacity of 623 mAh g^{-1} is obtained at the 100th cycle, which is close to the theoretical capacity of Sb (660 mAh g^{-1}). The capacity retentions after 200 cycles are as high as 80% and 72% at 0.5 and 1.0 A g^{-1}, respectively. These values are much higher than most of reported Sb-based anodes.[36, 122, 222, 252] The capacity fade of 3D Sb-Ni nanoarrays can be attributed to the increasing thickness of the SEI layer and inevitable volume

changes upon cycling. Except for the initial several cycles, the CE is close to 98% at both 0.5 and 1.0 A g^{-1}, suggesting facile ion and electron transport in the 3D Sb-Ni nanoarrays anodes.[221, 236, 237] The improved cyclability are associated with the optimized Ni-Sb configurations where the inactive Ni matrix as well as the space acts as the confining buffer to release the large volume changes and alleviate the concomitant huge stresses owing to repeated Na alloying/dealloying with Sb.
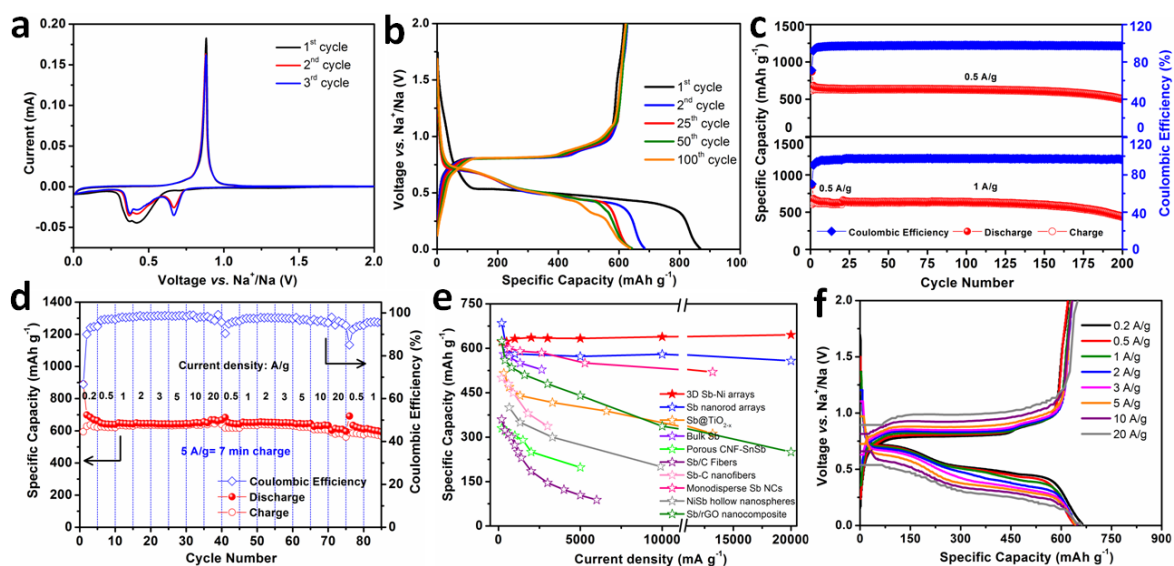
Figure 5-22 Electrochemical performance of 3D Sb-Ni nanoarrays anodes. (a) Cyclic voltammetry at a scan rate of 0.1 mV s^{-1} between 0.01 to 2.0 V (*vs.* Na$^+$/Na). (b) Galvanostatic charge/discharge voltage profiles in different cycles at a current density of 0.5 A g^{-1}. (c) Cycling performance at current densities of 0.5 and 1.0 A g^{-1}. (d) Rate performance at various current densities from 0.1 to 20 A g^{-1}. (e) Ragone plots of 3D Sb-Ni nanoarrays anode and other Sb-based SIBs anodes from literature (Sb nanorod arrays,[253] Sb@TiO$_{2-x}$,[44] bulk Sb,[122] porous CNF-SnSb,[229] Sb-C nanofibers,[132] monodisperse Sb NCs,[39] NiSb hollow nanospheres,[45] Sb/rGO nanocomposites, Sb/C fibers[222]). (f) Charge/discharge voltage profiles at various current densities from 0.1 to 20 A g^{-1}.

Owing to the unique 3D heterostructured configuration, 3D Sb-Ni nanoarrays anodes are expected to make high rate capability feasible. Figure 5-22d illustrates the rate performance tested at various current densities from 0.2 to 20 A g^{-1}. The reversible capacity of the anode is found to be very high and quite stable (especially, after few initial cycles). Even at very high rates of 10 and 20 A g^{-1}, the anode still can be reversibly cycled and maintains high CEs of about 98%. To specifically understand the stability of the capacity, 3D Sb-Ni nanoarrays anodes were cycled five times at each current rate again. In

the second rate test, the capacity level is still rather stable at each rate, regardless the rate cycling history. It is greatly noticeable that, in the second set, it still delivers large capacities of 607 and 580 mAh g^{-1} at 10 and 20 A g^{-1}, respectively, indicating the fast transfer of Na ion and electron through 3D Sb-Ni nanoarrays anodes. Further cycling at a low rate of 0.5 A g^{-1} in the third rate test, the capacity retention is around 94% of the capacities at the same rate in the first set, implying that 3D Sb-Ni nanoarrays have strong structure tolerance to endure greatly varying rates while simultaneously keeping high energy densities. This rate capability and their specific capacities are on the top of reported Sb-based anodes (Figure 5-22e). Figure 5-22f presents the corresponding voltage profiles of the anode at various current densities in the first set. Despite the increasing current densities from 0.2 to 20 A g^{-1}, both charge and discharge voltage profiles have quite similar shapes with minimal increase of the voltage offset. Furthermore, in the second set, when the anode was cycled at 0.5, 1.0, 0.5, and 10 A g^{-1} again, the voltage profiles recovered and are perfectly reproducible in comparison with those of the first set at the same current densities (Figure 5-23). All these features show facile electron transport and small mechanical energy loss in the 3D Sb-Ni nanoarrays anodes.
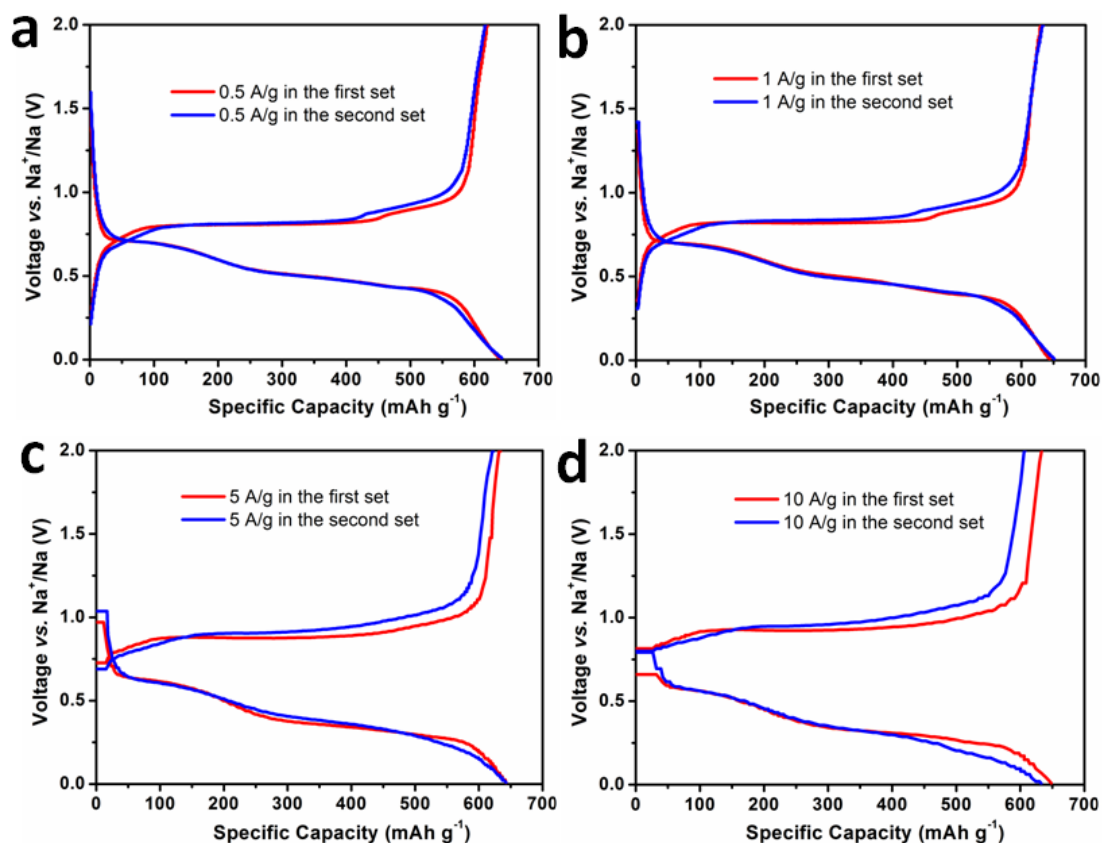
Figure 5-23 Galvanostatic charge/discharge voltage profiles of 3D Sb-Ni nanoarrays at various current densities in different sets.

5.3.3 Kinetic and quantitative analysis of Na^+ storage mechanism

In order to understand the superiority of the high-rate performance of 3D Sb-Ni nanoarrays, we need to closely study the CV curves. CV has been proven to be a powerful technique to evaluatethe electrochmical kinetics of electrode materials towards Na^+. Here, kinetic analysis based on CV analysis was carried out to gain further insight into the electrochemistry of the 3D Sb-Ni nanoarrays/Na cell. The CV curves at various scan rates from 0.1 to 10 mV s^{-1} are presented in Figure 5-24a, which possess similar shapes with broad peaks during both cathodic and anodic processes. CV curves could be employed to distinguish the diffusion-controlled contribution and capacitive contribution in the reaction based on the slope (*i.e.*, *b* value) calculated by the plots of log (peak current, i_p) to log (scan rate, v).[254] Generally, *b*=1 and 0.5 separately indicate that the electrochemical reactions are surface-limited and diffusion-limited with former corresponding to a capacitive behavior and Na^+ ion insetion/extraction. Usually, *b* values are between 0.5-1, implying both contribute to the reaction. In Figure 5-24b, 3D Sb-Ni nanoarrays display that

b values are 0.82, 0.78 and 0.84 for three cathodic peaks, respectively, indicating the capacitive contribution for the Na-storage reactions in 3D Sb-Ni nanoarrays. Moreover, the contribution of the total capacity (Q) storage can be analyzed using Trasatti's method which describes the relationship between the capacity and the sweep rate.[255] The Q involves capacity from surface process (Q_s) and the diffusion-controlled process (Q_d), as given in Equation (1)

$$Q\ (v) = Q_s + Q_d = Q_s + k\ (v^{-1/2}) \qquad (1)$$

Here k is a constant and v is the potential scan rate. The Q_d is the diffusion-controlled capacity, which is limited by $v^{-1/2}$. The surface capacity (Q_s) will be constant with the scan rate, which can be determined from the plot of capacity (Q) *vs.* $v^{-1/2}$. The extrapolation of the linear fit to the data to the *y*-intercept ($v^{-1/2}$=0) gives the contribution of capacitive (Q_s), which is calculated to be 131.9 mC cm^{-2} (Figure 5-24c). Moreover, the relative contributions related to capacitive and diffusion-controlled processes can be identified, as shown in Figure 5-24d. As the scan rate increases, the role of capacitive contribution further enlarges. The contribution is 84% at a scan rate of 0.1 mV s^{-1}, and reaches 99% at 10 mV s^{-1}. It is reported that capacitive contribution plays a critical role for the structures with high surface area and/or high porosity. Generally, the greater the capacitance is, the better the rate capability is.[44, 254] This fact explains the excellent rate performance of 3D Sb-Ni nanoarrays. To the best of our knowledge, such a stable and robust rate capability has not been reported for Sb-based anodes, which strongly confirms the effectiveness of our electrode design.
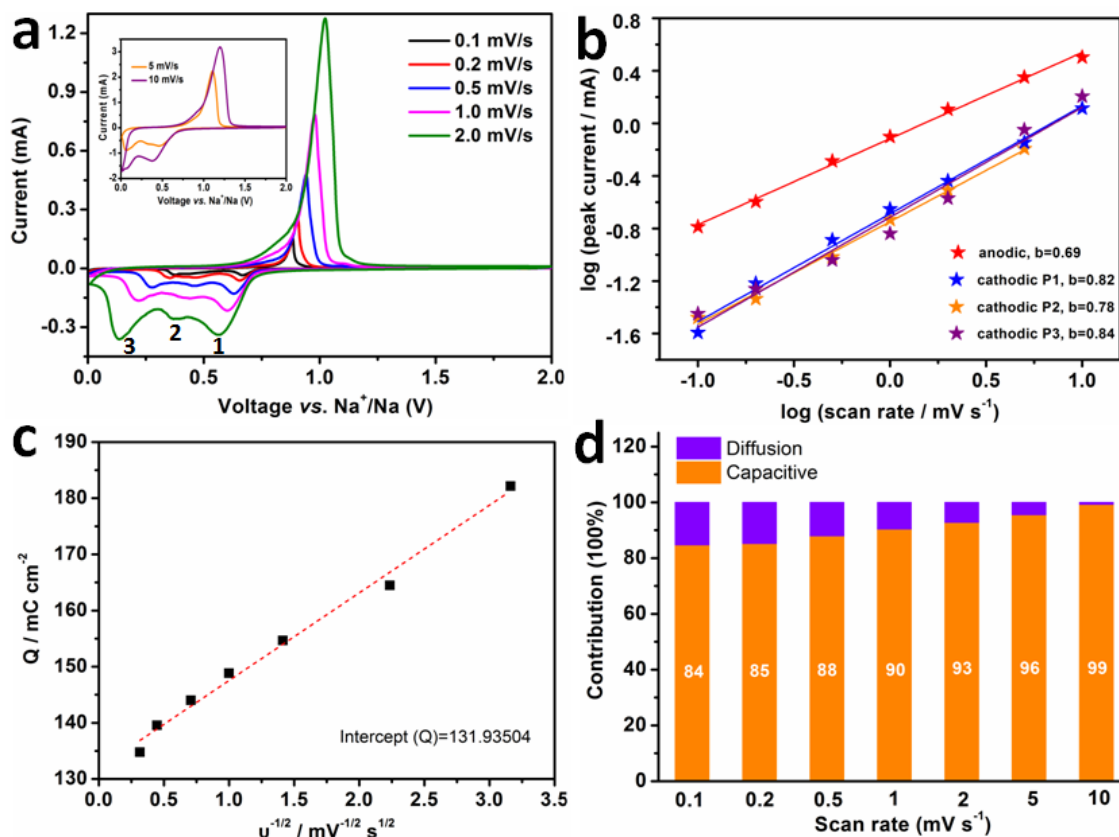
Figure 5-24 Kinetic and quantitative analysis of the Na$^+$ storage mechanism. (a) CV curves of 3D Sb-Ni nanoarrays at different scan rates from 0.1 to 10 mV s^{-1}. (b) The plots of log (i_p) to log (v) for cathodic/anodic peaks. (c) Trasatti analysis utilizing the dependence of charge storage on the reciprocal square root of the scan rates. In the plot of capacity (Q) *vs.* $v^{-1/2}$, the y-intercept corresponds to the infinite sweep rate capacity, $Q_{v=\infty}$. (d) Normalized contribution ratio of capacitive (orange yellow) and diffusion-controlled (blue) capacities at different scan rates calculated using Trasatti analysis described in Equation (1).

5.3.4 Factors analysis for great electrochemical performance

The excellent electrochemical performance of 3D Sb-Ni nanoarrays can be attributed to the rational design and engineering of the unique nanostructure, which is elaborated as follows. On one hand, the enhanced capacity and excellent rate capability largely contribute from the following structural features. First, Sb nanoplates have an increased portion of exposed surfaces and thus can provide more active sites for Na$^+$ ions accesses as well as short distance for Na$^+$ ions diffusion. Next, every Ni nanorod provides a direct and fast electron pathway to each Sb nanoplate. Meanwhile, in this open and vertically aligned 3D

nanostructure array, highway of electrolyte ions is achieved to realize maximum utilization of electro-active materials at high rates. One possible interface effect in the Sb/Ni heterogeneous structure was anticipated to provide additional charge storage in the electrode, and the phenomenon has been observed in other reported works.[256-262]

On the other hand, relieving large volume changes of Sb is another extremely important point to achieve improved rate capability and cycling life. In this work, Sb nanoplates are directly grafted on Ni nanorod arrays, in which several features are conducive to mitigate the volume variations. First, the Ni nanorod acting as a scaffold provides a large surface area for the growth of Sb nanoplates, and then well dispersed and immobilized Sb nanoplates are obtained, thereby inhibiting the agglomeration of active materials. Meanwhile, the direct growth of Sb nanoplates on Ni nanorod backbone could ensure firm bonding to the current collector, and Ni skeletons could effectively suppress the adverse mechanical effect from the large volume expansion. From the improved capacity and cycle life, the advantages of the assembly of Sb nanoplates on Ni nanorod arrays are fully demonstrated. In comparison, a planar Sb electrode on Ni foil is fabricated by electrodeposition under the same conditions. As seen in Figure 5-25a and b, the planar Sb electrode is constructed by severely aggregated Sb nanoplates on Ni foil. The planar electrode shows a dramatic fade in capacity upon cycling and much larger resistances than those of 3D Sb-Ni nanoarrays (Figure 5-25c-d), as a result of the large volume change and pulverization (Figure 5-25e-f). Second, the sufficient interspace between arrays effectively mitigates the strain caused during Na alloy/dealloy processes. As shown in Figure 5-26a, with increasing deposition time, the interspace among nanorods was filled with Sb. The limited interspace would reduce the electrolyte accessibility to the space among rods (Figure 5-27), and volume buffering of Sb could not be well achieved during discharge and charge cycling. These disadvantages result in poor capacity retention ability and rapidly increased resistances (Figure 5-26b-d). Therefore, the sufficient interspace is an important parameter for the assembly of Sb nanoplates on Ni nanorods electrode. Third, the void space between these plate-like subunits also could buffer the volume expansion and contraction.
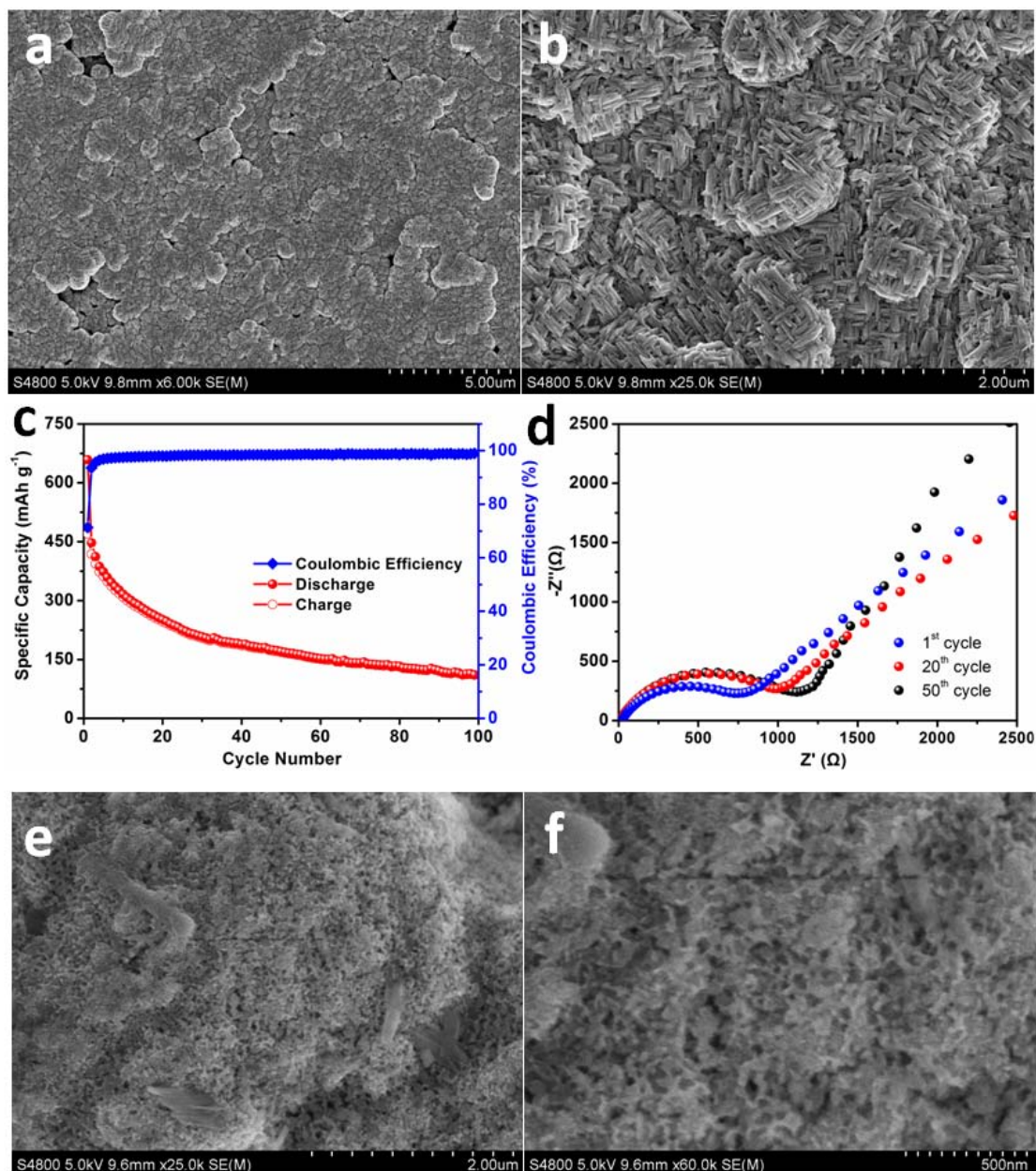
Figure 5-25 (a and b) SEM images of planar Sb electrode on Ni foil. (c) Cycling performance of planar Sb electrode on Ni foil at a current density of 0.5 A g⁻¹. (d) Nyquist plots of planar Sb electrode at charge state (2.0 V) from 1 MHz to 10 mHz. (e and f) SEM images of cycled planar Sb electrode after 200 cycles at 0.5 A g⁻¹.
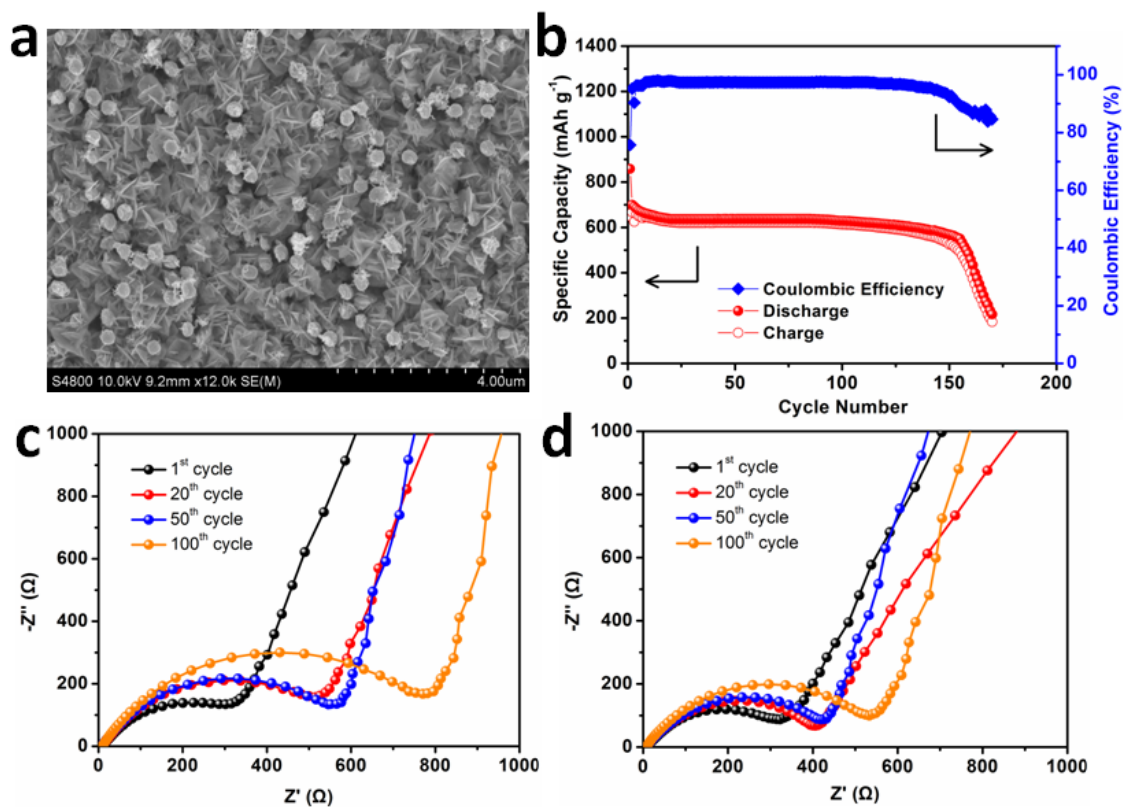
Figure 5-26 3D Sb-Ni nanoarrays with insufficient interspace: (a) SEM image, (b) Cycling performance at 0.5 A g^{-1}, (c) Nyquist plots at charge state (2.0 V) from 1 MHz to 10 mHz. (d) Nyquist plots of 3D Sb-Ni nanoarrays at charge state (2.0 V) from 1 MHz to 10 mHz.
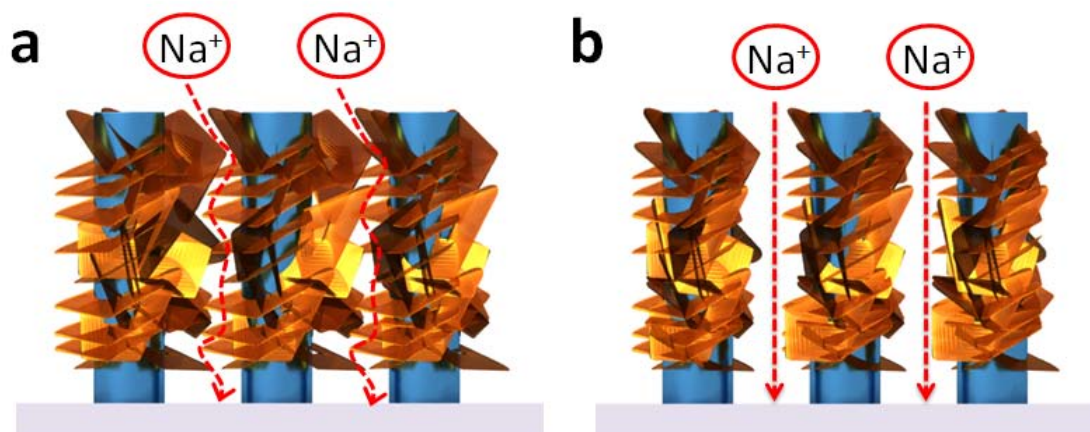
Figure 5-27 Schematic illustration of transport mechanism of Na ions in 3D Sb-Ni nanoarrays without (a) and with (b) sufficient interspace.

Last but most important, although the above strategies can alleviate the large volume variation to a certain extent, due to inherent nature of Sb, the volume change still is

inevitable. In particular, with further cycling, the mechanical breakdown of Sb is obvious. The advantage of 3D Sb-Ni nanoarrays is manifested when such breakdown happens. A distinct comparison can be found in bare 3D Sb nanorod arrays. In the case of Sb nanorod arrays, owing to the loss of electrical contact with the conductive substrate, the whole nanorod beyond the cracking point becomes inaccessible (Figure 5-28a), severely decreasing the overall capacity. However, in the case of 3D Sb-Ni nanoarrays, such breakdown has relatively limited influence on the overall capacity since Sb nanoplates that don't fall off can still be connected to the Ni nanorods, as shown in Figure 5-28b. The overall capacity fades at a comparatively slower pace than that of the nanorods-based nanostructures (Figure 5-29). The morphology of 3D Sb-Ni nanoarrays after cycling confirmed the above point. Figure 5-30a and b display the SEM images of the after-cycled arrays. Compared to the image of the pristine sample, the morphology shows less variation, implying that this electrode structure can effectively accommodate the huge volume change during sodiation/desodiation. After 200 discharge/charge cycles, the gaps between each nanoplate became indistinct whereas some crevices can be observed to form small coordinated regions randomly on the surface. With a volume change of 390% because of Na-Sb alloying, the Ni/Sb nanorods agglomerate; after Na-Sb dealloying, they shrink again, however not to the original morphology but preferably into self-adjusted flakes to relieve the stresses. After repeated cycling, the Sb nanoplates seem to break into smaller nanoplates and have a certain degree of crush in its platy structure, showing loose-packed structure (Figure 5-30c). Despite that, a majority of Sb nanoplates are still tightly attached to Ni nanorods because the Ni nanorods stick to the Sb coating tightly and therefore the coating is not shed off. Only small capacity decay is shown, confirming the structural stability of 3D Sb-Ni nanoarrays. Figure 5-30d depicts the crystallinity of 3D Sb-Ni nanoarrays after cycling. The distinct lattice spacing is observed, in which the lattice fringe with the distance of 0.221 nm correspond to the (104) planes of rhombohedral Sb.
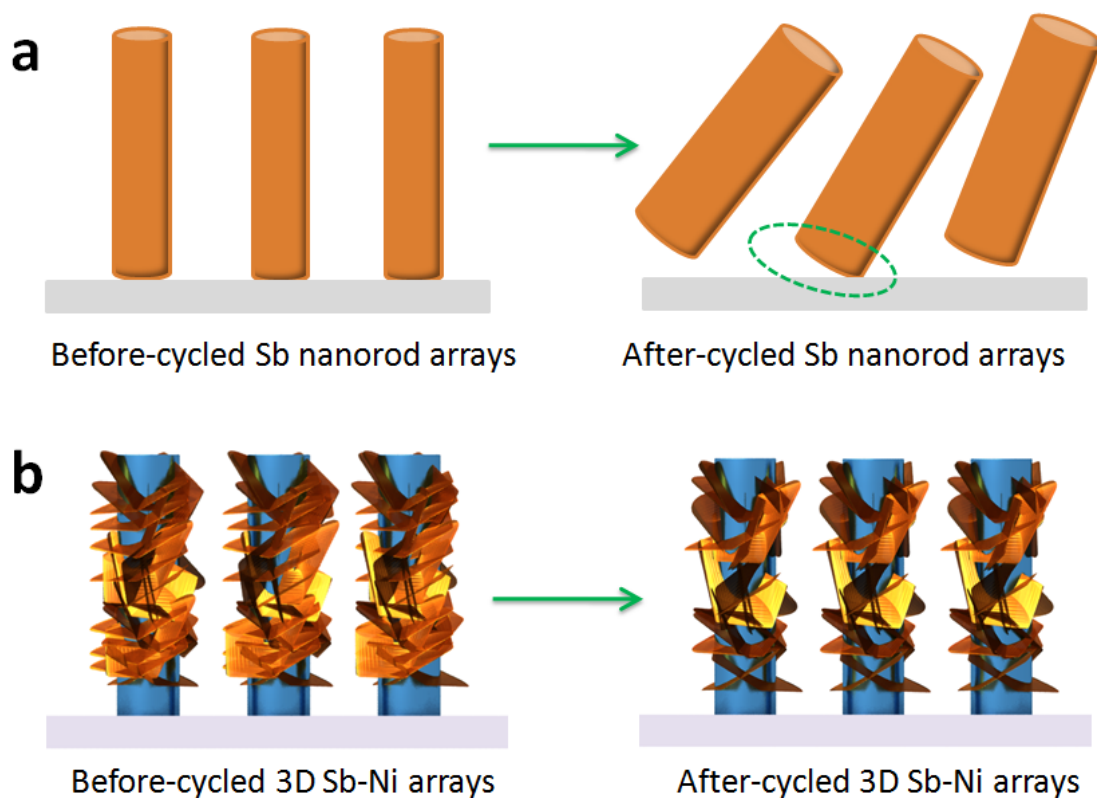
Figure 5-28 Schematic illustration of after-cycled fade mechanism of bare Sb nanorod arrays (a) and 3D Sb-Ni nanoarrays (b).
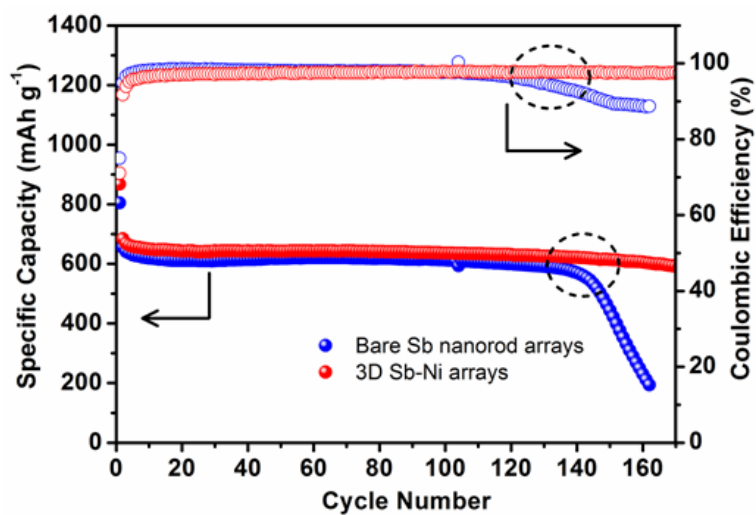
Figure 5-29 The comparison of cycling performance between bare Sb nanorod arrays and 3D Sb-Ni nanoarrays.
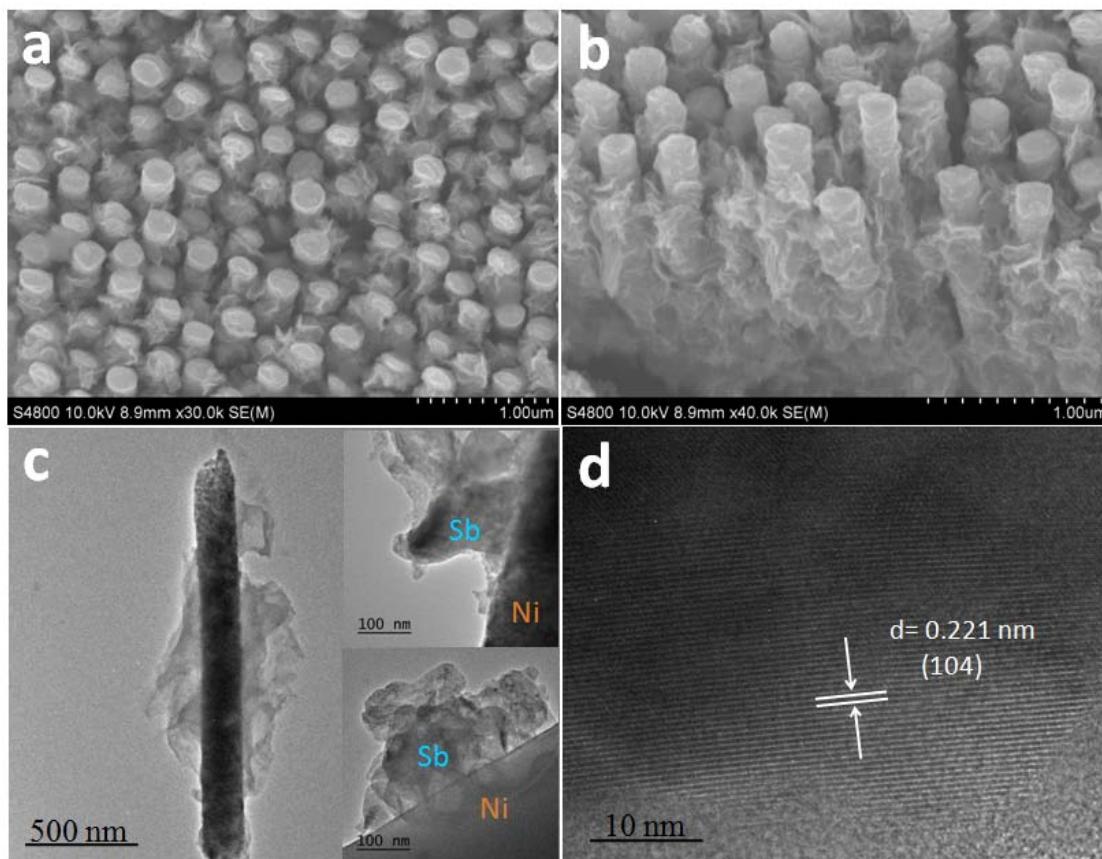
Figure 5-30 (a, b) SEM images and (c, d) HRTEM images of 3D Sb-Ni nanoarrays anodes after 200 cycles.

5.3.5 Summary

To tackle the issues of the rapidly fading capacity and poor rate capability of Sb anodes derived from large volume changes, we report the syntesis of a novel nano-heterostructure composed of Sb nanoplates on Ni nanorod arrays by combining a nanoimprinted AAO technique and a facile electrodeposition method. As a proof-of-concept demonstration of the function, such 3D Sb-Ni nanoarray composite material is used as binder-free SIB anode. It exhibits high capacity retention of 80% over 200 cycles at a high current density of 0.5 A g^{-1}, and excellent rate capacity up to 20 A g^{-1} with the capacity of 580 mAh g^{-1}. The synergistic effect exerted by the 2D nanoplates, open conductive array structure, and strong structural integrity are probably responsible for the enhanced performance. Moreover, a capacitive behavior is verified by kinetics analysis. The capacitive charge storage has the advantage of rendering high charging rate and therefore high power. It is expected that this design strategy is applicable to modulating other electrodes for advanced energy storage systems.

5.4 Investigations of Na-ion full-cell performance

5.4.1 Characterizations of positive materials

5.4.1.1 Structural characterizations of P2-Na$_{2/3}$Ni$_{1/3}$Mn$_{2/3}$O$_2$

The crystal structure of the as-prepared material was studied by XRD as shown in Figure 5-31a. The XRD pattern shows a layered structure which belongs to the hexagonal P63/mmc space group, indexed as a P2-type structure. The typical layered morphology is also observed in Figure 5-31b, in which a series of planes constitute single particles with an average size of 1~2 μm. Therefore, layered P2-Na$_{2/3}$Ni$_{1/3}$Mn$_{2/3}$O$_2$ has been successfully synthesized.
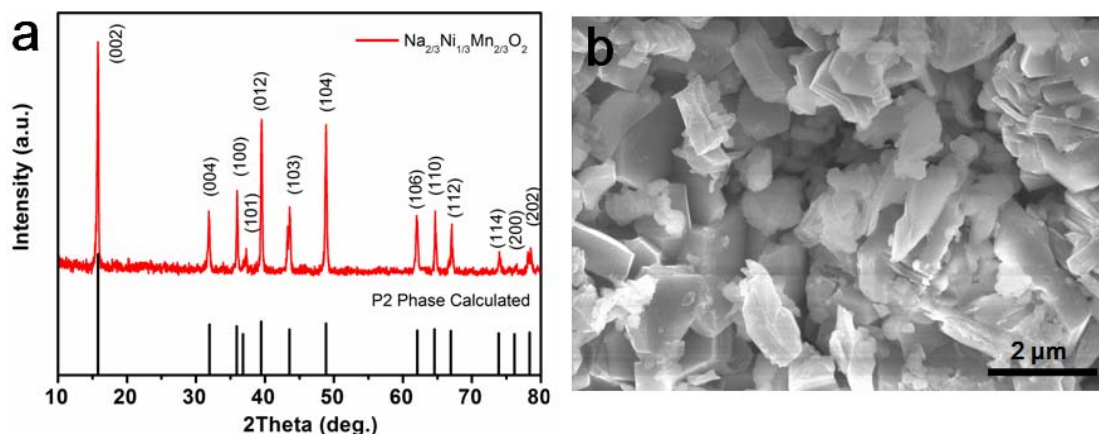
Figure 5-31 (a) XRD pattern and (b) SEM image of layered P2-Na$_{2/3}$Ni$_{1/3}$Mn$_{2/3}$O$_2$.

5.4.1.2 Electrochemical performance of P2-Na$_{2/3}$Ni$_{1/3}$Mn$_{2/3}$O$_2$

The electrochemical performance of as-prepared P2-Na$_{2/3}$Ni$_{1/3}$Mn$_{2/3}$O$_2$ in a half cell was investigated in the electrolyte of 1 M NaClO$_4$ in EC: PC (1:1 by volume) with the addition of 5% FEC. Figure 5-32a displays its CV profiles of the first five cycles, which have similar shapes with reported P2-Na$_{2/3}$Ni$_{1/3}$Mn$_{2/3}$O$_2$ cathodes.[90, 91, 263] Galvanostatic charge/discharge curves of P2-Na$_{2/3}$Ni$_{1/3}$Mn$_{2/3}$O$_2$ at a current density of 30 mA g^{-1} were also conducted, as shown in Figure 5-32b. The cut off potential was set to 2.7-4.0 V (*vs.* Na$^+$/Na), because it was reported that this range can ensure the reversibility of P2-Na$_{2/3}$Ni$_{1/3}$Mn$_{2/3}$O$_2$ cathode.[234] It can be seen that P2-Na$_{2/3}$Ni$_{1/3}$Mn$_{2/3}$O$_2$ showed typical and reversible voltage profiles, which are consistent with the characteristic peaks on the CV curves in Figure 5-32a. A reversible capacity for this cathode of 38 mAh g^{-1} is obtained between 2.7-4.0 V at a current density of 30 mA g^{-1}. Figure 5-32c shows its cycling

performance, in which P2-$Na_{2/3}Ni_{1/3}Mn_{2/3}O_2$ maintained superior cycling stability (100% capacity retention over 100 cycles) and high CE of around 99.5%.
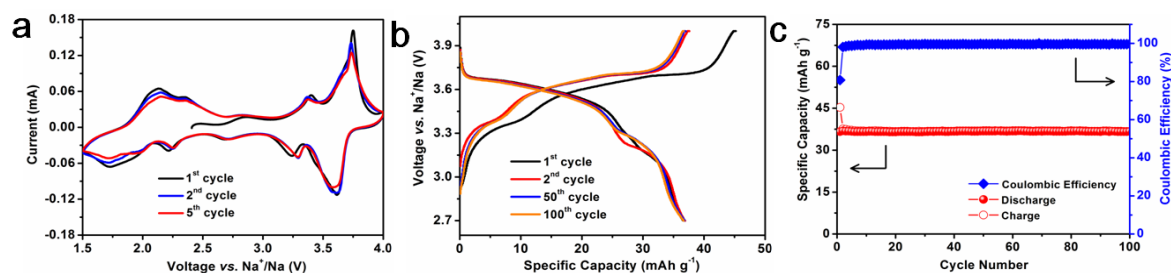
Figure 5-32 Electrochemical performance of layered P2-$Na_{2/3}Ni_{1/3}Mn_{2/3}O_2$ in a Na cell. a) Cyclic voltammetry at a scan rate of 0.1 mV s^{-1} between 1.5 to 4.0 V (*vs.* Na$^+$/Na). b) Galvanostatic charge/discharge voltage profiles in different cycles, and c) cycling performance at a current density of 30 mA g^{-1} between 2.7 to 4.0 V (*vs.* Na$^+$/Na).

5.4.1.3 Structural characterizations of $Na_3V_2(PO_4)_3$/C

To confirm the structure of $Na_3V_2(PO_4)_3$/C sample, XRD observation was characterized and shown in Figure 5-33a. The XRD pattern is in good agreement with the framework of a rhombohedral NASICON structure with the R$\overline{3}$c space group (ICDD#01-078-7289), and impurity phases have not been detected, indicating that $Na_3V_2(PO_4)_3$/C has been successfully synthesized. As shown in Figure 5-33b, the morphology and size of $Na_3V_2(PO_4)_3$/C were characterized by SEM, in which it has an irregular morphology and the average particle size is about 1 to 2 μm.
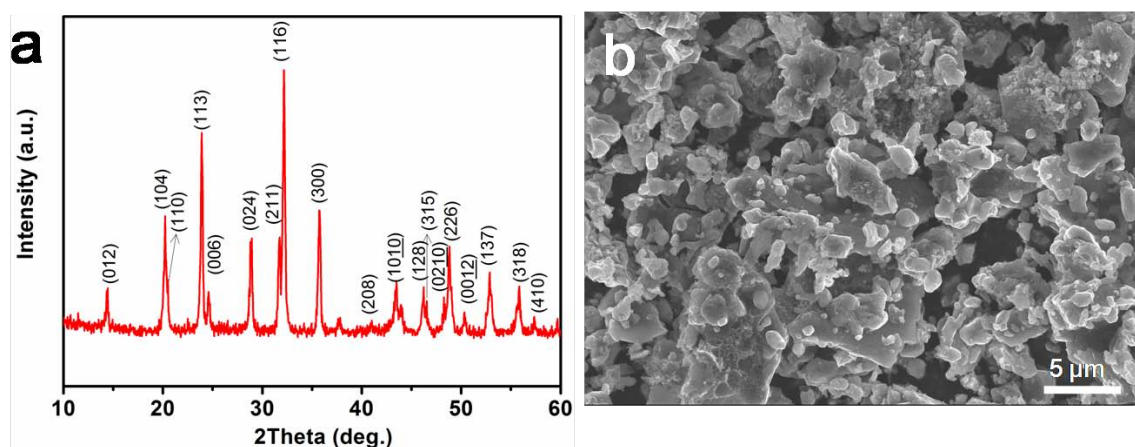
Figure 5-33 (a) XRD pattern and (b) SEM image of $Na_3V_2(PO_4)_3$/C.

5.4.1.4 Electrochemical performance of Na₃V₂(PO₄)₃/C

In order to investigate the electrochemical intercalation behavior of Na ions, cyclic voltammetry was performed in the potential window of 2.7-4.0 V at 0.1 mV s^{-1}, as shown in Figure 5-34a. A couple of oxidation and corresponding reduction peaks near 3.4 V can be observed, which are typical of Na-ion extraction and insertion with the V^{4+}/V^{3+} redox couple. Figure 5-34b shows its charge/discharge voltage profile that is consistent with the characteristic peaks on the CV curve in Figure 5-34a. The cycle performance was measured at a current density of 80 mA g^{-1}, as shown in Figure 5-34c. The Na₃V₂(PO₄)₃/C cathode delivered the initial reversible capacity of 98 mAh g^{-1} with the CE of 86%. After 50 cycles, the capacity was 95 mAh g^{-1} with the CE of 99%, and the capacity retention of 50 cycles is as high as 97%.
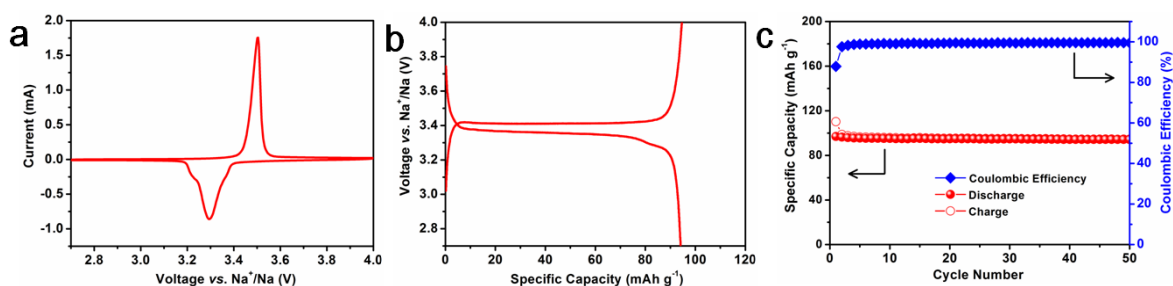
Figure 5-34 Electrochemical performance of Na₃V₂(PO₄)₃/C cathode. (a) Cyclic voltammetry at a scan rate of 0.1 mV s^{-1} between 2.7 to 4.0 V (*vs.* Na$^+$/Na). (b) Galvanostatic charge/discharge voltage profile, and (c) cycling performance at a current density of 80 mA g^{-1} between 2.7 to 4.0 V (*vs.* Na$^+$/Na).

5.4.2 Full-cell performance of hierarchical fern leaf-like Sb

To elucidate the potential practical application of the as-prepared the fern leaf-like Sb for Na-ion batteries, two different full cells were assembled by using two different cathode materials (P2-Na$_{2/3}$Ni$_{1/3}$Mn$_{2/3}$O$_2$ and Na₃V₂(PO₄)₃/C). The electrochemical performances of the fern leaf-like Sb//Na$_{2/3}$Ni$_{1/3}$Mn$_{2/3}$O$_2$ full cell is shown in Figure 5-35. First, the CV curves of the full cell is investigated with a voltage range of 1.4-4.0 V, which shows well-defined oxidation and reduction peaks and excellent reproducibility (Figure 5-35a), indicating the good stability of fern leaf-like Sb electrode again. The cycling performance can be seen in Figure 5-35b. The full cell affords a high capacity retention of 70% (based on the anode mass) of the theoretical capacity of Sb (660 mAh g^{-1}) after 100 cycles with a high CE of about 97.5 % at 0.5 A g^{-1}.

In addition of the high capacity and long lifespan, the full cell also exhibits excellent rate capability, which delivers the reversible capacities of 565, 540, 505, 470, 440, 405 and 370 mAh g^{-1} at current densities of 0.2, 0.5, 1.0, 2.0, 3.0, 5.0 and 10 A g^{-1}, respectively, with high CEs (Figure 5-35c). To further demonstrate the stability of the capacity, the full cell was subjected to 40 charge/discharge cycles at 0.2 A g^{-1} after cycling at various rates. The reversible capacity recovered to 520 mAh g^{-1}, which is 92% of the initial reversible capacity, and kept stable up to 75 cycles. The CE of the full cell is also very high, more than 95%. Figure 5-35d presents the corresponding voltage profiles of the full cell at various current densities. Regardless of the growing current densities from 0.2 to 10 A g^{-1}, both charge and discharge profiles retain the similar shapes. The operation voltages are in the range of 2.5 and 2.8 V. The superior rate capability could be ascribed to the stable electrode structure.
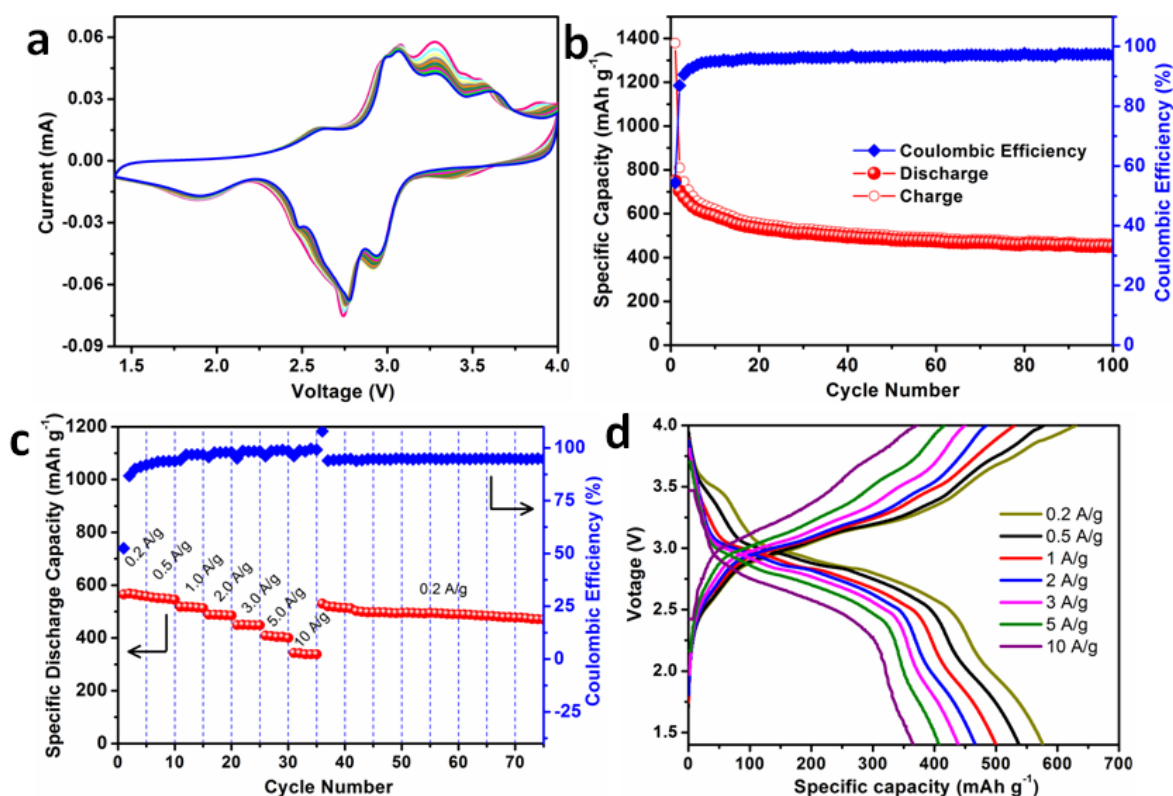
Figure 5-35 Electrochemical performance of fern leaf-like Sb// Na$_{2/3}$Ni$_{1/3}$Mn$_{2/3}$O$_2$ full cell. (a) CV curves at a scan rate of 0.3 mV s^{-1} at a voltage range of 1.4-4.0 V with 10 cycles. (b) Cycling performance at a current density of 0.5 A g^{-1} (with respect to the anode weight). (c) Rate capability (with respect to the anode weight) at various current densities from 0.2 to 10 A g^{-1}. (d) Charge/discharge voltage profiles at various current densities from 0.2 to 10 A g^{-1}.

The fern leaf-like $Sb//Na_3V_2(PO_4)_3/C$ full cell also displays a high capacity, good cyclability and rate capability, as shown in Figure 5-36. Although its electrochemical perforamce is not as good as the fern leaf-like $Sb//Na_{2/3}Ni_{1/3}Mn_{2/3}O_2$ full cell, a lot optimizations can be taken, such as adjusting the mass ratio of fern leaf-like Sb and $Na_{2/3}Ni_{1/3}Mn_{2/3}O_2$ as well as changing the measured voltage ranges. So far, the performances of the two full cells are much better than those of reported Sb-based full cells.[45, 234, 264] The above results fully prove that fern leaf-like Sb anode has strong feasibility for Na-ion storage in practice.
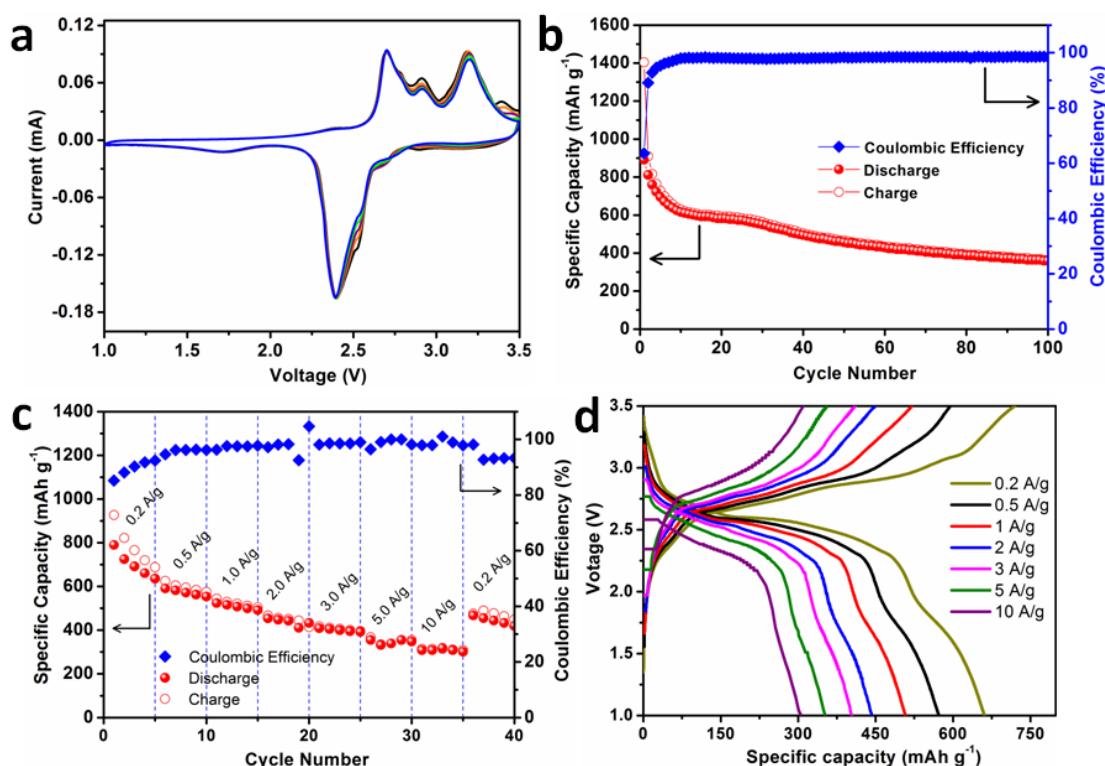
Figure 5-36 Electrochemical performance of fern leaf-like $Sb//Na_3V_2(PO_4)_3/C$ full cell. (a) CV curves at a scan rate of 0.3 mV s^{-1} at a voltage range of 1.0-3.5 V. (b) Cycling performance at a current density of 0.5 A g^{-1} (with respect to the anode weight). (c) Rate capability (with respect to the anode weight) at various current densities from 0.2 to 10 A g^{-1}. (d) Charge/discharge voltage profiles at various current densities from 0.2 to 10 A g^{-1}.

5.4.2 Full-cell performance of large-scale highly ordered Sb nanorod arrays

To display the feasibility of Sb nanorod arrays in full-cell configuration, a full cell coupled by $P2-Na_{2/3}Ni_{1/3}Mn_{2/3}O_2$ cathode and Sb nanorod arrays anode was investigated. This full cell was measured with a voltage range of 1.4-4.0 V at a large current density of 0.5 A g^{-1} (with respect to the anode weight) using 1.0 M $NaClO_4$ in EC-PC-5% FEC electrolyte.

According to the average working potentials of 3.6 and 0.7 V *vs.* Na^+/Na for P2-$Na_{2/3}Ni_{1/3}Mn_{2/3}O_2$ cathode (Figure 5-32b) and Sb nanorod arrays anode (Figure 5-11b), respectively, it is reasonably deduced that the full cell operates at around 2.9 V, as indeed shown by Figure 5-37a reflecting charge/discharge profiles of the full cell. Figure 5-37b shows the cycling performance of this full cell, in which it delivers a superior capacity retention of around 94% before 110 cycles with a capacity of around 620 mAh g^{-1} (relative to Sb anode weight), which is very close to the theoretical capacity of Sb (660 mAh g^{-1}). From the 110th cycle to the 130th cycle, this cell shows a capacity decay to 450 mAh g^{-1}. This decay characteristic is similar with Na/Sb half cell, due to the inevitable morphology change of Sb (Figure 5-12). Nevertheless, at such a high current density of 0.5 A g^{-1}, this cell still can work with a high capacity of about 334 mAh g^{-1} up to 250 cycles and extremely stable CE of around 98%. Although the capacity of the 250th cycle is only 54% the 110th capacity, the value of 334 mAh g^{-1} is very attractive considering at such large current density of 0.5 A g^{-1}. Moreover, according to the above studies, the cycling stability of this full cell might be better at a lower current density.

Notably, this full cell also displayed high rate capability, as shown in Figure 5-37c. Benefiting from the great rate capability of the Na/Sb half cell, it can be cycled at very large current densities of 10 and 20 A g^{-1}, and maintained stable reversibility. In addition, these capacities can be fully recovered when the cell went back to the low current densities with high CEs. The energy density and power density of the full cell were further evaluated with a Ragone plot, which were calculated based on the total mass of the cathode and anode active materisals, as shown in Figure 5-37d. These values show a clear comparison with commercial lithim-ion batteries and electochemical capacitors. Such cell could provide much higher power densities than commercial Li-ion batteries, while the energy densities are several times bigger than that of electrochemical capacitors. These capabilities suggest that Sb nanorod arrays anodes can be used to build large energy storage and conversion devices with both high-power and high-energy densities.
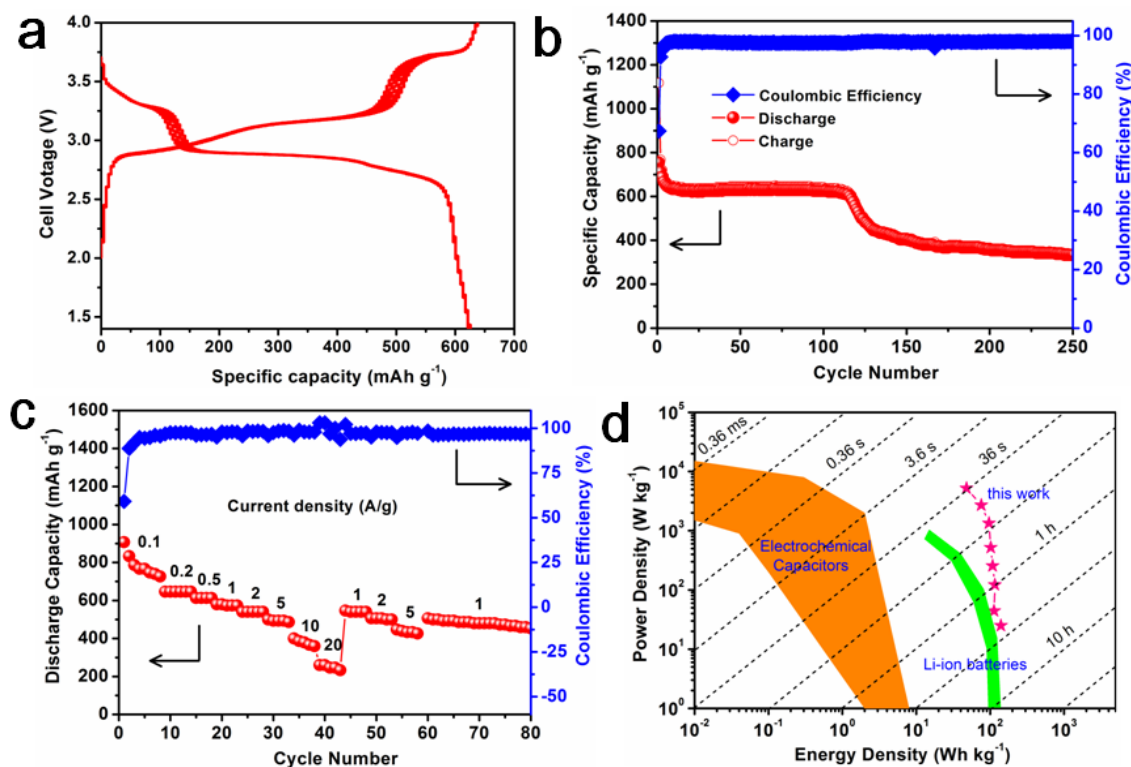
Figure 5-37 Electrochemical performance of a full cell coupled by P2-Na$_{2/3}$Ni$_{1/3}$Mn$_{2/3}$O$_2$ cathode and Sb nanorod arrays anode. (a) Galvanostatic charge/discharge voltage profiles of five cycles, and (b) Cycling performance at a current density of 0.5 A g^{-1} (relative to the anode weight). (c) Rate Capability (with respect to the anode weight), and (d) Ragone plot of energy and power density (with respect to the total mass of anode and cathode) at various current densities from 0.1 to 20 A g^{-1}. The shaded curves were obtained from reported work[265].

5.4.3 Full-cell performance of hierarchical Sb-Ni nanoarrays

The feasibility of the 3D Sb-Ni nanoarrays for Na-ion storage in practice was studied. A full cell was measured by consisting 3D Sb-Ni nanoarrays as negative electrodes and P2-Na$_{2/3}$Ni$_{1/3}$Mn$_{2/3}$O$_2$ as positive electrodes. This full cell was tested in a potential window of 1.4-4.0 V. Figure 5-38a displays CVs of the full cell at a scan rate of 0.5 mV s^{-1}. The cathodic and anodic peaks at 3.4 and 3.7 V correspond to the insertion/extraction into/from P2-Na$_{2/3}$Ni$_{1/3}$Mn$_{2/3}$O$_2$. Another two pairs of peaks at 2.8/3.2 V and 2.77/3.0 V are attributed to the sodiation of Sb and the disodiation of Na$_3$Sb. The multiple redox reactions are also reflected on the charge/ dicharge voltage profile of the full cell (Figure 5-38a inset), which match well with the CV results. The excellent reproducibility of CV curves indicates the

good stability of electrode materials again. Figure 5-38b reveals the cycling performance of the full cell, in which it delivers a highly stable capacity over 200 cycles at a current density of 0.5 A g^{-1}. After 200 charge/discharge cycles, it retains a reversible capacity of 579.8 mAh g^{-1} (relative to Sb anode weight), which is 87.8% of the theoretical capacity of Sb (660 mAh g^{-1}). In addition, except the first activation cycles, the cell gives high CEs approaching 98%. The energy density is estimated to be about 100 Wh kg^{-1} (based on the total mass of the positive and negative active materials), which is considered to be an extremely promising value. Furthermore, the full cell also shows a high rate capability, as seen in Figure 5-38c. It can be cycled at very large rates of 10 and 20 A g^{-1}, and keep stable reversibility, showing the capacities of 526.3 and 434.2 mAh g^{-1}, respectively, in the second set. They correspond to charge time of 3 min 23 s and 1 min 40 s (Figure 5-38d), respectively, which are sufficient for high-rate applications.[234] After 75 cycles at various current densities from 0.2 to 20 A g^{-1}, these capacities can still be recovered when the cell went back to the low current density, delivering 539.5 mAh g^{-1} at 0.5 A g^{-1}. Although the current density greatly increases (100 times), the discharge voltage only drops by about 0.16 V, indicating the small polarization and good reaction kinetics in full cell (Figure 5-38d). The results also clearly show that the full cell can be fully charged or discharged within a very short period of a few hundreds of seconds. The electrochemical performance of the current P2-Na$_{2/3}$Ni$_{1/3}$Mn$_{2/3}$O$_2$//3D Sb-Ni nanoarrays Na-ion full battery is superior to recently reported Na$_3$V$_2$(PO$_4$)$_3$-C//Sb@TiO$_2$,[44] Na$_{2/3}$Ni$_{1/3}$Mn$_{2/3}$O$_2$//rGO/Sb$_2$S$_3$,[234] and Na$_{0.4}$Mn$_{0.54}$Co$_{0.46}$O$_2$//NiSb full batteries.[45] The reported results were never carried out at rates as high as those obtained in our work.
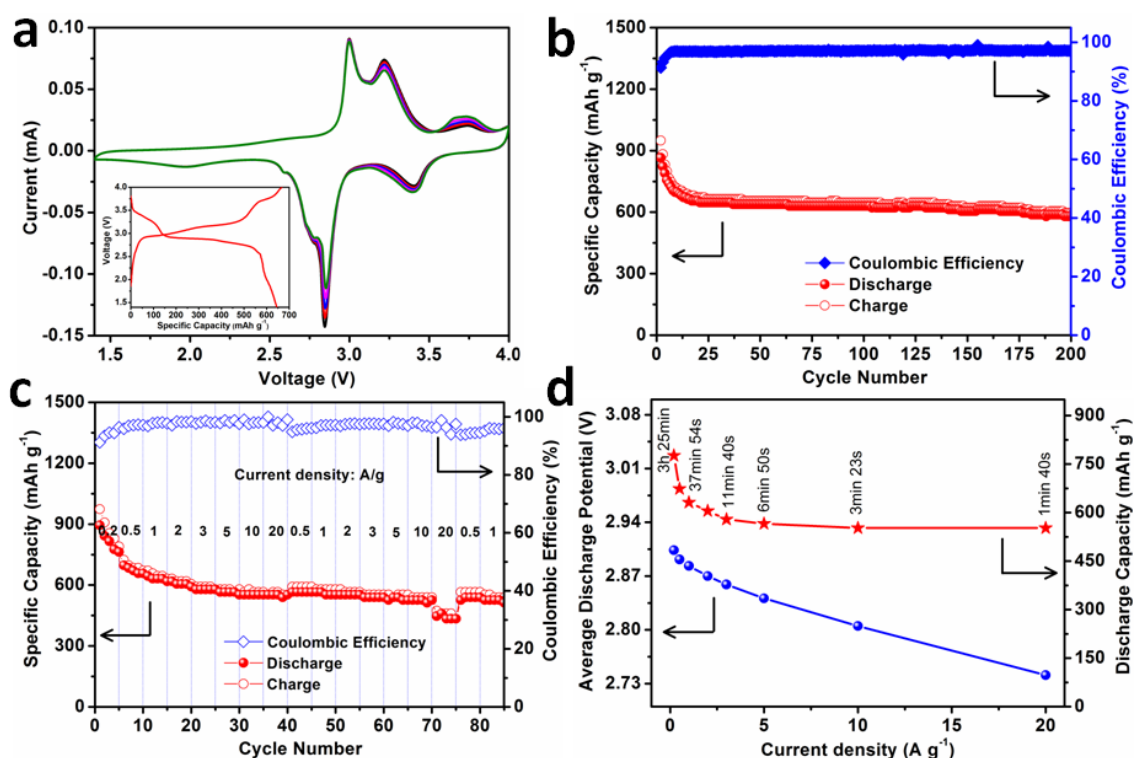
Figure 5-38 Electrochemical performance of a full cell coupled by P2-Na$_{2/3}$Ni$_{1/3}$Mn$_{2/3}$O$_2$ cathodes and 3D Sb-Ni nanoarrays anodes. (a) CV curves at a scan rate of 0.5 mV s^{-1} and galvanostatic charge/discharge voltage profile (inset) at a current density of 0.5 A g^{-1}. (b) Cycling performance at a current density of 0.5 A g^{-1} (relative to the anode weight) (starting from the 2nd cycle). (c) Rate capability (with respect to the anode weight) at various current densities from 0.1 to 20 A g^{-1}. (d) Respective discharge capacity and average discharge working potential at various current densities.

6   Summary and outlook

In summary, three different electrode configurations are demonstrated to accommodate the large volume changes of Sb for further realizing the good cycability and high rate capability. The main contributions of this dissertation can be concluded in the following aspects:

(1) Hierarchical Sb was successfully fabricated *via* a very simple and cost-effective electrochemical deposition method. Morphological and structural characterizations show that the as-prepared Sb has a uniform fern leaf-like structure which is composed of well-crystallized Sb nanoparticles. The formation mechanism of the fern leaf-like Sb was also investigated. The hierarchical Sb exhibits desirable properties for sodium storage, such as high electrical conductivity and large surface area. When used as additive-free anode for Na-ion batteries, the as-obtained fern leaf-like Sb reveals excellent cycling stability and rate capability. It can afford a high reversible capacity of 589 mAh g^{-1} over 150 cycles at 0.5 A g^{-1} and retain a capacity of 498 mAh g^{-1} at a high rate of 10 A g^{-1}. Furthermore, a full cell constructed by P2-Na$_{2/3}$Ni$_{1/3}$Mn$_{2/3}$O$_2$//fern leaf-like Sb also displays remarkably stable and robust Na-storage performance, which includes a high capacity retention of 70 % after 100 cycles at 0.5 A g^{-1} and a large capacity of 370 mAh g^{-1} at 10 A g^{-1}. The excellent electrochemical performance of fern leaf-like Sb can be attributed to its morphological and structural features that ensure the fast ion and electron transport and stable electrode structure.

(2) A performance-oriented electrode structure is proposed, which is 1D nanostructure arrays with large-scale high ordering, well vertical alignment, and large interval spacing. Benefiting from these structure merits, a great enhancement on electrochemical performance could be achieved. To Sb as an example, we firstly report large-scale highly ordered Sb nanorod arrays with uniform large interval spacing (190 nm). In return for this electrode design, high ion accessibility, fast electron transport, and strong electrode integrity are presented here. Used as additive- and binder-free anode for Na-ion batteries, Sb nanorod arrays showed a high capacity of 620 mAh g^{-1} at the 100th cycle with a retention of 84% up to 250 cycles at 0.2 A g^{-1}, and superior rate capability for delivering reversible capacities of 579.7 and 557.7 mAh g^{-1} at 10 and 20 A g^{-1}, respectively. A full cell coupled by P2-Na$_{2/3}$Ni$_{1/3}$Mn$_{2/3}$O$_2$ cathode and Sb nanorod arrays anode was also conducted, which showed a good cycle performance up to 250 cycles, high rate capability up to 20 A g^{-1}, and large energy density up to 130 Wh kg^{-1}. We believe that this

architecture design may be exploited for other active materials to achieve a high-capacity, high-rate, and long-lifespan electrode for Na-ion batteries.

(3) A novel hierarchical electrode composed of Sb nanoplates on Ni nanorod arrays is proposed to tackle the issues of the rapidly fading capacity and poor rate capability of Sb materials for Na-ion batteries. In serving as an anode material for SIB, the Ni core works as a support for relieving the volume expansion and constraction of Sb, while also providing an efficeint electron pathway for the fast alloying/dealloying of Sb. Meanwhile, the Sb shell acts a host for Na storage. The cooperation of the two components in D Sb-Ni nanoarrays brings about a favorable synergistic effect of the 2D nanoplates, open conductive array structure, and strong structural integrity, leading to excellent Na-ion storage performance. When used as binder-free SIB anode, it exhibits high capacity retention of 80% over 200 cycles at a high current density of 0.5 A g^{-1}, and excellent rate capacity up to 20 A g^{-1} with the capacity of 580 mAh g^{-1}. Kinetics analysis reveals an interesting Na^+ intercalation pseudocapacitive behaviour in 3D Sb-Ni nanoarrays Na cell and a high contribution of capacitive charge. This pseudocapacitve behaviour is highly beneficial to fast charge storage and long-term cyclability. Moreover, a P2-$Na_{2/3}Ni_{1/3}Mn_{2/3}O_2$//3D Sb-Ni nanoarrays full cell delivers a highly reversible capacity of 579.8 mAh g^{-1} over 200 cycles and a high energy density of 100 Wh kg^{-1}. This design strategy provides a new concept and applicable way to design other electrode materials with fast and stable Na-ion storage.

We believe that the above three different electrode architectures may work in other electrode materials for fast and stable Na-ion storage and their obtained excellent performance of Na-ion full cells proves the feasibility of these Sb structures as additive-free anodes in practice. Our findings will open up new opportunities for developing electrode materials of SIBs and hold great promise for the development of long-life SIBs for next-generation large-scale energy storage applications.

7 Bibliography

1. M. Armand and J.-M. Tarascon, *Nature*, 2008, 451, 652-657.

2. J. B. Goodenough and Y. Kim, *Chemistry of Materials*, 2009, 22, 587-603.

3. M. R. Palacin, *Chemical Society Reviews*, 2009, 38, 2565-2575.

4. V. Palomares, P. Serras, I. Villaluenga, K. B. Hueso, J. Carretero-González and T. Rojo, *Energy & Environmental Science*, 2012, 5, 5884-5901.

5. S. P. Ong, V. L. Chevrier, G. Hautier, A. Jain, C. Moore, S. Kim, X. Ma and G. Ceder, *Energy & Environmental Science*, 2011, 4, 3680-3688.

6. S. Y. Hong, Y. Kim, Y. Park, A. Choi, N.-S. Choi and K. T. Lee, *Energy & Environmental Science*, 2013, 6, 2067-2081.

7. N. Yabuuchi, K. Kubota, M. Dahbi and S. Komaba, *Chemical Reviews*, 2014, 114, 11636-11682.

8. Y. Cao, L. Xiao, W. Wang, D. Choi, Z. Nie, J. Yu, L. V. Saraf, Z. Yang and J. Liu, *Advanced Materials*, 2011, 23, 3155-3160.

9. N. Yabuuchi, M. Kajiyama, J. Iwatate, H. Nishikawa, S. Hitomi, R. Okuyama, R. Usui, Y. Yamada and S. Komaba, *Nature materials*, 2012, 11, 512-517.

10. A. Abouimrane, W. Weng, H. Eltayeb, Y. Cui, J. Niklas, O. Poluektov and K. Amine, *Energy & Environmental Science*, 2012, 5, 9632-9638.

11. S. Tepavcevic, H. Xiong, V. R. Stamenkovic, X. Zuo, M. Balasubramanian, V. B. Prakapenka, C. S. Johnson and T. Rajh, *ACS nano*, 2011, 6, 530-538.

12. J. Qian, M. Zhou, Y. Cao, X. Ai and H. Yang, *Advanced Energy Materials*, 2012, 2, 410-414.

13. Z. Jian, W. Han, X. Lu, H. Yang, Y. S. Hu, J. Zhou, Z. Zhou, J. Li, W. Chen and D. Chen, *Advanced Energy Materials*, 2013, 3, 156-160.

14. Y.-U. Park, D.-H. Seo, H.-S. Kwon, B. Kim, J. Kim, H. Kim, I. Kim, H.-I. Yoo and K. Kang, *Journal of the American Chemical Society*, 2013, 135, 13870-13878.

15. D. Kim, E. Lee, M. Slater, W. Lu, S. Rood and C. S. Johnson, *Electrochemistry Communications*, 2012, 18, 66-69.

16. L. Wang, Y. Lu, J. Liu, M. Xu, J. Cheng, D. Zhang and J. B. Goodenough, *Angewandte Chemie International Edition*, 2013, 52, 1964-1967.

17. H. Yoshida, N. Yabuuchi, K. Kubota, I. Ikeuchi, A. Garsuch, M. Schulz-Dobrick and S. Komaba, *Chemical Communications*, 2014, 50, 3677-3680.

18. Z. Wang, L. Qie, L. Yuan, W. Zhang, X. Hu and Y. Huang, *Carbon*, 2013, 55, 328-334.

19. Y. Cao, L. Xiao, M. L. Sushko, W. Wang, B. Schwenzer, J. Xiao, Z. Nie, L. V. Saraf, Z. Yang and J. Liu, *Nano Letters*, 2012, 12, 3783-3787.

20. D. Stevens and J. Dahn, *Journal of the Electrochemical Society*, 2000, 147, 1271-1273.

21. A. Ponrouch, A. Goñi and M. R. Palacín, *Electrochemistry Communications*, 2013, 27, 85-88.

22. K. Tang, L. Fu, R. J. White, L. Yu, M. M. Titirici, M. Antonietti and J. Maier, *Advanced Energy Materials*, 2012, 2, 873-877.

23. J. Zhao, L. Zhao, K. Chihara, S. Okada, J.-i. Yamaki, S. Matsumoto, S. Kuze and K. Nakane, *Journal of Power Sources*, 2013, 244, 752-757.

24. S. Wenzel, T. Hara, J. Janek and P. Adelhelm, *Energy & Environmental Science*, 2011, 4, 3342-3345.

25. S. Komaba, W. Murata, T. Ishikawa, N. Yabuuchi, T. Ozeki, T. Nakayama, A. Ogata, K. Gotoh and K. Fujiwara, *Advanced Functional Materials*, 2011, 21, 3859-3867.

26. K.-T. Kim, G. Ali, K. Y. Chung, C. S. Yoon, H. Yashiro, Y.-K. Sun, J. Lu, K. Amine and S.-T. Myung, *Nano Letters*, 2014, 14, 416-422.

27. Y. Xu, E. M. Lotfabad, H. Wang, B. Farbod, Z. Xu, A. Kohandehghan and D. Mitlin, *Chemical Communications*, 2013, 49, 8973-8975.

28. H. Xiong, M. D. Slater, M. Balasubramanian, C. S. Johnson and T. Rajh, *The Journal of Physical Chemistry Letters*, 2011, 2, 2560-2565.

29. P. Senguttuvan, G. Rousse, V. Seznec, J.-M. Tarascon and M. R. Palacin, *Chemistry of Materials*, 2011, 23, 4109-4111.

30. C. Wu, P. Kopold, Y.-L. Ding, P. A. van Aken, J. Maier and Y. Yu, *ACS Nano*, 2015, 9, 6610-6618.

31. G. Jeong, Y.-U. Kim, H. Kim, Y.-J. Kim and H.-J. Sohn, *Energy & Environmental Science*, 2011, 4, 1986-2002.

32. M. D. Slater, D. Kim, E. Lee and C. S. Johnson, *Advanced Functional Materials*, 2013, 23, 947-958.

33. V. Chevrier and G. Ceder, *Journal of the Electrochemical Society*, 2011, 158, A1011-A1014.

34. J. Qian, Y. Chen, L. Wu, Y. Cao, X. Ai and H. Yang, *Chemical Communications*, 2012, 48, 7070-7072.

35. N. Li, S. Liao, Y. Sun, H. Song and C. Wang, *Journal of Materials Chemistry A*, 2015, 3, 5820-5828.

36. L. Xiao, Y. Cao, J. Xiao, W. Wang, L. Kovarik, Z. Nie and J. Liu, *Chemical Communications*, 2012, 48, 3321-3323.

37. M. Walter, S. Doswald and M. V. Kovalenko, *Journal of Materials Chemistry A*, 2016, 4, 7053-7059.

38. N. Zhang, Y. Liu, Y. Lu, X. Han, F. Cheng and J. Chen, *Nano Research*, 2015, 8, 3384-3393.

39. M. He, K. Kravchyk, M. Walter and M. V. Kovalenko, *Nano Letters*, 2014, 14, 1255-1262.

40. Y. N. Ko and Y. C. Kang, *Chemical Communications*, 2014, 50, 12322-12324.

41. C. Nithya and S. Gopukumar, *Journal of Materials Chemistry A*, 2014, 2, 10516-10525.

42. W. Zhang, Y. Liu, C. Chen, Z. Li, Y. Huang and X. Hu, *Small*, 2015, 11, 3822-3829.

43. X. Zhou, Z. Dai, J. Bao and Y.-G. Guo, *Journal of Materials Chemistry A*, 2013, 1, 13727-13731.

44. N. Wang, Z. Bai, Y. Qian and J. Yang, *Advanced Materials*, 2016.

45. J. Liu, Z. Yang, J. Wang, L. Gu, J. Maier and Y. Yu, *Nano Energy*, 2015, 16, 389-398.

46. H. Hou, X. Cao, Y. Yang, L. Fang, C. Pan, X. Yang, W. Song and X. Ji, *Chemical Communications*, 2014, 50, 8201-8203.

47. A. Darwiche, M. T. Sougrati, B. Fraisse, L. Stievano and L. Monconduit, *Electrochemistry Communications*, 2013, 32, 18-21.

48. J. Duan, W. Zhang, C. Wu, Q. Fan, W. Zhang, X. Hu and Y. Huang, *Nano Energy*, 2015, 16, 479-487.

49. D.-H. Nam, K.-S. Hong, S.-J. Lim and H.-S. Kwon, *Journal of Power Sources*, 2014, 247, 423-427.

50. L. Baggetto, K. J. Carroll, H.-Y. Hah, C. E. Johnson, D. R. Mullins, R. R. Unocic, J. A. Johnson, Y. S. Meng and G. M. Veith, *The Journal of Physical Chemistry C*, 2014, 118, 7856-7864.

51. Y. Idota, T. Kubota, A. Matsufuji, Y. Maekawa and T. Miyasaka, *Science*, 1997, 276, 1395-1397.

52. D. H. Nam, K. S. Hong, S. J. Lim, M. J. Kim and H. S. Kwon, *Small*, 2015, 11, 2885-2892.

53. L. Li, K. H. Seng, D. Li, Y. Xia, H. K. Liu and Z. Guo, *Nano Research*, 2014, 7, 1466-1476.

54. H. Hou, Y. Yang, Y. Zhu, M. Jing, C. Pan, L. Fang, W. Song, X. Yang and X. Ji, *Electrochimica Acta*, 2014, 146, 328-334.

55. Y. Zhu, P. Nie, L. Shen, S. Dong, Q. Sheng, H. Li, H. Luo and X. Zhang, *Nanoscale*, 2015, 7, 3309-3315.

56. L. Wu, F. Pei, R. Mao, F. Wu, Y. Wu, J. Qian, Y. Cao, X. Ai and H. Yang, *Electrochimica Acta*, 2013, 87, 41-45.

57. X. Li, J. Yang, Y. Hu, J. Wang, Y. Li, M. Cai, R. Li and X. Sun, *Journal of Materials Chemistry*, 2012, 22, 18847-18853.

58. B. L. Ellis, P. Knauth and T. Djenizian, *Advanced Materials*, 2014, 26, 3368-3397.

59. H. Pan, Y.-S. Hu and L. Chen, *Energy & Environmental Science*, 2013, 6, 2338-2360.

60. B. Dunn, H. Kamath and J.-M. Tarascon, *Science*, 2011, 334, 928-935.

61. L. Joerissen, J. Garche, C. Fabjan and G. Tomazic, *Journal of Power Sources*, 2004, 127, 98-104.

62. H. Ibrahim, A. Ilinca and J. Perron, *Renewable and Sustainable Energy Reviews*, 2008, 12, 1221-1250.

63. Z. Yang, J. Zhang, M. C. Kintner-Meyer, X. Lu, D. Choi, J. P. Lemmon and J. Liu, *Chemical Reviews*, 2011, 111, 3577-3613.

64. C.-X. Zu and H. Li, *Energy & Environmental Science*, 2011, 4, 2614-2624.

65. B. L. Ellis and L. F. Nazar, *Current Opinion in Solid State and Materials Science*, 2012, 16, 168-177.

66. S. W. Kim, D. H. Seo, X. Ma, G. Ceder and K. Kang, *Advanced Energy Materials*, 2012, 2, 710-721.

67. Y. Xu, M. Zhou and Y. Lei, *Advanced Energy Materials*, 2016, 6, 1502514.

68. M. H. Han, E. Gonzalo, G. Singh and T. Rojo, *Energy & Environmental Science*, 2015, 8, 81-102.

69. M. Okoshi, Y. Yamada, A. Yamada and H. Nakai, *Journal of the Electrochemical Society*, 2013, 160, A2160-A2165.

70. C. Delmas, J.-J. Braconnier, C. Fouassier and P. Hagenmuller, *Solid State Ionics*, 1981, 3, 165-169.

71. K. Kuratani, N. Uemura, H. Senoh, H. Takeshita and T. Kiyobayashi, *Journal of Power Sources*, 2013, 223, 175-182.

72. Y. Yamada, Y. Koyama, T. Abe and Z. Ogumi, *The Journal of Physical Chemistry C*, 2009, 113, 8948-8953.

73. Y. Yamada, Y. Iriyama, T. Abe and Z. Ogumi, *Langmuir*, 2009, 25, 12766-12770.

74. M. Sawicki and L. L. Shaw, *RSC Advances*, 2015, 5, 53129-53154.

75. M. Spahr, P. Novak, O. Haas and R. Nesper, *Journal of Power Sources*, 1995, 54, 346-351.

76. N. Yabuuchi and S. Komaba, *Science and Technology of Advanced Materials*, 2014, 15, 043501.

77. S. Komaba, C. Takei, T. Nakayama, A. Ogata and N. Yabuuchi, *Electrochemistry Communications*, 2010, 12, 355-358.

78. J. Braconnier, C. Delmas and P. Hagenmuller, *Materials Research Bulletin*, 1982, 17, 993-1000.

79. C. Delmas, C. Fouassier and P. Hagenmuller, *Physica B+ C*, 1980, 99, 81-85.

80. N. Yabuuchi, H. Yoshida and S. Komaba, *Electrochemistry*, 2012, 80, 716-719.

81. Y. Uebou, S. Okada and J.-i. Yamaki, *Journal of Power Sources*, 2003, 115, 119-124.

82. A. NADIRI, C. Delmas, R. Salmon and P. Hagenmuller, *Revue de chimie minérale*, 1984, 21, 537-544.

83. M. Nose, S. Shiotani, H. Nakayama, K. Nobuhara, S. Nakanishi and H. Iba, *Electrochemistry Communications*, 2013, 34, 266-269.

84. H. Kim, I. Park, D.-H. Seo, S. Lee, S.-W. Kim, W. J. Kwon, Y.-U. Park, C. S. Kim, S. Jeon and K. Kang, *Journal of the American Chemical Society*, 2012, 134, 10369-10372.

85. J. Kang, S. Baek, V. Mathew, J. Gim, J. Song, H. Park, E. Chae, A. K. Rai and J. Kim, *Journal of Materials Chemistry*, 2012, 22, 20857-20860.

86. P. Serras, V. Palomares, A. Goñi, I. G. de Muro, P. Kubiak, L. Lezama and T. Rojo, *Journal of Materials Chemistry*, 2012, 22, 22301-22308.

87. R. Shakoor, D.-H. Seo, H. Kim, Y.-U. Park, J. Kim, S.-W. Kim, H. Gwon, S. Lee and K. Kang, *Journal of Materials Chemistry*, 2012, 22, 20535-20541.

88. M. Xu, L. Wang, X. Zhao, J. Song, H. Xie, Y. Lu and J. B. Goodenough, *Physical Chemistry Chemical Physics*, 2013, 15, 13032-13037.

89. V. Palomares, M. Casas-Cabanas, E. Castillo-Martínez, M. H. Han and T. Rojo, *Energy & Environmental Science*, 2013, 6, 2312-2337.

90. Z. Lu and J. Dahn, *Journal of the Electrochemical Society*, 2001, 148, A1225-A1229.

91. D. H. Lee, J. Xu and Y. S. Meng, *Physical Chemistry Chemical Physics*, 2013, 15, 3304-3312.

92. Z. Lu and J. Dahn, *Chemistry of Materials*, 2001, 13, 1252-1257.

93. A. Yamada, S.-C. Chung and K. Hinokuma, *Journal of the Electrochemical Society*, 2001, 148, A224-A229.

94. B. L. Cushing and J. B. Goodenough, *Journal of Solid State Chemistry*, 2001, 162, 176-181.

95. J. Gopalakrishnan and K. K. Rangan, *Chemistry of Materials*, 1992, 4, 745-747.

96. A. Padhi, K. Nanjundaswamy, C. Masquelier and J. Goodenough, *Journal of the Electrochemical Society*, 1997, 144, 2581-2586.

97. Z. Jian, L. Zhao, H. Pan, Y.-S. Hu, H. Li, W. Chen and L. Chen, *Electrochemistry Communications*, 2012, 14, 86-89.

98. S. Y. Lim, H. Kim, R. Shakoor, Y. Jung and J. W. Choi, *Journal of the Electrochemical Society*, 2012, 159, A1393-A1397.

99. D. Wang, X. Wu, Z. Wang and L. Chen, *Journal of Power Sources*, 2005, 140, 125-128.

100. J. Sangster, *Journal of Phase Equilibria and Diffusion*, 2007, 28, 571-579.

101. H. g. Wang, Z. Wu, F. l. Meng, D. l. Ma, X. l. Huang, L. m. Wang and X. b. Zhang, *ChemSusChem*, 2013, 6, 56-60.

102. L. Wu, D. Buchholz, D. Bresser, L. G. Chagas and S. Passerini, *Journal of Power Sources*, 2014, 251, 379-385.

103. L. Baggetto, J. K. Keum, J. F. Browning and G. M. Veith, *Electrochemistry Communications*, 2013, 34, 41-44.

104. Y. Kim, Y. Park, A. Choi, N. S. Choi, J. Kim, J. Lee, J. H. Ryu, S. M. Oh and K. T. Lee, *Advanced Materials*, 2013, 25, 3045-3049.

105. J. W. Wang, X. H. Liu, S. X. Mao and J. Y. Huang, *Nano Letters*, 2012, 12, 5897-5902.

106. L. Wu, X. Hu, J. Qian, F. Pei, F. Wu, R. Mao, X. Ai, H. Yang and Y. Cao, *Journal of Materials Chemistry A*, 2013, 1, 7181-7184.

107. S. C. Jung, D. S. Jung, J. W. Choi and Y.-K. Han, *The Journal of Physical Chemistry Letters*, 2014, 5, 1283-1288.

108. N. Yabuuchi, Y. Matsuura, T. Ishikawa, S. Kuze, J. Y. Son, Y. T. Cui, H. Oji and S. Komaba, *ChemElectroChem*, 2014, 1, 580-589.

109. A. Suryawanshi, D. Mhamane, S. Nagane, S. Patil, V. Aravindan, S. Ogale and M. Srinivasan, *Electrochimica Acta*, 2014, 146, 218-223.

110. L. Zhao, J. Zhao, Y. S. Hu, H. Li, Z. Zhou, M. Armand and L. Chen, *Advanced Energy Materials*, 2012, 2, 962-965.

111. Y. Park, D. S. Shin, S. H. Woo, N. S. Choi, K. H. Shin, S. M. Oh, K. T. Lee and S. Y. Hong, *Advanced Materials*, 2012, 24, 3562-3567.

112. K. Chihara, N. Chujo, A. Kitajou and S. Okada, *Electrochimica Acta*, 2013, 110, 240-246.

113. X. Rui, W. Sun, C. Wu, Y. Yu and Q. Yan, *Advanced Materials*, 2015, 27, 6670-6676.

114. S. Guo, H. Yu, P. Liu, Y. Ren, T. Zhang, M. Chen, M. Ishida and H. Zhou, *Energy & Environmental Science*, 2015, 8, 1237-1244.

115. X. Xie, K. Kretschmer, J. Zhang, B. Sun, D. Su and G. Wang, *Nano Energy*, 2015, 13, 208-217.

116. H. Li, L. Peng, Y. Zhu, D. Chen, X. Zhang and G. Yu, *Energy & Environmental Science*, 2016, 9, 3399-3405.

117. J. Waluk, H. P. Klein, A. J. Ashe and J. Michl, *Organometallics*, 1989, 8, 2804-2808.

118. T. Asami, M. Kubota and K. Minamisawa, *Japanese Journal of Soil Science and Plant Nutrition (Japan)*, 1988.

119. J. T. Tanner and W. D. Ehmann, *Geochimica et Cosmochimica Acta*, 1967, 31, 2007-2026.

120. P. W. Bridgman, 1925.

121. M. Obrovac and V. Chevrier, *Chemical Reviews*, 2014, 114, 11444-11502.

122. A. Darwiche, C. Marino, M. T. Sougrati, B. Fraisse, L. Stievano and L. Monconduit, *Journal of the American Chemical Society*, 2012, 134, 20805-20811.

123. F. Wan, J.-Z. Guo, X.-H. Zhang, J.-P. Zhang, H.-Z. Sun, Q. Yan, D.-X. Han, L. Niu and X.-L. Wu, *ACS Applied Materials & Interfaces*, 2016, 8, 7790-7799.

124. Z. Liu, X.-Y. Yu, X. W. D. Lou and U. Paik, *Energy & Environmental Science*, 2016, 9, 2314-2318.

125. S. Liu, J. Feng, X. Bian, J. Liu and H. Xu, *Energy & Environmental Science*, 2016, 9, 1229-1236.

126. F. Zhao, N. Han, W. Huang, J. Li, H. Ye, F. Chen and Y. Li, *Journal of Materials Chemistry A*, 2015, 3, 21754-21759.

127. M. H. Ryou, J. Kim, I. Lee, S. Kim, Y. K. Jeong, S. Hong, J. H. Ryu, T. S. Kim, J. K. Park and H. Lee, *Advanced Materials*, 2013, 25, 1571-1576.

128. I. Lahiri, S.-W. Oh, J. Y. Hwang, S. Cho, Y.-K. Sun, R. Banerjee and W. Choi, *ACS Nano*, 2010, 4, 3440-3446.

129. S. Komaba, T. Ishikawa, N. Yabuuchi, W. Murata, A. Ito and Y. Ohsawa, *ACS Applied Materials & Interfaces*, 2011, 3, 4165-4168.

130. X. Zhou, Y. Zhong, M. Yang, M. Hu, J. Wei and Z. Zhou, *Chemical Communications*, 2014, 50, 12888-12891.

131. W. Luo, S. Lorger, B. Wang, C. Bommier and X. Ji, *Chemical Communications*, 2014, 50, 5435-5437.

132. L. Wu, X. Hu, J. Qian, F. Pei, F. Wu, R. Mao, X. Ai, H. Yang and Y. Cao, *Energy & Environmental Science*, 2014, 7, 323-328.

133. J. Zhu, T. Sun, J. Chen, W. Shi, X. Zhang, X. Lou, S. Mhaisalkar, H. H. Hng, F. Boey and J. Ma, *Chemistry of Materials*, 2010, 22, 5333-5339.

134. J. Xie, X. Zhao, G. Cao, M. Zhao and S. Su, *Journal of Power Sources*, 2005, 140, 350-354.

135. A. Nie, L. y. Gan, Y. Cheng, X. Tao, Y. Yuan, S. Sharifi‑Asl, K. He, H. Asayesh‑Ardakani, V. Vasiraju and J. Lu, *Advanced Functional Materials*, 2016, 26, 543-552.

136. S. Liao, Y. Sun, J. Wang, H. Cui and C. Wang, *Electrochimica Acta*, 2016, 211, 11-17.

137. J.-H. Choi, C.-W. Ha, H.-Y. Choi, H.-C. Shin and S.-M. Lee, *Materials Letters*, 2015, 159, 349-352.

138. L. Baggetto, E. Allcorn, R. R. Unocic, A. Manthiram and G. M. Veith, *Journal of Materials Chemistry A*, 2013, 1, 11163-11169.

139. A. Darwiche, M. Toiron, M. T. Sougrati, B. Fraisse, L. Stievano and L. Monconduit, *Journal of Power Sources*, 2015, 280, 588-592.

140. L. Baggetto, H.-Y. Hah, C. E. Johnson, C. A. Bridges, J. A. Johnson and G. M. Veith, *Physical Chemistry Chemical Physics*, 2014, 16, 9538-9545.

141. Y. Zhao and A. Manthiram, *Chemistry of Materials*, 2015, 27, 3096-3101.

142. H. Hou, M. Jing, Y. Yang, Y. Zhang, Y. Zhu, W. Song, X. Yang and X. Ji, *Journal of Materials Chemistry A*, 2015, 3, 2971-2977.

143. M. He, M. Walter, K. V. Kravchyk, R. Erni, R. Widmer and M. V. Kovalenko, *Nanoscale*, 2015, 7, 455-459.

144. L. Fan, J. Zhang, J. Cui, Y. Zhu, J. Liang, L. Wang and Y. Qian, *Journal of Materials Chemistry A*, 2015, 3, 3276-3280.

145. H. Hou, M. Jing, Y. Zhang, J. Chen, Z. Huang and X. Ji, *Journal of Materials Chemistry A*, 2015, 3, 17549-17552.

146. L. Wu, H. Lu, L. Xiao, X. Ai, H. Yang and Y. Cao, *Journal of Materials Chemistry A*, 2015, 3, 5708-5713.

147. L. Mai, L. Xu, C. Han, X. Xu, Y. Luo, S. Zhao and Y. Zhao, *Nano Letters*, 2010, 10, 4750-4755.

148. H.-Y. Chen, D.-B. Kuang and C.-Y. Su, *Journal of Materials Chemistry*, 2012, 22, 15475-15489.

149. R. Lakes, *Nature*, 1993, 361, 511-515.

150. L. Zhang, H. B. Wu, Y. Yan, X. Wang and X. W. D. Lou, *Energy & Environmental Science*, 2014, 7, 3302-3306.

151. Y. Sun, X. Hu, C. Y. Jimmy, Q. Li, W. Luo, L. Yuan, W. Zhang and Y. Huang, *Energy & Environmental Science*, 2011, 4, 2870-2877.

152. N. Wu, Y. Zhang, Y. Wei, H. Liu and H. Wu, *ACS Applied Materials & Interfaces*, 2016, 8, 25361-25368.

153. Q. Mahmood, M. G. Kim, S. Yun, S.-M. Bak, X.-Q. Yang, H. S. Shin, W. S. Kim, P. V. Braun and H. S. Park, *Nano Letters*, 2015, 15, 2269-2277.

154. J. Duay, S. A. Sherrill, Z. Gui, E. Gillette and S. B. Lee, *ACS nano*, 2013, 7, 1200-1214.

155. H. B. Wu, H. Pang and X. W. D. Lou, *Energy & Environmental Science*, 2013, 6, 3619-3626.

156. Y. Wu, C. Cao, J. Zhang, L. Wang, X. Ma and X. Xu, *ACS Applied Materials & Interfaces*, 2016, 8, 19567-19572.

157. K. X. Wang, X. H. Li and J. S. Chen, *Advanced Materials*, 2015, 27, 527-545.

158. Y. Wu, Z. Wen, H. Feng and J. Li, *Small*, 2012, 8, 858-862.

159. H. Uchiyama, E. Hosono, H. Zhou and H. Imai, *Journal of Materials Chemistry*, 2009, 19, 4012-4016.

160. C. Ban, Z. Wu, D. T. Gillaspie, L. Chen, Y. Yan, J. L. Blackburn and A. C. Dillon, *Advanced Materials*, 2010, 22.

161. S. Wang, L. Xia, L. Yu, L. Zhang, H. Wang and X. W. D. Lou, *Advanced Energy Materials*, 2015.

162. L. Zhan, S. Wang, L.-X. Ding, Z. Li and H. Wang, *Journal of Materials Chemistry A*, 2015, 3, 19711-19717.

163. W.-Q. Wu, H.-L. Feng, H.-S. Rao, Y.-F. Xu, D.-B. Kuang and C.-Y. Su, *Nature Communications*, 2014, 5.

164. P. Banerjee, I. Perez, L. Henn-Lecordier, S. B. Lee and G. W. Rubloff, *Nature Nanotechnology*, 2009, 4, 292-296.

165. S. W. Boettcher, J. M. Spurgeon, M. C. Putnam, E. L. Warren, D. B. Turner-Evans, M. D. Kelzenberg, J. R. Maiolo, H. A. Atwater and N. S. Lewis, *Science*, 2010, 327, 185-187.

166. Z. L. Wang and J. Song, *Science*, 2006, 312, 242-246.

167. J. Liu, K. Song, P. A. van Aken, J. Maier and Y. Yu, *Nano Letters*, 2014, 14, 2597-2603.

168. J. Liu, Y. Li, X. Huang, R. Ding, Y. Hu, J. Jiang and L. Liao, *Journal of Materials Chemistry*, 2009, 19, 1859-1864.

169. H. Masuda and K. Fukuda, *Science*, 1995, 268, 1466.

170. W. Lee and S.-J. Park, *Chemical Reviews*, 2014, 114, 7487-7556.

171. Y. Lei, W. Cai and G. Wilde, *Progress in Materials Science*, 2007, 52, 465-539.

172. H. Zhao, M. Zhou, L. Wen and Y. Lei, *Nano Energy*, 2015, 13, 790-813.

173. Y. Lei, C. Liang, Y. Wu, L. Zhang and Y. Mao, *Journal of Vacuum Science & Technology B: Microelectronics and Nanometer Structures Processing, Measurement, and Phenomena*, 2001, 19, 1109-1114.

174. Y. Lei, W.-K. Chim, Z. Zhang, T. Zhou, L. Zhang, G. Meng and F. Phillipp, *Chemical Physics Letters*, 2003, 380, 313-318.

175. H. Zhao, C. Wang, R. Vellacheri, M. Zhou, Y. Xu, Q. Fu, M. Wu, F. Grote and Y. Lei, *Advanced Materials*, 2014, 26, 7654-7659.

176. F. Grote, R.-S. Kühnel, A. Balducci and Y. Lei, *Applied Physics Letters*, 2014, 104, 053904.

177. C. Wang, L. Wen, T. Kups, Y. Mi, R. Vellacheri, Y. Fang, P. Schaaf, H. Zhao and Y. Lei, *Journal of Materials Chemistry C*, 2013, 1, 8003-8006.

178. A. Al-Haddad, Z. Wang, R. Xu, H. Qi, R. Vellacheri, U. Kaiser and Y. Lei, *The Journal of Physical Chemistry C*, 2015, 119, 16331-16337.

179. H. Masuda, K. Yasui and K. Nishio, *Advanced Materials*, 2000, 12, 1031-1033.

180. K. H. Tsui, Q. Lin, H. Chou, Q. Zhang, H. Fu, P. Qi and Z. Fan, *Advanced Materials*, 2014, 26, 2805-2811.

181. N. Winkler, J. Leuthold, Y. Lei and G. Wilde, *Journal of Materials Chemistry*, 2012, 22, 16627-16632.

182. C.-H. Cui, H.-H. Li and S.-H. Yu, *Chemical Communications*, 2010, 46, 940-942.

183. X. Zhang, L. Zhang, Y. Lei, L. Zhao and Y. Mao, *Journal of Materials Chemistry*, 2001, 11, 1732-1734.

184. T. D. Lazzara, M. A. Whitehead and T. G. van de Ven, *European Polymer Journal*, 2009, 45, 1883-1890.

185. M. Steinhart, J. Wendorff, A. Greiner, R. Wehrspohn, K. Nielsch, J. Schilling, J. Choi and U. Gösele, *Science*, 2002, 296, 1997-1997.

186. T.-C. Wang, H.-Y. Hsueh and R.-M. Ho, *Chemistry of Materials*, 2010, 22, 4642-4651.

187. S. Park, Y.-S. Kim, W. B. Kim and S. Jon, *Nano Letters*, 2009, 9, 1325-1329.

188. G. Che, B. B. Lakshmi, E. R. Fisher and C. R. Martin, *Nature*, 1998, 393, 346-349.

189. H. Nishihara and T. Kyotani, *Advanced Materials*, 2012, 24, 4473-4498.

190. C. Liang, K. Terabe, T. Tsuruoka, M. Osada, T. Hasegawa and M. Aono, *Advanced Functional Materials*, 2007, 17, 1466-1472.

191. Y. Lei, L. Zhang, G. Meng, G. Li, X. Zhang, C. Liang, W. Chen and S. Wang, *Applied Physics Letters*, 2001, 78, 1125-1127.

192. B. B. Lakshmi, C. J. Patrissi and C. R. Martin, *Chemistry of Materials*, 1997, 9, 2544-2550.

193. R. O. Al-Kaysi, A. M. Müller, R. J. Frisbee and C. J. Bardeen, *Crystal Growth and Design*, 2009, 9, 1780-1785.

194. H. X. Ji, J. S. Hu, Q. X. Tang, W. P. Hu, W. G. Song and L. J. Wan, *Advanced Materials*, 2006, 18, 2753-2757.

195. Z. Zhan, R. Xu, Y. Mi, H. Zhao and Y. Lei, *ACS Nano*, 2015, 9, 4583-4590.

196. Z. Zhan and Y. Lei, *ACS Nano*, 2014, 8, 3862-3868.

197. Y. Qiu, S.-F. Leung, Q. Zhang, B. Hua, Q. Lin, Z. Wei, K.-H. Tsui, Y. Zhang, S. Yang and Z. Fan, *Nano Letters*, 2014, 14, 2123-2129.

198. Q. Lin, B. Hua, S.-f. Leung, X. Duan and Z. Fan, *ACS Nano*, 2013, 7, 2725-2732.

199. Y. Liu, W. Zhang, Y. Zhu, Y. Luo, Y. Xu, A. Brown, J. N. Culver, C. A. Lundgren, K. Xu and Y. Wang, *Nano Letters*, 2012, 13, 293-300.

200. F. F. Cao, J. W. Deng, S. Xin, H. X. Ji, O. G. Schmidt, L. J. Wan and Y. G. Guo, *Advanced Materials*, 2011, 23, 4415-4420.

201. M. M. Shaijumon, E. Perre, B. Daffos, P. L. Taberna, J. M. Tarascon and P. Simon, *Advanced Materials*, 2010, 22, 4978-4981.

202. S. K. Cheah, E. Perre, M. Rooth, M. Fondell, A. Hårsta, L. Nyholm, M. Boman, T. r. Gustafsson, J. Lu and P. Simon, *Nano Letters*, 2009, 9, 3230-3233.

203. P.-L. Taberna, S. Mitra, P. Poizot, P. Simon and J.-M. Tarascon, *Nature materials*, 2006, 5, 567-573.

204. Y. Liu, Y. Xu, Y. Zhu, J. N. Culver, C. A. Lundgren, K. Xu and C. Wang, *ACS Nano*, 2013, 7, 3627-3634.

205. Y. Xu, M. Zhou, L. Wen, C. Wang, H. Zhao, Y. Mi, L. Liang, Q. Fu, M. Wu and Y. Lei, *Chemistry of Materials*, 2015, 27, 4274-4280.

206. P. Patel, I.-S. Kim and P. Kumta, *Materials Science and Engineering: B*, 2005, 116, 347-352.

207. G.-H. Lee, H.-W. Shim and D.-W. Kim, *Nano Energy*, 2015, 13, 218-225.

208. W. D. Sproul, *Surface and Coatings Technology*, 1996, 81, 1-7.

209. D. M. Mattox, *Handbook of physical vapor deposition (PVD) processing*, William Andrew, 2010.

210. R. M. Penner, *The Journal of Physical Chemistry C*, 2014, 118, 17179-17192.

211. W. Coene, G. Janssen, M. O. de Beeck and D. Van Dyck, *Physical Review Letters*, 1992, 69, 3743.

212. H. Seiler, *Journal of Applied Physics*, 1983, 54, R1-R18.

213. S. L. Flegler, J. W. Heckman and K. L. Klomparens, *Scanning and transmission electron microscopy: an introduction*, WH Freeman New York:, 1993.

214. R. S. White and A. D. Owens, *Journal of Forensic Science*, 1987, 32, 1595-1603.

215. G. Thomas, 1962.

216. D. B. Williams and C. B. Carter, in *Transmission electron microscopy*, Springer, 1996, pp. 3-17.

217. M. Xu, F. Wang, B. Ding, X. Song and J. Fang, *RSC Advances*, 2012, 2, 2240-2243.

218. G. Zhang, S. Sun, M. N. Banis, R. Li, M. Cai and X. Sun, *Crystal Growth & Design*, 2011, 11, 2493-2499.

219. M. H. Rashid and T. K. Mandal, *The Journal of Physical Chemistry C*, 2007, 111, 16750-16760.

220. B. Yang, Y. Wu, H. Hu, C. Li, X. Yang and Y. Qian, *Materials Chemistry and Physics*, 2005, 92, 286-289.

221. C. He, S. Wu, N. Zhao, C. Shi, E. Liu and J. Li, *ACS Nano*, 2013, 7, 4459-4469.

222. Y. Zhu, X. Han, Y. Xu, Y. Liu, S. Zheng, K. Xu, L. Hu and C. Wang, *ACS Nano*, 2013, 7, 6378-6386.

223. C. W. Lee, J.-C. Kim, S. Park, H. J. Song and D.-W. Kim, *Nano Energy*, 2015, 15, 479-489.

224. S. H. Choi and Y. C. Kang, *ChemSusChem*, 2013, 6, 2111-2116.

225. S. Yang, H. Song and X. Chen, *Electrochemistry Communications*, 2006, 8, 137-142.

226. Y. N. Ko, S. B. Park, K. Y. Jung and Y. C. Kang, *Nano Letters*, 2013, 13, 5462-5466.

227. J. Song, Z. Yu, M. L. Gordin, S. Hu, R. Yi, D. Tang, T. Walter, M. Regula, D. Choi and X. Li, *Nano Letters*, 2014, 14, 6329-6335.

228. X. Jia, Y. Cheng, Y. Lu and F. Wei, *ACS Nano*, 2014, 8, 9265-9273.

229. L. Ji, M. Gu, Y. Shao, X. Li, M. H. Engelhard, B. W. Arey, W. Wang, Z. Nie, J. Xiao and C. Wang, *Advanced Materials*, 2014, 26, 2901-2908.

230. Y. Li, B. Tan and Y. Wu, *Nano Letters*, 2008, 8, 265-270.

231. J. Jiang, Y. Li, J. Liu and X. Huang, *Nanoscale*, 2011, 3, 45-58.

232. A. L. M. Reddy, M. M. Shaijumon, S. R. Gowda and P. M. Ajayan, *Nano Letters*, 2009, 9, 1002-1006.

233. L. Wen, Y. Mi, C. Wang, Y. Fang, F. Grote, H. Zhao, M. Zhou and Y. Lei, *Small*, 2014, 10, 3162-3168.

234. Y. Denis, P. V. Prikhodchenko, C. W. Mason, S. K. Batabyal, J. Gun, S. Sladkevich, A. G. Medvedev and O. Lev, *Nature Communications*, 2013, 4.

235. B. Farbod, K. Cui, W. P. Kalisvaart, M. Kupsta, B. Zahiri, A. Kohandehghan, E. M. Lotfabad, Z. Li, E. J. Luber and D. Mitlin, *ACS Nano*, 2014, 8, 4415-4429.

236. X. Jia, Z. Chen, X. Cui, Y. Peng, X. Wang, G. Wang, F. Wei and Y. Lu, *ACS Nano*, 2012, 6, 9911-9919.

237. B. Luo, B. Wang, X. Li, Y. Jia, M. Liang and L. Zhi, *Advanced Materials*, 2012, 24, 3538-3543.

238. J. M. Mosby and A. L. Prieto, *Journal of the American Chemical Society*, 2008, 130, 10656-10661.

239. I. Kovalenko, B. Zdyrko, A. Magasinski, B. Hertzberg, Z. Milicev, R. Burtovyy, I. Luzinov and G. Yushin, *Science*, 2011, 334, 75-79.

240. A. Magasinski, P. Dixon, B. Hertzberg, A. Kvit, J. Ayala and G. Yushin, *Nature Materials*, 2010, 9, 353-358.

241. J. Huang, K. Wang and Z. Wei, *Journal of Materials Chemistry*, 2010, 20, 1117-1121.

242. C.-H. Lai, K.-W. Huang, J.-H. Cheng, C.-Y. Lee, B.-J. Hwang and L.-J. Chen, *Journal of Materials Chemistry*, 2010, 20, 6638-6645.

243. X. Song, X. Li, Z. Bai, B. Yan, D. Li and X. Sun, *Nano Energy*, 2016, 26, 533-540.

244. D. Chao, C. Zhu, P. Yang, X. Xia, J. Liu, J. Wang, X. Fan, S. V. Savilov, J. Lin and H. J. Fan, *Nature Communications*, 2016, 7.

245. H. Hou, M. Jing, Y. Yang, Y. Zhu, L. Fang, W. Song, C. Pan, X. Yang and X. Ji, *ACS Applied Materials & Interfaces*, 2014, 6, 16189-16196.

246. J. Wang, N. Du, H. Zhang, J. Yu and D. Yang, *The Journal of Physical Chemistry C*, 2011, 115, 23620-23624.

247. F.-S. Ke, L. Huang, B. C. Solomon, G.-Z. Wei, L.-J. Xue, B. Zhang, J.-T. Li, X.-D. Zhou and S.-G. Sun, *Journal of Materials Chemistry*, 2012, 22, 17511-17517.

248. J. Wang, N. Du, H. Zhang, J. Yu and D. Yang, *Journal of Materials Chemistry*, 2012, 22, 1511-1515.

249. M. Fan, Y. Chen, Y. Xie, T. Yang, X. Shen, N. Xu, H. Yu and C. Yan, *Advanced Functional Materials*, 2016, 26, 5019-5027.

250. A. B. Fuertes, F. Pico and J. M. Rojo, *Journal of Power Sources*, 2004, 133, 329-336.

251. L. Baggetto, P. Ganesh, C.-N. Sun, R. A. Meisner, T. A. Zawodzinski and G. M. Veith, *Journal of Materials Chemistry A*, 2013, 1, 7985-7994.

252. L. Hu, X. Zhu, Y. Du, Y. Li, X. Zhou and J. Bao, *Chemistry of Materials*, 2015, 27, 8138-8145.

253. L. Liang, Y. Xu, C. Wang, L. Wen, Y. Fang, Y. Mi, M. Zhou, H. Zhao and Y. Lei, *Energy & Environmental Science*, 2015, 8, 2954-2962.

254. K. Zhang, Z. Hu, X. Liu, Z. Tao and J. Chen, *Advanced Materials*, 2015, 27, 3305-3309.

255. S. Ardizzone, G. Fregonara and S. Trasatti, *Electrochimica Acta*, 1990, 35, 263-267.

256. J. Y. Shin, D. Samuelis and J. Maier, *Advanced Functional Materials*, 2011, 21, 3464-3472.

257. J. Jamnik and J. Maier, *Physical Chemistry Chemical Physics*, 2003, 5, 5215-5220.

258. Y. F. Zhukovskii, P. Balaya, E. A. Kotomin and J. Maier, *Physical Review Letters*, 2006, 96, 058302.

259. Y. Yang, X. Fan, G. Casillas, Z. Peng, G. Ruan, G. Wang, M. J. Yacaman and J. M. Tour, *ACS Nano*, 2014, 8, 3939-3946.

260. Y. F. Zhukovskii, P. Balaya, M. Dolle, E. A. Kotomin and J. Maier, *Physical Review B*, 2007, 76, 235414.

261. X. Yu, J. Sun, K. Tang, H. Li, X. Huang, L. Dupont and J. Maier, *Physical Chemistry Chemical Physics*, 2009, 11, 9497-9503.

262. Y. F. Zhukovskii, E. Kotomin, P. Balaya and J. Maier, *Solid State Sciences*, 2008, 10, 491-495.

263. Y. Wen, B. Wang, G. Zeng, K. Nogita, D. Ye and L. Wang, *Chemistry–An Asian Journal*, 2015, 10, 661-666.

264. I. Hasa, S. Passerini and J. Hassoun, *RSC Advances*, 2015, 5, 48928-48934.

265. P. Simon and Y. Gogotsi, *Nature Materials*, 2008, 7, 845-854.

Extended works

During the period of my Ph.D., besides the works presented in this dissertation, I have not only focused on Sb nanomaterials, but also have been interested in reduced graphene oxide, carbon fibers, composite nanostructures, ALD, and hydrothermal synthesis. I also published two more papers as the first author and proficiently collaborated with my colleagues in other topics related to batteries. The abstracts and the table of content figures of the respective papers are illustrated in this section to highlight the achieved results beyong the scope of this dissertation.

1. **1-Dimensional AgVO₃ nanowires hybrid with 2-dimensional graphene nanosheets to create 3-dimensional composite aerogels and their improved electrochemical properties (the first author)**
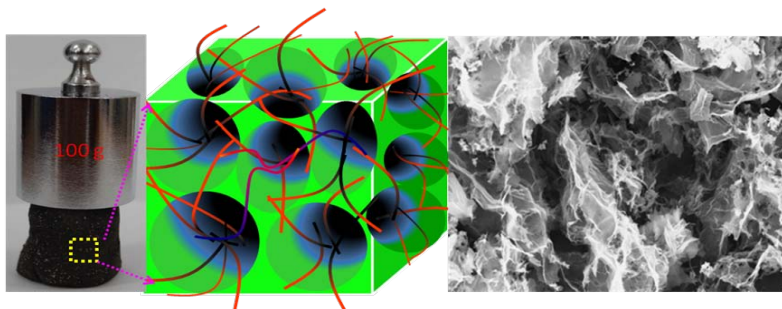
Three-dimensional (3D) porous composite aerogels have been synthesized *via* an innovative *in situ* hydrothermal method assisted by a freeze-drying process. In this hybrid structure, one-dimensional (1D) $AgVO_3$ nanowires are uniformly dispersed on two-dimensional (2D) graphene nanosheet surfaces and/or are penetrated through the graphene sheets, forming 3D porous composite aerogels. As cathode materials for lithium-ion batteries, the composite aerogels exhibit high discharge capacity, excellent rate capability, and good cycling stability. (*Nanoscale*, 2014, **6**, 3536-3539)

2. **Intertwined Cu₃V₂O₇(OH)₂·2H₂O nanowires/carbon fibers composite: a new anode with high rate capability for sodium-ion batteries (the first author)**
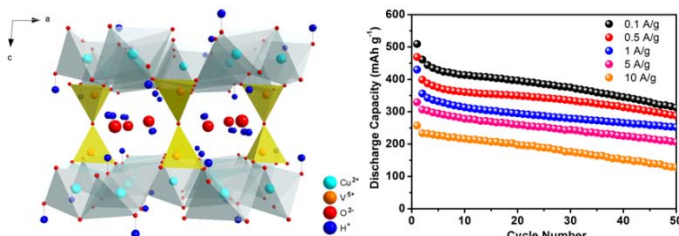

Sodium-ion batteries (SIBs) have recently attracted intensive attentions as a potential alternative to LIBs for large-scale energy storage applications. However, one of the major challenges to the commercialization of SIBs is the limited choice of anode materials that can offer high rate capability. In this regard, we report intertwined $Cu_3V_2O_7(OH)_2 \cdot 2H_2O$ nanowires/carbon fibers composite, fabricated by a facile

hydrothermal method, as the anode material for SIBs. It shows s a highly reversible Na-ion storage capacity of 287.4 mAh g^{-1} after 50 cycles at a large current density of 0.5 A g^{-1}, and excellent rate performance of delivering 206.5 and 127.7 mAh g^{-1} after 50 cycles at high current densities of 5 and 10 A g^{-1}, respectively. The promising performance is ascribed to both the crystal structure of $Cu_3V_2O_7(OH)_2 \cdot 2H_2O$ with a large interlayer spacing, and unique intertwined network morphology of CuVOH-NWs/CFs composite in which CuVOH-NWs and CFs synergistically functioned. This work will pave a way to develop more metal vanadates materials as anodes for high-performance SIBs. (*J. Power Sources*, 2015, **294**, 193-200)

3. **Manipulation of disodium rhodizonate: factors for fast-charge and fast-discharge sodium-ion batteries with long-term cyclability (in cooperation with Dr. Chengliang Wang)**
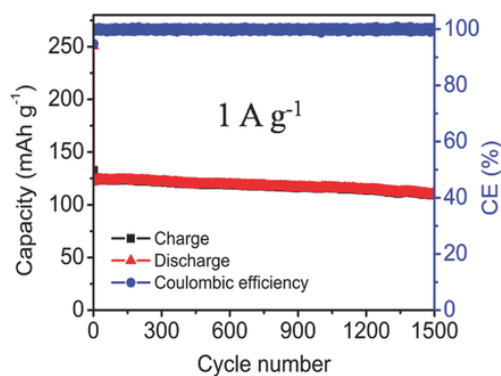
Organic sodium-ion batteries (SIBs) are one of the most promising alternatives of current commercial inorganic lithium-ion batteries (LIBs) especially in the foreseeable large-scale flexible and wearable electronics. However, only a few reports are involving organic SIBs so far. To achieve fast-charge and fast-discharge performance and the long-term cycling suitable for practical applications, is still challenging. Here, important factors for high performance SIBs especially with high capacity and long-term cyclability under fast-charge and fast-discharge process are investigated. It is found that controlling the solubility through molecular design and determination of the electrochemical window is essential to eliminate dissolution of the electrode material, resulting in improved cyclability. The results show that poly(vinylidenedifluoride) will decompose during the charge/discharge process, indicating the significance of the binder for achieving high cyclability. Beside of these, it is also shown that decent charge transport and ionic diffusion are beneficial to the fast-charge and fast-discharge batteries. For instance, the flake morphology facilitates the ionic diffusion and thereby can lead to a capacitive effect that is favorable to fast charge and fast discharge. (*Adv. Funct. Mater.*, 2016, **26**, 1777-1786)

4. Potassium prussian blue nanoparticles: a low-cost cathode material for potassium-ion batteries (in cooperation with Dr. Yang Xu)
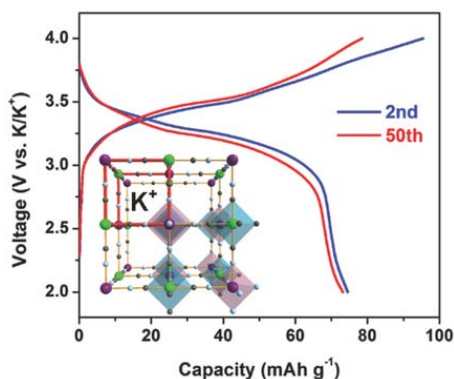
Potassium-ion batteries (KIBs) in organic electrolytes hold great promise as an electrochemical energy storage technology owing to the abundance of potassium, close redox potential to lithium, and similar electrochemistry with lithium system. Although carbon materials have been studied as KIB anodes, investigations on KIB cathodes have been scarcely reported. A comprehensive study on potassium Prussian blue $K_{0.220}Fe[Fe(CN)_6]_{0.805}\cdot4.01H_2O$ nanoparticles as a potential cathode material is for the first time reported. The cathode exhibits a high discharge voltage of 3.1–3.4 V, a high reversible capacity of 73.2 mAh g^{-1}, and great cyclability at both low and high rates with a very small capacity decay rate 0.09% per cycle. Electrochemical reaction mechanism analysis identifies the carbon-coordinated Fe^{III}/Fe^{II} couple as redox-active site and proves structural stability of the cathode during charge/discharge. Furthermore, for the first time, a KIB full-cell is presented by coupling the nanoparticles with commercial carbon materials. The full-cell delivers a capacity of 68.5 mAh g^{-1} at 100 mA g^{-1} and retains 93.4% of the capacity after 50 cycles. Considering the low cost and material sustainability as well as the great electrochemical performances, this work may pave the way toward more studies on KIB cathodes and trigger future attention on rechargeable KIBs. (*Adv. Funct. Mater.*, 2016, **27**, 1604307)

5. Understanding the orderliness of atomic arrangement toward enhanced sodium storage (in cooperation with Dr. Min Zhou)
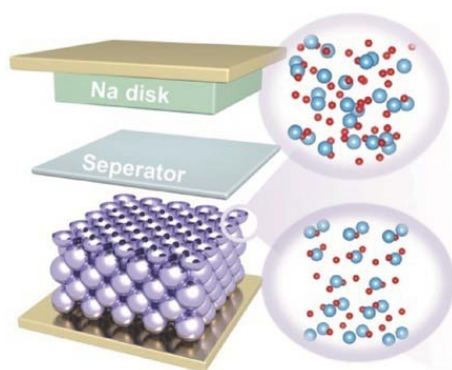
In response to the increased demands of available energy storage, sodium ion batteries (SIBs) appear as promising alternatives to widely used lithium ion batteries. However, because of large radius of Na ions, more complex requirements for the intrinsic properties raise the difficulties in finding a suitable material, in particularly for electrodes with intercalation mechanism. Concerning the principle of designing effective electrodes, the ordering of atomic arrangements should be at the heart in SIBs due to its significant

influences on various electrochemical processes, such as ion absorption, ion diffusion, electron diffusion, etc. As proof-of-concept, the state-of-the art TiO_2 electrodes with different orderliness of atomic arrangement are achieved through colloidal crystal template method assisted by low-temperature atomic layer deposition and post-heating treatment. The disordering at the surface is benefit for the contribution from surface processes, which is particularly significant to the electrode materials with poorer affinity of transporting ions. Meanwhile, the disordering in bulk results in better ion diffusion, but worse electron transport. Understanding this relationship between atomic orderliness and battery performance is of importance for extending the design principle to some traditional electrodes for highly effective energy storage. (*Adv. Energy Mater.*, 2016, **6**, 1600448)

6. **A selectively permeable membrane for enhancing cyclability of organic sodium-ion batteries (in cooperation with Dr. Chengliang Wang)**
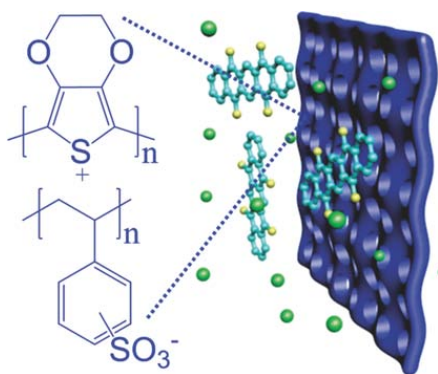
A novel strategy to enhance the cyclability of organic sodium-ion batteries is developed by applying a selectively permeable membrane to allow the passage of Na ions but block the slightly dissolved active molecules and thereby inhibit the further dissolution. After utilization of the membrane, the batteries show highly enhanced cyclability. Such strategy can be potentially extended to many organic materials with low solubilities. (*Adv. Mater.*, 2016, **28**, 9182-9187)

7. **Enhancement of sodium ion battery performance enabled by oxygen vacancies (in cooperation with Dr. Yang Xu)**
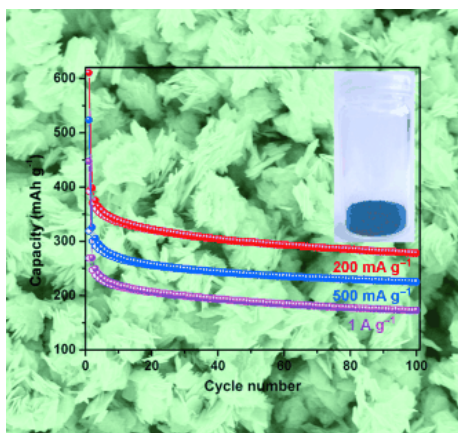
The utilization of oxygen vacancies (OVs) in sodium ion batteries (SIBs) is expected to enhance performance, but as yet it has rarely been reported. Taking the MoO_{3-x} nanosheet anode as an example, for the first time we demonstrate the benefits of OVs on SIB performance. Moreover, the benefits at deep-discharge conditions can be further promoted by an ultrathin Al_2O_3 coating. A series of measurements show that the OVs increase the electric conductivity and Na-ion diffusion coefficient, and the promotion from ultrathin coating lies in the effective reduction of cycling-induced

solid-electrolyte interphase. The coated nanosheets exhibited high reversible capacity and great rate capability with the capacities of 283.9 (50 mA g^{-1}) and 179.3 mAh g^{-1}(1 A g^{-1}) after 100 cycles. This work may not only arouse future attention on OVs for sodium energy storage, but also open up new possibilities for designing strategies to utilize defects in other energy storage systems. (*Angew. Chem.*, 2015, **54**, 8768-8771)

8. Extended π-conjugated system for fast-charge and -discharge sodium-ion batteries (in cooperation with Dr. Chengliang Wang)
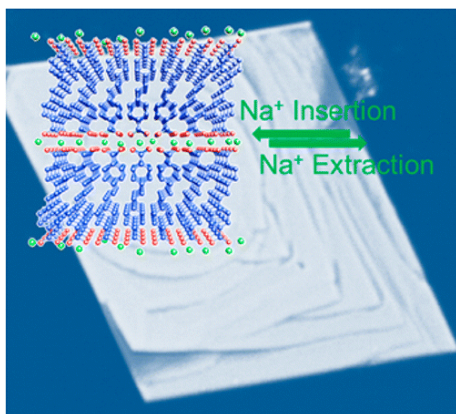
Organic sodium-ion batteries (SIBs) are potential alternatives of current commercial inorganic lithium-ion batteries for portable electronics (especially wearable electronics) because of their low cost and flexibility, making them possible to meet the future flexible and large-scale requirements. However, only a few organic SIBs have been reported so far, and most of them either were tested in a very slow rate or suffered significant performance degradation when cycled under high rate. Here, we are focusing on the molecular design for improving the battery performance and addressing the current challenge of fast-charge and -discharge. Through reasonable molecular design strategy, we demonstrate that the extension of the π-conjugated system is an efficient way to improve the high rate performance, leading to much enhanced capacity and cyclability with full recovery even after cycled under current density as high as 10 A g^{-1}. (*J. Am. Chem. Soc.*, 2015, **137**, 3124-3130)

9. Amorphous TiO$_2$ inverse opal anode for high-rate sodium ion batteries (in cooperation with Dr. Min Zhou)
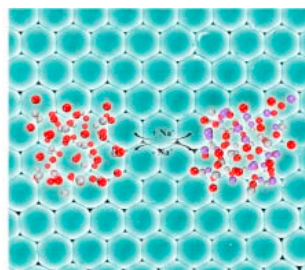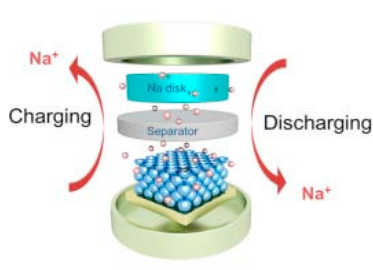

Potential applications of sodium-ion batteries (SIBs) have motivated significant research interest in grid-scale energy storage. However, large radius of Na ions results in different electrochemical behaves. Therefore, synergistic understanding of the differences is greatly interested for future development of SIBs. Surface availability for ions with poor affinity to electrode materials is critical to rate performance in SIBs, but yet has rarely been reported. Here, to overcome the obstacles of material platform, amorphous TiO$_2$inverse

opal is employed as a proof-of-concept prototype to illuminate the effects of surface ion availability and its relationship between solvent wettability and rate capability. Within expectation, superior rate capabilities are achieved in return for enhanced solvent wettability, regardless of the type of electrolyte and the ion concentration in electrolyte. Even when the anode is cycled at a current density as high as 5000 mA g^{-1}, the reversible capacity could still retain a high value of ~113 mA h g^{-1}. Our concept opens up a promising avenue to realize full potential of designing electrode materials for SIBs by adjusting the surface kinetics. This understanding shall extend the design principle to electrode materials for highly effective energy storage using other transport ions and other storage mechanisms. (*Nano Energy*, 2017, **31**, 514-524)

10. Highly ordered three-dimensional Ni-TiO₂ nanoarrays as sodium ion battery anodes (in cooperation with Dr. Yang Xu)
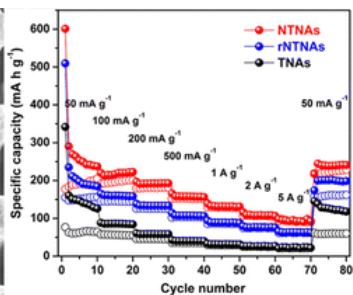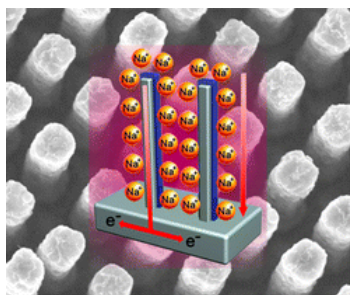
Sodium ion batteries (SIBs) represent an effective energy storage technology with potentially lower material costs than lithium ion batteries. Here, we show that the electrochemical performance of SIBs, especially rate capability, is intimately connected to the electrode design at the nanoscale by taking anatase TiO_2 as an example. Highly ordered three-dimensional (3D) Ni-TiO_2 core–shell nanoarrays were fabricated using nanoimprinted AAO templating technique and directly used as anode. The nanoarrays delivered a reversible capacity of ~200 mAh g^{-1} after 100 cycles at the current density of 50 mAh g^{-1} and were able to retain a capacity of ~95 mAh g^{-1} at the current density as high as 5 A g^{-1} and fully recover low rate capacity. High ion accessibility, fast electron transport, and excellent electrode integrity were shown as great merits to obtain the presented electrochemical performance. Our work demonstrates the possibility of highly ordered 3D heterostructured nanoarrays as a promising electrode design for Na energy storage to alleviate the reliance on the materials' intrinsic nature and provides a versatile and cost-effective technique for the fabrication of such perfectly ordered nanostructures. (*Chem. Mater.*, 2015, **27**, 4274-4280)

Scientific contributions

In total I have published and jointly published 13 papers in SCI-indexed international scientific journals during the period of my Ph.D., including 1 paper with impact factor higher than 25 (Energy & Environmental Science), 10 papers with impact factor higher than 8 (Advanced Materials, Advanced Functional Materials, Advanced Energy Materials, Journal of the American Chemical Society, Nano Energy, Chemistry of Materials, Angewandte Chemie International Edition, Journal of Material Chemistry A, Nano Research), and 2 papers with impact factor between 6 and 8 (Nanoscale, Journal of Power Sources). The published papers were cited for more than 206 times during my PhD (Source: google scholar database).

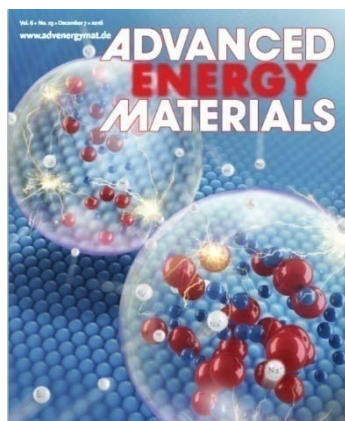I also gave 17 contributions at conferences, including 10 talks and 7 posters.

Cover stories
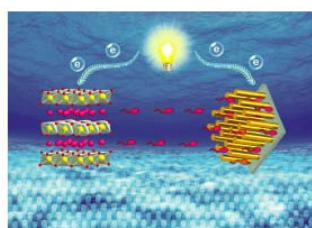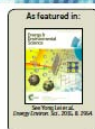
1. The paper 'Large-scale highly ordered Sb nanorod array anodes with high capacity and rate capability for sodium-ion batteries' by L. Liang and Y. Lei was selected as back inside cover.

2. The paper 'Understanding the orderliness of atomic arrangement towards enhanced sodium storage' by M. Zhou, L. Liang and Y. Lei was selected as back cover.
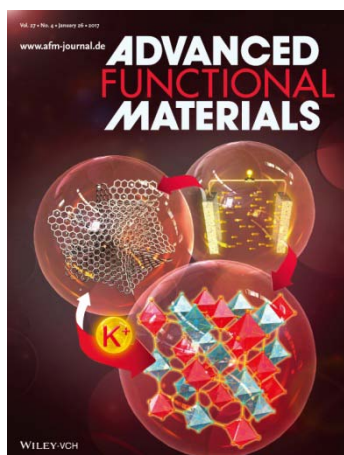
3. The paper 'Potassium prussian blue nanoparticles: a low-cost cathode material for potassium-ion batteries' by C. Zhang, Y. Xu, L. Liang and Y. Lei was selected as back cover.

Publications in SCI-indexed scientific journals

1. **L. Liang**, Y. Xu, L.Wen, Y. Li, M. Zhou, C. Wang, H. Zhao, U. Kaiser, Y. Lei*, *Nano Res.*, 2017, Accepted. (IF: 7.354)

2. **L. Liang**, Y. Xu, Y. Li, H. Dong, M. Zhou, H. Zhao, U. Kaiser, Y. Lei*, *J. Mater. Chem. A*, 2017, **5**, 1749-1755. (IF: 8.867)

3. M. Zhou, Y. Xu, C. Wang, Q. Li, J. Xiang, **L. Liang**, H. Zhao, M. Wu, Y. Lei*, *Nano Energy*, 2017, 31, 514-524. (IF: 12.343)

4. C. Zhang, Y. Xu, M. Zhou, **L. Liang**, H. Dong, M. Wu, Y. Yang, Y. Lei*, *Adv. Funct. Mater.*, 2016, **27**, 1604307. (IF: 12.124)

5. C. Wang, C. Jiang, Y. Xu, **L. Liang**, M. Zhou, J. Jiang, S. Singh, H. Zhao, A. Schober, Y. Lei*, *Adv. Mater.*, 2016, **28**, 9182-9187. (IF: 19.791)

6. C. Wang, Y. Fang, Y. Xu, **L. Liang**, M. Zhou, H. Zhao, Y. Lei*, *Adv. Funct. Mater.*, 2016, **26**, 1777-1786. (IF: 12.124)

7. M. Zhou, Y. Xu, J. Xiang, C. Wang, **L. Liang**, L. Wen, Y. Fang, Y. Mi, Y. Lei*, *Adv. Energy Mater.*, 2016, **6**, 1600448. (IF: 15.230)

8. **L. Liang**, Y. Xu, C. Wang, L. Wen, Y. Fang, Y. Mi, M. Zhou, H. Zhao, Y. Lei*, *Energy Environ. Sci.*, 2015, **8**, 2954-2962. (IF: 29.518, selected as back inside cover)

9. **L. Liang**, Y. Xu, X. Wang, C. Wang, M. Zhou, Q. Fu, M. Wu, Y. Lei*, *J. Power Sources*, 2015, **294**, 193-200. (IF: 6.395)

10. Y. Xu, Z. M., X. Wang, C. Wang, **L. Liang**, F. Grote, M. Wu, Y. Lei*, *Angew. Chem.*, 2015, **54**, 8768-8771. (IF: 11.994)

11. C. Wang, Y. Xu, Y. Fang, M. Zhou, **L. Liang**, S. Singh, H. Zhao, A. Schober, Y. Lei*, *J. Am. Chem. Soc.*, 2015, **137**, 3124-3130. (IF: 13.858)

12. Y. Xu, M. Zhou, L. Wen, C. Wang, H. Zhao, Y. Mi, **L. Liang**, Q. Fu, M. Wu, Y. Lei*, *Chem. Mater.*, 2015, **27**, 4274-4280. (IF: 9.466)

13. **L. Liang**, Y. Xu, Y. Lei*, H. Liu*, *Nanoscale*, 2014, **6**, 3536-3539. (IF: 7.367)

Conference contributions

1. **L. Liang**, Y. Xu, C. Wang, L. Wen, Y. Fang, Y. Mi, M. Zhou, H. Zhao, Y. Lei*, 'Large-scale highly ordered Sb nanorod arrays anode with high capacity and rate capability for sodium-ion batteries', the 80th Annual Conference of the DPG, Mar 19-24, 2017, Dresden, Germany. **(Talk)**

2. **L. Liang**, Y. Xu, C. Wang, M. Zhou, L. Wen, H. Zhao, Y. Fang, Y. Mi, Y. Lei*, 'Highly ordered 3D nanostructure arrays with improved electrochemical performance for sodium-ion battery anodes', the 80th Annual Conference of the DPG, Mar 19-24, 2017, Dresden, Germany. **(Poster)**

3. B. Hai, Y. Xu, M. Zhou, **L. Liang**, Y. Lei*, 'Synthesis of bismuth/reduced graphene oxide composites and their electrochemical properties for Na-ion batteries', the 80th Annual Conference of the DPG, Mar 19-24, 2017, Dresden, Germany. **(Talk)**

4. M. Zhou, Y. Xu, **L. Liang**, B. Hai, Y. Lei*, 'Template-directed nanoengineering for promoted solar water splitting', the 80th Annual Conference of the DPG, Mar 19-24, 2017, Dresden, Germany. **(Poster)**

5. Y. Xu, Y. Xu, M. Zhou, **L. Liang**, Y. Lei*, Potassium prussian blue nanoparticles: a low-cost cathode material for potassium-ion batteries', the 80th Annual Conference of the DPG, Mar 19-24, 2017, Dresden, Germany. **(Talk)**

6. B. Hai, Y. Xu, M. Zhou, C. Wang, **L. Liang**, Y. Mi, Y. Lei*, 'Stuctural engineering of electrode materilas for Na-ion batteries', the 80th Annual Conference of the DPG, Mar 19-24, 2017, Dresden, Germany. **(Poster)**

7. H. Zhao, R. Xu, M. Sommerfeld, L. Liang, M. Zhou, Y. Xu, Y. Lei*, 'Perfectly-ordered nanostructure arrays as potentially promising building blocks for constructing high-performance devices', the 80th Annual Conference of the DPG, Mar 19-24, 2017, Dresden, Germany. **(Poster)**

8. Y. Xu, M. Zhou, C. Wang, **L. Liang**, Fabian Grote, Y. Mi, Y. Lei*, 'Enhancement of sodium ion battery performance enabled by oxygen vacancies', the 80th Annual Conference of the DPG, Mar 19-24, 2017, Dresden, Germany. **(Talk)**

9. M. Zhou, Y. Xu, **L. Liang**, H. Zhao, B. Hai, Y. Lei*, 'Amorphous TiO_2 inverse opal anode for sodium ion batteries', the 80th Annual Conference of the DPG, Mar 19-24, 2017, Dresden, Germany. **(Talk)**

10. M. Zhou, Y. Xu, C. Wang, **L. Liang**, Y. Lei*, 'Nanoengineering based on colloidal crystal template for energy conversion and storage', The 3rd International Conference & 5th International MacroNano-Colloquium on the Challenges and Perspectives of Functional Nanostructures (CPFN), June 20-22, 2016, Ilmenau, Germany. **(Talk)**

11. **L. Liang**, Y. Xu, Y. Lei*, 'Highly ordered 3D nanostructure arrays with improved electrochemical performance for sodium-ion battery anodes', the 2nd International Conference & 4th International MacroNano-Colloquium on the Challenges and Perspectives of Functional Nanostructures (CPFN), July 30-31, 2015, Ilmenau, Germany. **(Poster)**

12. Y. Xu, C. Wang, **L. Liang**, M. Zhou, Y. Lei*, 'Electrode and material design for sodium lion batteries**,** the 2nd International Conference & 4th International MacroNano-Colloquium on the Challenges and Perspectives of Functional Nanostructures (CPFN), July 30-31, 2015, Ilmenau, Germany. **(Talk)**

13. C. Wang, Y. Xu, Y. Fang, M. Zhou, **L. Liang**, S. Singh, H. Zhao, A. Schober, Y. Lei*, 'Extended π‑conjugated system for fast-charge and -discharge sodium-ion batteries', the 2nd International Conference & 4th International MacroNano-Colloquium on the Challenges and Perspectives of Functional Nanostructures (CPFN), July 30-31, 2015, Ilmenau, Germany. **(Poster)**

14. Y. Xu, M. Zhou, X. Wang, C. Wang, **L. Liang**, F. Grote, M. Wu, Y. Mi, Y. Lei*, 'Enhancement of sodium ion battery performance enabled by oxygen vacancies**,** the 2nd International Conference & 4th International MacroNano-Colloquium on the Challenges and Perspectives of Functional Nanostructures (CPFN), July 30-31, 2015, Ilmenau, Germany. **(Poster)**

15. Y. Xu, M. Zhou, **L. Liang**, Y. Mi, Y. Lei*, 'Highly ordered nanoarchitectures for energy-related applications', the 1st International Conference & 3rd International MacroNano-Colloquium on the Challenges and Perspectives of Functional Nanostructures (CPFN), July 30-31, 2014, Ilmenau, Germany. **(Talk)**

16. M. Zhou, Y. Xu, **L. Liang**, Y. Mi, Y. Lei*, 'Template-directed nano-architectured electrodes for advanced energy conversion and storage', the 1st International Conference & 3rd International MacroNano-Colloquium on the Challenges and

Perspectives of Functional Nanostructures (CPFN), July 30-31, 2014, Ilmenau, Germany. **(Talk)**

17. **L. Liang**, Y. Xu, H. Liu, Y. Lei*, '1-dimensional $AgVO_3$ nanowires hybrid with 2-dimensional graphene nanosheets to create 3-dimensional composite aerogels and their improved electrochemical properties', the 78th Annual Conference of the DPG, Mar 31- April 4, 2014, Dresden, Germany. **(Talk)**

Award

2016/12: National Excellent Self-financed International Students Scholarship (34 people in Germany)

Declaration

I hereby declare that this Ph.D. dissertation entitled "Rational Design of Antimony Nanostructures toward High-Performance Anode Materials for Sodium–Ion Batteries" was carried out by me for the degree of Doctor of Philosophy under the supervision of Prof. Dr. Yong Lei. All dates or information in this dissertation that have been directly or indirectly consulted or used from other sources are clearly stated. This dissertation has not been submitted, in part or in whole, for any other degree or examination in any other University. I have acknowledged all main sources of help, and I have made clear exactly what was done by others and what I have contributed when the work was done jointly with others. Some of the results may have been published in scientific journals or elsewhere. I am aware that the falsity of this declaration will be regarded as an attempt of deception and will cause the derogation of the doctoral procedure.

Ilmenau, 26. April 2017

Liying Liang